Chemical Evolution in Protoplanetary Disks

by

Jeffrey K. J. Fogel

A dissertation submitted in partial fulfillment
of the requirements for the degree of
Doctor of Philosophy
(Astronomy and Astrophysics)
in The University of Michigan
2011

Doctoral Committee:

Associate Professor Edwin A. Bergin, Chair
Professor Sushil K. Atreya
Professor Nuria P. Calvet
Professor Emeritus Charles R. Cowley
Professor Lee W. Hartmann

To my family, who have supported me throughout this long process.

And to Katie, I wouldn't have made it without you.

ACKNOWLEDGMENTS

I would not have been able to complete this dissertation without support from many colleagues. I am pleased to have this opportunity to acknowledge their contributions.

First and foremost I would like to thank my advisor, Ted Bergin. He worked tirelessly with me along the way to track down bugs, decipher results and generally make sure that my work was the best that it could be. When I was stuck on an issue, a conversation with Ted immediately clarified how to solve the problem and how to move forward. I learned a huge amount from him, both about astronomy and about how to approach and solve problems. He also acted as a mentor, providing important support and guidance in my career decisions.

I also would like to thank my committee members, Sushil Atreya, Nuria Calvet, Chuck Cowley and Lee Hartmann for their feedback and advice along the way. Their comments were critical in shaping this work. All of them were very generous with their time and willing to discussing any issues that arose during my research.

The work presented here could not have been completed without the support and assistance of my collaborators, including Ted Bergin, Tom Bethell, Nuria Calvet, Ilse Cleeves, Paola D'Alessio, Catherine Espaillat, Lee Hartmann, Sébastien Maret, Dmitry Semenov and Zhaohuan Zhu. Their contributions of code, time spent running models and discussions with me of astrophysical phenomena were all invaluable. I want to especially thank Ilse, who often postponed her own work in order to run models for me.

Finally, I would like to thank all of my friends and family who have tirelessly supported me along the way. The many volleyball and softball games helped to relieve stress and keep me sane during the long process. Thank you!

Chapter 2 of this dissertation is based on work published in the Astrophysical Journal (Fogel et al., 2011). This work was supported by the National Science Foundation under Grant 0707777.

CONTENTS

LIST OF FIGURES

FIGURE

LIST OF TABLES

TABLE

ABSTRACT

This dissertation presents a new model for calculating the chemistry of protoplanetary disks prior to and during the initial stage of planet formation. In this dissertation we analyze the effects of some important physical processes on determining that chemistry.

Chapter 2 describes the new model and analyzes the effects of including dust settling and Ly α radiation in the stellar UV field on the protoplanetary disk chemistry, two elements missing from most previous models. In agreement with earlier studies, the evolution of dust grains plays a large role in determining how deep the UV radiation penetrates into the disk. Significant grain settling at the midplane leads to much smaller freeze-out regions and correspondingly larger molecular layers. The inclusion of Ly α radiation impacts the disk chemistry through specific species that have large photodissociation cross sections at 1216 Å. These include HCN, NH_3 and CH_4, for which the column densities are decreased by an order of magnitude or more.

Chapter 3 looks at the effects of including dust-dependent X-ray opacity on the chemistry and analyzes the location of the dead zone in these disks. This is the first work that calculates a dead zone from the ion-neutral collision rate combined with a detailed disk chemical model. In our most realistic model, where cosmic rays are deflected by a stellar wind, the active zone at 5 AU is only 3 g cm^{-2} with dust settling included, which is too low to match the observed mass accretion rates. The dust-dependent X-ray opacities affect the abundance of related species, such as N_2H^+ and HCO^+, but rarely by more than a factor of two.

Chapter 4 analyzes the effects that central star spectral type has on the protoplanetary disk chemistry and specifically the chemistry of the midplane. The spectral type will change the temperature and density structure of the disk, which influences

the overall chemical composition, as has been seen in recent observational disk surveys. We find that disks around G, F and A stars have warm CO-gas rich midplanes while less luminous stars have CO-gas poor midplanes.

CHAPTER 1

Introduction

Where we come from is one of the most basic and fundamental questions in science. This dissertation focuses on origins, exploring the conditions associated with the earliest stages in the birth of planetary systems. Planets are born in protoplanetary disks - disks of gas and dust that form around newly formed protostars due to conservation of angular momentum when the rotating molecular cloud core that creates the star collapses. The material in this disk evolves both physically and chemically until the dust grains coagulate to form planets and the gaseous disk dissipates. Here, we explore how the initial steps of planet formation, the settling of dust grains to the disk midplane, alters the chemical composition.

1.1 Protoplanetary Disk Observations

Until recently our knowledge of protoplanetary disk chemical and physical evolution has relied on studying objects in our own solar system, such as meteorites, comets and the planets themselves. However, over the past decade we have begun to explore extra-solar protoplanetary disks through sensitive observations in millimeter and submillimeter wavelengths.

The dominant molecular component of protoplanetary disks, H_2, is largely unobservable, due to the lack of a dipole moment and a large rotation constant, except in high temperature regions close to the central star (Bitner et al., 2007). Instead, other molecular species, with significantly lower abundances, must be used to study and trace the physical and chemical structure of the disks. Despite these constraints, spatially resolved observations have been used to detect Keplerian rotation (Koerner

& Sargent, 1995; Simon et al., 2000) as well as a radial gradient in the temperature structure of the disk (Beckwith & Sargent, 1993).

Using millimeter and submillimeter spectroscopy, the following molecules have been identified in disks: H_2, OH, H_2O, CO (and isotopologues), CN, HCN, DCN, HNC, C_2H, C_2H_2, CS, HCO^+, H_2CO, H_2D^+, DCO^+, NH_3 and N_2H^+ (e.g., Dutrey et al., 1997; Kastner et al., 1997; Aikawa et al., 2003; Qi et al., 2008; Öberg et al., 2010). However, even with interferometers, limited resolution and sensitivity restricts these observations to size scales of tens of AU at the distance of the nearest star forming regions. This hinders the number of objects that we are able to study in detail. Currently, there are only a handful of well studied protoplanetary disk systems, including DM Tau, LkCa 15, AB Aur, TW Hya, GG Tau, MWC 480, AA Tau, GM Aur and CQ Tau (e.g., Dutrey et al., 1997; Qi, 2001; Qi et al., 2003; Thi et al., 2004; Dutrey et al., 2007a; Öberg et al., 2010). In the future, instruments such as the Atacama Large Millimeter Array (ALMA) and the James Webb Space Telescope (JWST) will significantly improve both our resolution and sensitivity capabilities, thereby allowing us to probe many more molecular species in many more objects. One of the goals of this dissertation is to predict the molecular abundance distributions that can be tested by future ALMA observations.

Although observational studies are relatively recent, we have learned a great deal about the physical structure of protoplanetary disks from our current observations (Semenov et al., 2010; Bergin, 2011, and references therein), which are described below.

1.2 Observational & Theoretical Constraints on Disk Structure

Protoplanetary disk chemical composition and evolution is highly dependent on the temperature and density structure of the disk as well as on the incident radiation, both from the central star and from the surrounding environment.

1.2.1 Physical Structure

The radial distribution for midplane temperature and density have been estimated from observations of dust thermal emission. They both are approximated at large radii by power-laws, $\Sigma(r) \propto r^{-p}$ and $T(r) \propto r^{-q}$ for p = 0-1 and q = 0.5-0.75. This leads to a midplane temperature of $\sim$ 100-200 K at 1 AU and a surface density at 100 AU of 0.1-10 g cm^{-2} (e.g., Beckwith et al., 1990; Kitamura et al., 2002). The vertical structure is determined by calculating hydrostatic equilibrium and leads to a flared disk structure (Kenyon & Hartmann, 1987). Disk heating is primarily through stellar irradiation, with the stellar radiation being absorbed by dust grains at the surface of the disk which then reprocess this radiation to longer wavelengths and heats the interior (e.g., Calvet et al., 1992; Chiang & Goldreich, 1997; D'Alessio et al., 1998). As a result, when dust settling, the transfer of dust grains from the upper layers of the disk to the midplane (see Section 2.2.1), is incorporated into the disk structure calculations the stellar radiation is deposited in deeper layers, leading to higher overall temperatures.

A schematic picture of both the chemical and physical structure of the disk based on current theory can be seen in Figure 1.1. Due to the heating mechanism, the temperature of the disk generally decreases from the top of the disk towards the midplane at all r > 1 AU. The density distribution is generally $e^{(-z/H)^2}$, as seen in the top middle panel of the figure.

1.2.2 Chemical Structure

Due to the physical structure mentioned in Section 1.2.1, the disk chemical structure can be divided into three layers. As the abundance of CO is one of the most important quantities to determine, the C^+ to CO to CO(gr) transition will be used here as an illustration of the overall chemical structure. At the top of the disk is a photon dominated region (PDR), where molecules are dissociated primarily by the incident UV radiation. In this region the primary carbon-bearing species is C^+. Below this is the so-called 'warm molecular layer'. Here, the temperature is still high enough that most molecular species are not frozen-out onto dust grains, but the UV radiation is

shielded so as to prevent photodissociation. Therefore the primary carbon-bearing species in this region of the disk is gas-phase CO. Finally, approaching the midplane the temperature of the disk is low enough, $\lesssim$ 20 K, that most molecules, including CO, are frozen-out onto dust grains. The specific location of these layers depends on the physical structure of the disk, especially whether dust settling is included or not, as well as the chemical species examined.

1.2.3 Radiation

While temperature plays a large role on the chemistry in the disk (Fegley & Prinn, 1989; Prinn, 1993; Bergin et al., 2007), non-thermal processes such as UV radiation, cosmic rays and X-ray radiation act as ionizing agents that create and destroy molecular species and are contributors to the disk physical structure and evolution.

Cosmic ray ionization has an attenuation depth of 96 g cm^{-2} (Umebayashi & Nakano, 1981). For typical disk structures, such as that seen in Section 1.2.1, this suggests that cosmic rays are able to penetrate to the midplane at R $\gtrsim$ 1 AU. Cosmic rays power chemistry via the ionization of H_2, which ultimately forms H_3^+ which then powers the molecular chemistry (Graedel et al., 1982). Cosmic rays can ionize molecules, thereby driving ion-molecule reactions (Aikawa et al., 1997), and are critical to determining the ionization fraction of the disk in the densest regions. They potentially can be deflected from the disk if there is a stellar wind present, similar to that in our own solar system, though detections of ions such as HCO^+ and H_2D^+ indicate that cosmic rays do play a role in disk chemistry, at least in the outer radii (Semenov et al., 2004; Ceccarelli et al., 2005).

Stellar X-rays have a penetration depth of 0.008 g cm^{-2} for 1 keV X-rays and 1.6 g cm^{-2} for 10 keV X-rays in an unsettled disk (Glassgold et al., 2000). X-rays also power chemistry through the ionization of H_2 that then forms H_3^+. The penetration depths indicate that, except for the outermost radii (R $\gtrsim$ 50 AU), the X-rays are not able to penetrate all the way to the midplane, but instead are important in the surface and molecular layers.

T Tauri stars emit UV radiation in excess of what would be expected from a

blackbody with the same temperature of $\sim$ 4000 K. This is due to the accretion of disk material onto the central star (Calvet & Gullbring, 1998), but could also potentially be influenced by an active chromosphere (Alexander et al., 2005). The strength of the UV field around T Tauri stars is generally parameterized in terms of the interstellar radiation field (Habing, 1968, $G_0 = 1$) and is observed to have values of $G_0 \sim 300$ - 1000 at 100 AU (Bergin et al., 2004). As the shape of the UV field can be important, properly treating UV scattering and radiative transport is critical to understanding its impact on the chemistry (van Zadelhoff et al., 2003). The UV field consists of two components: an interstellar radiation field (ISRF) that strikes the disk at a normal angle of incidence and the stellar radiation field (SRF), dominated by UV emission from the accretion shock, that has a more shallow angle of incidence (Willacy & Langer, 2000).

In addition, Ly α radiation can carry $\sim$ 75 % of the FUV flux (Bergin et al., 2004; Herczeg et al., 2004) and scatter differently from the rest of the UV field, thereby making it an important driver of chemistry in the disk (Bergin et al., 2003). Whereas the general UV field scatters solely off of the dust grains, the Ly α radiation scatters from the atomic hydrogen in the disk prior to scattering off of dust grains, meaning that it needs to be treated separately from the rest of the UV field (Bethell et al., 2010).

1.3 Chemical Evolution Modeling

Models of protoplanetary disk chemistry have grown increasingly more sophisticated as the structure, radiation, and physical processes mentioned above were included. Initially, disk compositions were calculated assuming thermochemical equilibrium (e.g., Lewis, 1974), which seemed to match with the observations of our solar system. However, in the 1990s it was realized that chemical kinetics played a large role in determining observed abundances in extrasolar protoplanetary disks and new models were developed that directly solved the time-dependent reaction equations (e.g., Aikawa et al., 1996; Willacy et al., 1998; Aikawa & Herbst, 1999). To these increasingly complex models, non-thermal processes such as X-ray ionization and UV

radiation as well as grain processes, changing dust grain size and mixing were incorporated in order to more closely match the observations (e.g., Aikawa & Nomura, 2008; Willacy & Woods, 2009; Woitke et al., 2009; Nomura et al., 2009).

Despite this progress, there are a number of omissions in current disk models that we hope to answer in this dissertation.

Protoplanetary disk chemical models have included stellar UV fields and even simple Ly α radiation treatments (Nomura & Millar, 2005), but no previous work has explored an observationally motivated radiation field that coupled the resonant line radiation transfer of Ly α radiation with the full disk chemistry. Given the dominance of Ly α radiation in T Tauri stars, it will likely strongly influence the chemical evolution. In particular, there are systematic differences in photodissociation rates for species that have cross sections at 1216 Å (van Dishoeck et al., 2006), as compared with those that do not. For example, ratios such as CN/HCN will be affected since CN is dissociated primarily below 1150 Å while HCN is subject to dissociation by Ly α radiation (Bergin et al., 2003). The inclusion of Ly α radiation might then increase the CN/HCN ratio and potentially allow for a better fit to the observed ratios (e.g., Thi et al., 2004).

Another factor that is relatively unexplored in most disk chemical models is the effect of dust settling. As disks evolve, the dust grains in the upper layers of the disk settle to the midplane while the gas remains suspended. The settling of dust grains lowers the optical and UV opacities in the upper regions of the disk, leading to a flatter geometry and greater penetration of radiation, both for UV and for X-ray radiation (Dullemond & Natta, 2003; Bethell & Bergin, 2011). The increase in penetration of the SRF also will affect the temperature structure of the disk, with more settled disks leading to higher temperatures (D'Alessio et al., 2006).

The chemical changes due to dust settling can play a large role as contributors to other processes, such as mass accretion onto the central star. As we show, dust settling increases the size of the ionized region in the disk, which in turn increases the region of the disk that is active due to magneto-rotational instability (MRI). Given the fact that observed spectral energy distributions (SEDs) have indicated that most

disks are settled (e.g., Furlan et al., 2006), this is an important question to examine in detail.

Finally, most disk chemical models have looked primarily at only a single spectral-type central star. There have been models of T Tauri stars (e.g., Aikawa et al., 2002; Willacy, 2007; Nomura et al., 2007) and Herbig stars (Jonkheid et al., 2007), but very few studies have investigated a cross-comparison of spectral types (Pinte et al., 2010). Observational studies are beginning to systematically study the effects of spectral type on observed molecular signatures (Öberg et al., 2010), so it is timely for chemical models to also explore the effects of spectral type on the chemistry. In particular, the temperature of the central star will affect the temperature structure of the disk, which will have implications for the observed chemical composition.

In this dissertation we present a new protoplanetary disk chemical model which differs from previous models by incorporating Ly α radiation transport, dust settling and dust-dependent x-ray opacity along with a detailed chemical reaction network. In Chapter 2 we present the details of the chemical model as well as analyze the effects of including Ly α radiation and dust grain settling in a protoplanetary disk chemical model around a T Tauri type star. In Chapter 3 we discuss the implications of dust grain settling on the X-ray radiation penetration and how this affects the chemistry and active zones in the disk. In Chapter 4 we look at the effects that changing the central star spectral type has on the chemistry by looking primarily at the midplane, where most of the mass is locateds. In Chapter 5 we summarize the results of our chemical model and look to the future for modeling efforts.

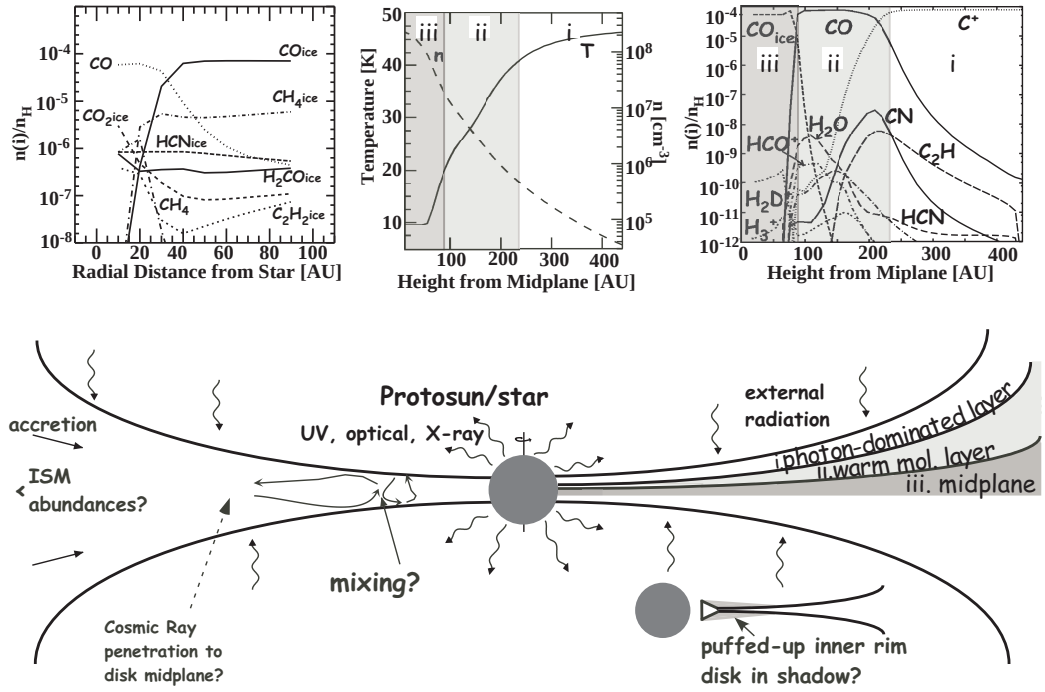

Figure 1.1. Chemical structure of protoplanetary disks (taken from Bergin et al., 2007). The vertical structure is divided into three zones: a photoionization layer, a warm molecular layer and a freeze-out layer. There are various non-thermal mechanisms, including cosmic ray, UV and X-ray driven chemical reactions. Viscous accretion and turbulence will transport the disk material both vertically and radially. The top panels show the radial and vertical distribution of molecular abundance for a typical disk model at the midplane (Aikawa et al., 1999) and r $\sim$ 300 AU (van Zadelhoff et al., 2003). A sample of the hydrogen density and *dust* temperature at the same distance (D'Alessio et al., 1999) is also provided.

CHAPTER 2

Model Description, Ly α Radiation and Dust Settling

2.1 Introduction

Planets form in protoplanetary disks around stars with disks, though the exact mechanism of this formation is still not clear. It is therefore important to understand the physical conditions in the disks in which they form. In particular, studying the chemical history of these disks provides us with a wealth of information because the chemistry responds to the physical environment. From the observed molecular emission we are able to explore disk physics such as the overall ionization fraction, which impacts on accretion physics, and disk kinematics, a direct probe of rotation and turbulence (see Apai & Lauretta, 2010, and references therein). In addition, the chemical composition of extrasolar protoplanetary disks can be compared to that of the many remnants from planet formation that we observe in our own solar system, such as comets, meteorites and asteroids. The composition of these bodies provides a chemical memory of the formation of our solar system. It is therefore necessary to understand the chemical evolution of protoplanetary disks so that we can unravel the mystery of how our own solar system formed and characterize planet formation elsewhere.

Because chemical processes respond to the physical state of the gas, knowledge of the physical environment of the disk is required to properly model the chemistry. This includes determining how the chemical composition of the disk is affected by the local density and temperature as well as by radiation from the central star and the surrounding environment. Based on observations of T Tauri stars, a typical

disk system consists of a central star surrounded by a flared dusty disk hundreds of AU in radius. T Tauri stars are low-mass young stellar objects, masses range from 0.08 to 2 $M_{\odot}$, with emission spectra that peak in optical wavelengths, though they also emit in the UV and X-ray regimes (Ardila et al., 2002; Kastner et al., 1997). The optical emission determines the dust temperature within the structure of the disk (Calvet et al., 1991), but it is the UV and X-ray radiation that provides the ionizing photons needed to power molecular chemistry. Due to the radial dependence of the sound speed, the disks themselves are flared (Kenyon & Hartmann, 1987). Armed with models of the disk physical structure, chemical models have suggested that beyond $R \sim 40$ AU, the size scale probed by current observations, the chemical structure of the disks around T Tauri stars can be divided into three regions: the photon dominated region, the warm molecular layer, and the frozen-out midplane (e.g., Aikawa et al., 2002; Willacy & Langer, 2000; Semenov et al., 2004). This is in agreement with the limits set by observations of molecular emission. Radiation from the central star as well as the interstellar radiation field (ISRF) ionize atoms and dissociate molecules at the surface, leading to a photon dominated region at the top of the disk where chemical elements exist primarily as free atoms or ions. Near the midplane, the temperature is low enough that freeze-out of molecules as ices on grains can occur. In between is a layer that is warm enough to prevent freeze-out, but shielded enough so that molecular species can form. The exact locations of these regions depend on the chemical species, due to the differences in binding energies and freeze-out temperatures between different molecules.

Over the years, chemical models of protoplanetary disks have grown increasingly more sophisticated (Bergin et al., 2007, and references therein). The first generation determined the disk composition by assuming thermochemical equilibrium in the disk (e.g., Lewis, 1974). Once it was realized that chemical kinetics, and not just the solids, played a large role in determining the observed abundances, models were developed that directly solved the time-dependent reaction equations (e.g., Willacy et al., 1998; Aikawa & Herbst, 1999). The current state-of-the-art models include cosmic ray and X-ray ionization, UV radiation from the central star, adsorption and desorption onto

and off of grains, changing dust grain sizes, some simple mixing, surface chemistry, and some isotopic chemistry (e.g., Aikawa & Nomura, 2008; Willacy & Woods, 2009; Woitke et al., 2009; Nomura et al., 2009). For these models, surface chemistry refers to hydrogenation of H (forming H_2) and O (ultimately forming H_2O), that occurs on the surfaces of dust grains.

One major aspect of protoplanetary disk chemistry models is to properly treat the transfer of FUV radiation that is incident on the disk. This includes UV radiation, both from external sources (typically the ISRF) and from the central star (mostly the accretion shock, which dominates the stellar radiation field, SRF, in the UV regime for T Tauri stars) as well as X-ray emission from the central star. The two different sources of UV radiation have different angles of incidence on the disk with the ISRF having a normal angle of incidence, while the SRF has a very shallow angle of incidence (Willacy & Langer, 2000). Because of this, it has been shown that properly treating the absorption and scattering of the SRF is critical in calculating the disk chemical evolution as there is little penetration of the UV field into the disk without scattering being taken into account (van Zadelhoff et al., 2003).

In addition to properly treating the UV radiation transfer, Ly α radiation is an important component in fully dealing with the UV field. Bergin et al. (2003, 2004) and Herczeg et al. (2004) showed that Ly α radiation is dominant in the UV fields of some T Tauri stars, and in fact can carry up to 75% of the UV flux from these stars. Additionally, the scattering of the Ly α radiation in the disk will be different from the scattering of the general UV field. Whereas the general UV field scatters solely off of the dust grains, the Ly α radiation scatters from the atomic hydrogen in the disk prior to scattering off of dust grains, meaning that it needs to be treated separately from the rest of the UV field (Bethell et al., 2010). The scattering of Ly α radiation from atomic hydrogen also differs from the scattering off of dust grains in that it is isotropic, as opposed to scattering off of dust grains which is preferentially in the forward direction (Bonilha et al., 1979; Draine, 2003). Previous models have included stellar UV fields, but no previous model has included an observationally motivated radiation field that coupled the resonant line radiation transfer of Ly α radiation

with the full disk chemistry. Given the dominance of Ly α radiation in T Tauri stars, the lack of Ly α radiation in previous disk chemistry models is a significant omission (Bergin et al., 2003). Including this source of radiation can potentially lead to better agreement with the observations, as discussed in Section 1.3.

Another factor in properly dealing with UV radiation propagation is the dust in the disk. Both dust settling and dust coagulation will lower the opacities in the upper regions of the disk, leading to a flatter overall disk and greater penetration of radiation (Dullemond & Natta, 2003). This increase in penetration depth for the UV radiation has been measured observationally by looking at the spectral energy distributions (SEDs) of these T Tauri stars and measuring the SED slope in the mid-IR wavelengths (5-30 μm), with more dust settling leading to a flatter slope (e.g., Furlan et al., 2008). These observations show that most disks are fit by models with significant dust settling included.

Motivated by these physical effects, we have created a protoplanetary disk chemistry model that includes the treatment of the radiation transfer of Ly α radiation from Bethell et al. (2010) coupled with the full disk chemistry to demonstrate how the inclusion of Ly α radiation will affect disk chemistry. We have also looked at the effect of dust settling on the chemical composition of the disk. In Section 2.2 we describe the model used to calculate the chemistry in these protoplanetary disks. The physical model, as well as the types of chemical reactions used, is discussed. In Section 2.3 we present the effects that including dust settling and Ly α radiation has in terms of the chemistry of the disk and in Section 2.4 we discuss why it is necessary to include them in future disk chemical models.

2.2 Model

Our numerical model is based on the ALCHEMIC code, written by Semenov et al. (2010) for use on molecular cloud chemistry, and heavily modified for our purposes. It is a (1+1)-dimensional model, which means that while the code itself is one-dimensional (1D) over height at a specific radius, the code was run at a range of radii to give a pseudo-two-dimensional result. The disadvantage of such a model

is that there is no interaction between horizontal zones, though with no mixing included this should be a minor effect. Our treatment of the UV field, however, was a full two-dimensional treatment. The code modeled a flared protoplanetary disk with incident radiation from a central T Tauri star as well interstellar cosmic rays. Our model calculated the chemical abundances for 639 chemical species and 5910 chemical reactions. While most of the reactions were not time-dependent, we did incorporate a few time-dependent reactions into the network which will be discussed in more detail below.

2.2.1 Physical Model

In this section we describe the physical structure of the disk that was used as well as the radiation field incident on the disk. We used the parameters for a typical T Tauri star with radius $R_* = 2\ R_\odot$, mass $M_* = 0.5\ M_\odot$, mass accretion rate $\dot{M} = 10^{-8} M_\odot$ yr^{-1} and temperature $T_* = 4000$ K (e.g., Kenyon & Hartmann, 1995). The dust composition, taken from D'Alessio et al. (2006), consists of two populations, a large grain and a small grain component. In both cases, the grain size distribution is given by a power law of the grain radius (a): $n(a) = n_0 \left(\frac{a}{a_0}\right)^{-p}$, where $p = 3.5$, $a_{min} = 0.005$ μm, $a_{max,small} = 0.25$ μm, and $a_{max,large} = 1.00$ mm.

Our model includes the effects of dust settling, parameterized by ϵ, defined as the dust-to-gas mass ratio of the small grains in the upper regions of the disk relative to the standard dust-to-gas mass ratio of 0.01 (D'Alessio et al., 2006). A value of $\epsilon = 1$ means that no settling has taken place, while a smaller value of ϵ indicates a depletion of dust grains in the upper regions of the disk and a corresponding increase in large dust grains near the midplane. We therefore assume that the disk is well shielded in a thin layer near the midplane. The general disk temperature and density structure for dust settling parameters of $\epsilon = 1$ and 0.01, shown in Figure 2.1, are based on the assumption that the gas and dust temperatures are well coupled (Kamp & Dullemond, 2004). When dust settling is included, the temperature structure of the disk changes which leads to a less flared disk due to the surface density being approximated as

$$\Sigma \sim \frac{\dot{M}\Omega_k}{3\pi\alpha c_s^2(T)} \tag{2.1}$$

where Ω_k is the Keplerian angular velocity, α is a free parameter defined by Shakura & Sunyaev (1973) and c_s is the sound speed. Because of the dependence of the sound speed on temperature, a different temperature structure will lead to a different density structure for the disk. For the settled models, the temperature of the disk near the midplane is increased due to the greater penetration depth for radiation in the more settled disks, which will play a large role in determining the chemistry of the disk. Recent studies have found that protoplanetary disk observations are well fit using dust settling parameters of $\epsilon \lesssim 0.01$ (Furlan et al., 2006). For the results presented in this chapter, we compared ϵ values of 1, 0.1 and 0.01. Based on the work done by Andrews & Williams (2005) we assume that the inner and outer disk dust populations are coupled, and so we treat them identically. The mass of the disk depends on the dust settling parameter and was 0.02 $M_\odot$ for $\epsilon = 1$ and 0.01 $M_\odot$ for $\epsilon = 0.1$ and 0.01.

In order to more clearly understand the gross effects of Ly α radiation on the chemistry of the disk we do not include any turbulent mixing in the disk. Additionally, grain growth in our model is not time dependent, but is fixed for each model. While including these time-dependent processes in a detailed chemical model might be interesting, even with modern computers it is a very computationally intensive set of calculations. Many previous models of disk chemistry have reproduced results in agreement with observations without including these processes (e.g., Aikawa & Herbst, 1999; Willacy & Langer, 2000; Aikawa & Nomura, 2006). In comparison, to first order, diffusion smoothes out abundance variations with height and increases the depth of the molecular layer (e.g., Ilgner et al., 2004; Semenov et al., 2006; Willacy et al., 2006). Thus we can still understand the large-scale effects of Ly α radiation on the chemistry without including diffusion or turbulent mixing in our model.

2.2.2 UV Field Calculation

The UV field for the central star that was used for our model was calculated by Bethell et al. (2010), who explored the radiative transfer and scattering of Ly α radiation in a protoplanetary disk. This UV field was calculated such that the G_0(100 AU) value, the total flux in our calculated radiation field at 100 AU as compared to the total flux of the ISRF in the FUV band (Habing, 1968), was set to 732. This value was chosen as an average of the G_0 values observed by Bergin et al. (2004) for a set of T Tauri stars. An example of the UV spectra used can be seen in the top panel of Figure 2.2, which shows the UV field for a radius of 208 AU for an $\epsilon = 0.01$. The UV field was assumed to be very smooth for all wavelengths other than Ly α, which completely dominates the spectra. While there are known emission lines in the other portions of the UV spectra (Bergin et al., 2003), they are orders of magnitude lower than the Ly α radiation and would not significantly modify the disk chemistry presented here. The lower panel of Figure 2.2 shows the dependence of the UV field on the column density of the disk. Due to geometrical dilution, the UV field strength actually peaks slightly inside the disk and not at the surface. The distance from the star to a point in the disk is $r^2 + z^2$. As z decreases, this distance shrinks and the UV field strength increases until there is enough material between the star and the point for the UV field to be attenuated.

The Ly α photon density was calculated in the two-stage process described in Bethell et al. (2010). Here we provide only a high-level description of the aspects of the method most relevant to disk chemistry. In order to follow continuum FUV and Ly α photons from the star into the disk, the gas and dust opacity must first be known. We assume that the pure absorption of both continuum and Ly α photons is simply due to dust. The scattering opacity requires more careful consideration and is of central importance to the propagation of Ly α. For continuum photons we assume scattering is due to dust. For Ly α the scattering is a combination of dust scattering and resonant scattering by H atoms. For consistency, we use the same dust grain population as that used in D'Alessio et al. (2006). The first calculation is therefore to establish the distribution of atomic H, which is done by balancing the

formation of H_2 on grains with its destruction by UV photons in the Lyman-Werner bands (912-1100Å, Black & van Dishoeck 1987). Following Spaans & Neufeld (1997) we write the steady-state H_2 fraction, f_{H_2}, as

$$\frac{n(H_2)}{n_H} = \frac{Rn_H}{\zeta + 2Rn_H}. \tag{2.2}$$

We adopt the Cazaux & Tielens (2004) expression for the grain-surface H_2 formation rate R. The simple 'shielding function' approach of Draine & Bertoldi (1996) is used to estimate the H_2 dissociation rate, ζ, ensuring consistency with later chemical computations (Section 2.2.3). The photons are propagated through the (irregular two-dimensional) spatial grid using standard Monte Carlo radiative transfer techniques (e.g., Bethell et al., 2007). This approach allows the potentially important effects of scattering to be included (e.g., van Zadelhoff et al., 2003). The radiative transfer through the dusty H/H_2 distribution is iterated until a converged, simultaneous solution is achieved for both the H/H_2 distribution and UV radiation field. This iterative approach is typical for problems in which the opacity is coupled to the radiation field. It is important to note that the H/H_2 transition occurs readily, well above the regions where the bulk of the heavy element chemistry takes place. The H/H_2 transition defines the top of the so-called 'warm molecular layer'. In this sense the chemistry occurs against a background of a fully molecular H_2 disk. However, before the Ly α photons can reach these depths they must first pass through the upper "photodissociation layer," composed of mostly atomic H. This leads us to the second stage of the calculation: the detailed propagation of Ly α photons. We are in essence repeating the UV transport calculation, but this time treating the Ly α propagation in greater detail. While this two-stage approach is not fully self-consistent, it renders the overall problem more tractable.

Although the shape of the stellar Ly α line bathing the disk in T Tauri systems is generally not observed directly, it is known to be very wide in the case of TW Hya and in other stars with molecule-rich disks (FWHM >500 km s^{-1}, Herczeg et al. 2002; Bergin et al. 2004), especially when measured in Doppler widths of the disk gas

(Figure 2.3). As a result, the vast majority of Ly α photons scatter off the wings of the resonant-scattering Voigt profile presented by HI in the photodissociation layer. Even at frequency offsets as large as $\pm$200 Doppler widths relative to line center (1216Å), the resonant scattering opacity of H atoms suspended above the disk is greater than that due to the accompanying dust (assuming the typical interstellar dust:gas mass ratio ~ 0.01, i.e., $\epsilon = 1$). Of course, this difference is further enhanced by the removal of dust via settling. Dust settling also enhances the abundance of atomic hydrogen by reducing the H_2 formation rate (Equation 2.2). From the point of view of a stellar Ly α photon it is as though the disk is covered in an optically thick layer of high-albedo material (the atomic hydrogen), which immediately scatters approximately half of the incident Ly α photons out into space and the remaining photons downward into the disk. This downward scattering greatly increases the penetrating power of Ly α photons compared to the feebly dust-scattered continuum photons. Due to the great width of the Ly α line, its overall frequency evolution as the photons diffuse into the disk is relatively unimportant, and the scattering process can be treated as conserving photon energy. Nevertheless, in our calculation we follow the frequency evolution of photons using the detailed theory of 'partial frequency redistribution' (Hummer, 1962). Ultimately these photons are lumped together into a bolometric Ly α photon density, $J_\lambda(r, z)$, that is used later in chemical rate equations.

Because of the proximity of TW Hya, and the lack of interstellar gas along the line of site, it is the only system with detectable Ly α beyond the broad wings. However, H_2 fluorescent emission is clearly detected in the handful of low-mass T Tauri disk systems with high resolution FUV spectra. This H_2 is pumped via coincidences with Ly α (Herczeg et al., 2002). Thus it is likely that Ly α emission is an important facet of the UV field in most if not all accreting systems, although the exact strength amongst systems needs to be determined. This assertion will be quantified with new UV spectra from the *Cosmic Origins Spectrograph* on the *Hubble Space Telescope*, but preliminary results are in agreement (G. Herczeg, private communication).

In order to determine the effects of Ly α radiation on the chemistry of the disk, we ran two models, one with and one without the Ly α radiation. In the case without Ly

α radiation the UV field was identical, except that the continuum was interpolated over the Ly α peak to remove it. The results from these models will be presented in Section 2.3.

2.2.3 Chemical Model

For our chemical model we found the abundance of each species in the disk by solving rate equations for each chemical species at each time-step and zone in the disk. The basic equation we solved can be written as

$$\frac{dn(i)}{dt} = \sum_j \sum_l k_{jl} n(j) n(l) - n(i) \sum_j k_{ij} n(j) \tag{2.3}$$

where $n(i)$ is the abundance of species i and k_{ij} is the reaction rate for reacting species i and j. At its most basic, this equation is a summation of the rates of destruction of a species subtracted from the summation of the rates of formation. The specific rate equations for each reaction used in our network depended on the type of the reaction and will be discussed in further detail below. Three-body reactions were not included in our network, as we were mostly concerned with the outer regions of the disk and three-body reactions become competitive only in the inner regions of the disk where temperatures and densities are very high (n $> 10^{14}$ cm^{-3}, Willacy et al., 1998). Initial abundances of each species were taken to be molecular cloud abundances, approximated from Aikawa & Herbst (1999) and are listed in Table 2.1.

Our chemical network was based on the Ohio State University Astrophysical Chemistry Group gas-phase model from 2008 March[1] (Smith et al., 2004), with a number of additions that will be elaborated below. This network includes some gas-grain interaction, electron-grain recombination, cosmic ray ionization, cosmic ray induced photoreactions, ion-molecule reactions, charge exchange reactions, negative ion - neutral species reactions, radiative association, associate ejection, neutral + neutral $\rightarrow$ ion + electron, neutral-neutral chemical reactions, neutral-neutral radiative association, dissociative recombination, radiative recombination, positive ion-negative

[1] http://www.physics.ohio-state.edu/$\sim$eric/research.html

ion recombination, electron attachment, photoionization and photodissociation. The reaction rates for all of these reactions can be found on the OSU Web site, though only about 10%-20% of these reaction rates have been measured in the laboratory, which adds some uncertainty to all chemical network calculations (e.g., Wakelam et al., 2006; Vasyunin et al., 2008). We therefore focus primarily on the species that are less sensitive to these rate uncertainties, such as CO, H_2O, N_2H^+ and NH_3, where the abundances are consistent within a factor $\lesssim 3$. However, there are some species discussed here for which the abundances are more sensitive to the reaction rates used, such as CO_2, H_2CO, CN and HCN, but even in those cases the column densities are rarely uncertain by more than a factor of ~ 4 (Vasyunin et al., 2008).

Photodissociation

One addition to the OSU network was the incorporation of photodissociation of molecules from measured cross sections in the literature. These rates are dependent on both the strength and the shape of the radiation field that is used for the model. Because we were using an observationally motivated radiation field, it was necessary to treat the molecular photodissociation properly. Two different methods were used to calculate the photodissociation cross sections. For those molecules where UV cross sections for the molecules have been measured (van Dishoeck et al., 2006), the reaction rate was determined by

$$k_{\rm photodissociation} = \int \frac{4\pi\lambda}{hc}\sigma(\lambda)J_\lambda(r,z)d\lambda \ {\rm s}^{-1} \tag{2.4}$$

where $\sigma(\lambda)$ is the wavelength-dependent cross section of the molecule and $J_\lambda(r,z)$ is the radiation field at any point in the disk (calculation described in Section 2.2.2). For all of the species that did not have measured cross sections in the literature, the photodissociation rates were calculated by

$$k_{\text{photodissociation}} = G_0(100\text{AU}) \left(\frac{100.0}{R(\text{AU})} \right)^2 \alpha e_\tau(r, z, \lambda = 1500\text{Å}) \text{ s}^{-1} \tag{2.5}$$

$$e_\tau = \frac{J_{\lambda,z}}{J_{\lambda,z_{\max}}} \tag{2.6}$$

where $G_0(100\text{AU})$, as defined above, is the dimensionless scaling factor between the ISRF and the radiation field we used for our model and was set to 732. α is the unshielded photodissociation rate taken from the UMIST 2006 database (Woodall et al., 2007), while e_τ accounts for the attenuation of the radiation field. Normally, this term would just be $e^{-\tau}$, however due to scattering of the radiation the attenuation needed to be calculated as the radiation field for a given height z, ($J_{\lambda,z}$), divided by the maximum radiation field at that radius ($J_{\lambda,z_{\max}}$). A wavelength of 1500 Å was chosen as a wavelength well beyond that of Ly α to use for this calculation.

A comparison of the calculated photodissociation rates of HCN versus total column is shown in Figure 2.4. This figure illustrates the reaction rate of HCN for three different methods of calculating the photodissociation rate. The dashed line shows the result if we assume a normal ISRF scaled to match our radiation field in the FUV, Equation 2.5, but without any scattering included. The dotted line includes the e_τ term which incorporates the attenuation and scattering of our UV field at 1500 Å (van Zadelhoff et al., 2003; Bergin et al., 2003). Finally, the solid line is the result of using Equation 2.4 to calculate the rate from the wavelength-dependent cross section and our UV field. The spread in the three lines at high column densities indicates the importance of including scattering of the UV field in these calculations. The difference between the solid and dotted lines occurs as a result of using the wavelength dependent cross section instead of just approximating it at 1500 Å, which is especially important for species with a cross section at 1216 Å that will be affected by the presence of Ly α radiation. Because of geometrical dilution due to the flaring of the disk, the maximum UV field is actually a few tens of AU below the surface. This effect causes the rate calculated from the ISRF alone to be slightly higher in the lower column density regions of the disk.

Self-shielding of CO and H_2

Because the photodissociation rates of CO and H_2 are dominated by line rather than continuous absorption, self-shielding of these two molecules becomes significant in the regions where they are optically thick. For our model, CO self-shielding was calculated from the rates given in Visser et al. (2009) while the H_2 self-shielding rates were calculated from Lee et al. (1996). The H_2 photodissociation rate was

$$k_{\mathrm{H_2\ SS}} = 2.54 \times 10^{-11} G_0(100\mathrm{AU}) \left(\frac{100.0}{R(\mathrm{AU})}\right)^2 \times \theta[N(H_2)] \times e_\tau(r, z, \lambda = 1000\text{Å})(\mathrm{s}^{-1}) \tag{2.7}$$

where $\theta[N(H_2)]$ is the shielding factor for H_2 as calculated in Lee et al. (1996). Here, e_τ is defined in Equation 2.6, though in this case it is calculated at 1000 Å since that is the middle of the range where H_2 is photodissociated (van Dishoeck & Black, 1988). The G_0(100 AU) factor is used since the equation assumes an ISRF, which needed to be scaled up to match the UV field in our model.

For CO, the shielding functions in Visser et al. (2009) were calculated for the unmodified ISRF and thus needed to be scaled up to match our UV field. However, there was one modification to the scaling technique used to calculate the self-shielding rate for H_2. Because CO does not have a cross section coincident with Ly α radiation at 1216 Å, but the radiation field used for our models had a large fraction of its UV flux at 1216 Å, using a G_0 value calculated with Ly α included would lead to erroneous results. Instead, the peak at 1216 Å was removed by linearly interpolating over that portion of the curve and that resulting curve was used to calculate a new G_0 value used in the CO photodissociation calculations. This led to a G_0(CO) value of $\sim$ 150. In addition, $e_\tau(r, z, \lambda = 960\text{Å})$ was used, with 960 Å chosen to be in the middle of the CO photodissociation range. In both of the self-shielding cases the calculation of the rates were time-dependent since they depended on the column density of the molecule.

X-ray Ionization and Cosmic Ray Ionization

Observations of T Tauri stars have shown that they emit strongly in X-rays, with luminosities between 10^{29} - 10^{31} erg s^{-1} (Flaccomio et al., 2009; Feigelson & Montmerle, 1999; Glassgold et al., 1997). Aikawa & Herbst (1999, 2001) discussed the effects that this radiation has on protoplanetary disk ionization and chemistry, which includes secondary ionization of hydrogen gas as well as UV photolysis induced by the X-rays. For our model, both of these effects have been included using the formalisms developed by Glassgold et al. (1997) and Aikawa & Herbst (2001), using an X-ray luminosity of 10^{29} erg s^{-1} emitted at a height of ~ 10 R$_\odot$ above the midplane. For the cosmic ray ionization reactions we have followed the formalism presented by Semenov et al. (2004) with cosmic rays striking the disk vertically on both sides with an attenuation column of 96 g cm^{-2} (Umebayashi & Nakano, 1981) and an unshielded cosmic ray ionization rate of 1.3×10^{-17} s^{-1}.

Adsorption and Desorption

The majority of our chemical network is made up of gas species and most of the reactions in our network are between two such species. Just looking at gas species, however, leaves out a critical component of disk chemistry, reactions between gas species and dust grains. In order to self-consistently treat the gas-grain interactions, the reaction rates for all such reactions were decreased by a factor of ϵ in order to take into account the effect of the dust grains settling to the midplane.

Adsorption is the process by which a gas-phase species sticks to the surface of a dust grain and is retained due to van der Waals or surface bonding forces. For the low temperatures that we were looking at in our models we assumed sticking coefficients of unity, in agreement with laboratory measurements (Burke & Hollenbach, 1983; Masuda et al., 1998; Bisschop et al., 2006). The reaction rate for species adsorption onto grains can then be written as

$$k_{\rm ad} = \sigma_{\rm gr}\sqrt{\frac{8.0k_BT}{\pi\beta m_{\rm H}}}Sn_{\rm gr}({\rm s}^{-1}) \tag{2.8}$$

where $\sigma_{\rm gr}$ is the cross section of the dust grain, approximated to be $\pi r_{\rm gr}^2$. The dust

grains were assumed to have a radius of $r_{\rm gr} = 0.1\mu m$ which leads to a cross section of $3.14 \times 10^{-10}{\rm cm}^2$ in Equation 2.8. This is slightly larger than the average dust grain size calculated from the distribution in Section 2.2.1 of 0.02 μm due to the fact that smaller grains are subject to thermal spikes and it is therefore harder for molecules to adsorb onto small grains (Leger et al., 1985). k_B is Boltzmann's constant, β is the molecular weight of the species, and S is the sticking coefficient.

In our model there were three different methods of desorption, or ways to overcome the binding energy that holds a species to the surface of a dust grain after it has been adsorbed.

Thermal desorption. For thermal desorption, the rate of desorption was calculated using the Polanyi-Wigner relation (Tielens, 2005):

$$k_{\rm td} = \sqrt{\frac{3.0 \times 10^{15} k_B E_b}{\pi^2 \mu {\rm m_H}}} e^{-E_b/T} ({\rm s}^{-1}) \tag{2.9}$$

where E_b is the binding energy of the molecule and T is the dust temperature. Binding energies were taken from Hasegawa & Herbst (1993) and Willacy (2007) with the exception of H which was set to 1500 K, consistent with Cazaux & Tielens (2004). By equating the flux of thermally desorbing molecules from a grain surface to the flux of adsorbing molecules, it is possible to estimate the freeze-out temperature for a given species. Doing this, Hollenbach et al. (2009) estimated freeze-out temperatures for H_2O of $\sim$ 100 K, but only $\sim$ 20 K for CO. This has two implications for protoplanetary disk chemistry. The first is that each species will have a slightly different disk structure, in terms of where we see the freeze-out region, that is dependent on the freeze-out temperature of that species (Aikawa et al., 2002). Second, the different temperatures mean that species will freeze out at different locations in the disk, affecting which species are available for further chemical reactions in those regions.

Cosmic ray desorption. We included cosmic ray desorption of ices from dust grains, however this is not a significant desorption mechanism in all regions of the disk. As mentioned before, we assumed an attenuation column of 96 g cm^{-2} for cosmic rays. This means that at radii less than $\sim$ 1 AU, where Σ is greater than

96 g cm^{-2} even at the midplane, cosmic ray desorption never plays a large role in desorption. In contrast, in the outer regions of the disk the cosmic ray attenuation is fairly low and that, combined with low temperatures at the midplane, means that there are regions of the disk where cosmic ray desorption is an important desorption mechanism. For our model, the cosmic ray desorption rate was calculated using the formalism of Hasegawa & Herbst (1993) and Bringa & Johnson (2004).

Photodesorption. Photodesorption is the dominant form of desorption in the regions of the disk where the UV field can reach and the temperature is below a species' sublimation temperature. The rate for photodesorption by UV photons was calculated as:

$$k_{\rm photodesorption} = F_{\rm UV} Y \frac{\sigma_{\rm gr}}{N_{\rm sites}} N_p \frac{n(i)}{n_{\rm ice}} N_m^{-1} \tag{2.10}$$

where $F_{\rm UV}$ is the total UV flux, Y is the yield (the number of adsorbed particles ejected per incident photon), $\sigma_{\rm gr}$ is the grain cross section, $N_{\rm sites}$ is the number of reaction sites on the grain, assumed to be 10^6, N_p=2 is a correction for the fact that UV photons only penetrate the first few monolayers, $n(i)$ is the abundance of a given species, $n_{\rm ice}$ is the total abundance of all species frozen onto grain surfaces and N_m is the number of monolayers. This equation is valid for an assumed two or fewer monolayers per grain, as laboratory experiments by Öberg et al. (2007) indicate that most photodesorption occurs in the upper $\sim$ 2 monolayers. All species were assumed to have a yield of 10^{-3}, except for CO and H_2O for which we used recently measured values from Öberg et al. (2007, 2009b).

In order to properly treat the Ly α radiation, the normal photodesorption reactions mentioned above were calculated with the Ly α radiation removed from the UV field used in $F_{\rm UV}$ and instead a separate set of photodesorption reactions were included for all species that had a photodissociation cross section at Ly α wavelengths. There is little experimental data available on photodesorption rates, so we assumed that the physics of species on dust grains is similar to the physics of those species in the gas phase. This means that any species with a photodissociation cross section

at 1216 Å was assumed to have a related Ly α photodesorption cross section. In order to estimate the photodesorption yields of these species, we assumed a constant normalization factor between the gas-phase photodissociation cross sections in van Dishoeck et al. (2006) and the photodesorption yields. To determine the normalization factor we matched the photodissociation cross section for H_2O of 1.2×10^{-17}cm^2 at $\lambda = 1216$ Å with the photodesorption yield for H_2O(gr) of 2.36×10^{-3} measured by Öberg et al. (2009b). In symbolic form:

$$\frac{Y_{\rm H_2O}}{Y_X} = \frac{\sigma_{\rm H_2O}}{\sigma_X} \tag{2.11}$$

where σ_X is the photodissociation cross section of species X and Y_X is the photodesorption yield of that same species. This new yield was then used in Equation 2.10, but this time with only the Ly α radiation flux included. By treating the Ly α photodesorption separately in this manner, we remove the problem of the UV field having most of the flux at Ly α wavelengths, even if the species we are looking at does not have a cross section at 1216 Å.

Grain Surface Chemistry

While the vast majority of our reactions involved gas species or molecules adsorbing onto or desorbing off of grains, there were two series of grain surface chemistry reactions that were included in the model. The first is the formation of H_2 on grain surfaces. Here we show the reaction and the formalism for computing the evolution:

$$\rm H + grain \rightarrow H(gr) + grain \qquad \frac{dn_{H(gr)}}{dt} = n_H n_{gr} < \sigma v > S + ... \tag{2.12}$$

$$\rm H(gr) + H \rightarrow H_2$$

$$\text{if } n(\rm H(gr)) > n(gr): \qquad \frac{dn_{H_2}}{dt} = n_{gr} n_H < \sigma v > S + ... \tag{2.13}$$

$$\text{if } n(\rm gr) > n(H(gr)): \qquad \frac{dn_{H_2}}{dt} = n_{H(gr)} n_H < \sigma v > S + ... \tag{2.14}$$

The reaction is calculated in two steps because the limiting step is for a hydrogen

atom to find a grain. Additionally, if the abundance of hydrogen atoms on grains, H(gr), is greater than the abundance of grains in the system (Equation 2.13), the reaction rate is reduced by the ratio $\frac{n(\mathrm{gr})}{n(\mathrm{H(gr)})}$ to take into account the fact that a gas-phase atom must collide with a grain in order for the reaction to take place. In all cases, the rate coefficient is $< \sigma v_{\mathrm{H}} > S_{\mathrm{H}}$ where σ is the collisional cross section, defined as above as πr_{gr}^2, v_{H} is the velocity of a hydrogen atom assuming a Maxwellian distribution at the gas temperature, and S_{H} is the sticking probability of a hydrogen atom, assumed to be one.

The second series of grain surface reactions was oxygen chemistry to form water on grains and followed the treatment from Hollenbach et al. (2009). This included:

$$\mathrm{O(gr) + H \rightarrow OH(gr)} \tag{2.15}$$

$$\mathrm{H(gr) + O \rightarrow OH(gr)} \tag{2.16}$$

$$\mathrm{H(gr) + OH \rightarrow H_2O(gr)} \tag{2.17}$$

$$\mathrm{OH(gr) + H \rightarrow H_2O(gr)} \tag{2.18}$$

Laboratory experiments suggest that there is rapid formation of water ice on grain surfaces (Miyauchi et al., 2008), which makes these reactions a necessary addition to the chemical network since water is one of the dominant oxygen-bearing species. No other reactions on grains were included.

2.3 Results

2.3.1 Basic Model

For the purposes of the discussion to follow, X(gr) indicates species X adsorbed onto a grain surface. All abundances are relative to the total abundance of hydrogen (n(H) + 2 n(H_2)) by number density. In addition, all of the contour plots have been mirrored over the midplane to more easily display the features of the disk. Unless otherwise stated, all values are taken at a time of 10^6 years.

The general structure of our results, demonstrated in Figure 2.5, fits very well with the picture described earlier in Section 2.1 and seen by Aikawa et al. (2002). The figure shows C^+ and CO(gr) abundances for a disk with Ly α radiation and two dust settling values. In the upper regions of the disk there is a photodissociation region (PDR) where atomic ions and neutrals exist (little CO, no CO ice), below this is a molecular layer consisting mainly of molecules (CO, no CO ice) and near the midplane is a cold region where most of the chemistry consists of molecules frozen out onto grains (no CO, CO ice). This structure can also be seen in the upper-left plot of Figure 2.6, which is a plot of the major carbon-bearing species in the disk at a radius of 208 AU versus height. In the PDR ($z \gtrsim 200$ AU), all of the carbon is in the form of C^+ ions, in the molecular layer (50 AU $\lesssim z \lesssim$ 150 AU) the carbon is in the form of CO, and in the freeze-out region ($z \lesssim 50$ AU) the carbon is in the form of CO frozen out onto grains. The specific location of the CO freeze-out region is sensitive to the temperature profile around 20 K, where CO freezes out onto grains. As a result, different radiative transfer calculations will lead to slightly different locations of the freeze-out region (e.g., Dullemond et al., 2002).

Similar plots can be made for the oxygen-bearing, nitrogen-bearing and sulfur-bearing chemistry in the disk (Figure 2.6). For the oxygen-bearing species, the oxygen is primarily in the form of neutral O atoms throughout the disk until the disk is cold enough for water to adsorb onto dust grains. At that point, the oxygen quickly transitions from neutral O to H_2O ice on grains. There is a small layer between these two regimes where molecules such as CO and H_2O exist, but the molecular layer for oxygen-bearing molecules is very narrow. In the nitrogen-bearing chemistry, there are again three distinct regions. The PDR consists of neutral N which transitions to N_2 in the molecular layer and then freezes out as N(gr) in the freeze-out region.

The sulfur-bearing chemistry is the most complex. While the PDR and freeze-out regions are easy to distinguish, consisting of S^+ and S(gr) respectively, the molecular layer is complicated by the presence of multiple sulfur-bearing species, such as SO_2(gr), CS(gr) and OCS(gr), that adsorb onto grains at higher temperatures than S(gr).

Focusing on CN and HCN to demonstrate some of the more complicated chemical structure, Figure 2.7 shows the abundances of CN and HCN for an ϵ value of 1. Overall we see the general structure of PDR, warm molecular layer, freeze-out; however there is also evident substructure. The banding feature in these plots occurs due to the interaction between multiple formation and destruction mechanisms in the model. In the band of lower abundances around z = 100 AU, the temperature is low enough that there is some freeze onto grains, but the UV field is still able to penetrate so that there are reactions with PDR species (C^+ for HCN and O for CN) as well. Lower in the disk, the UV field is unable to penetrate as strongly, so the abundance of CN and HCN increases briefly until the temperature of the disk is cold enough for most of the CN or HCN to adsorb onto grains. This is just one example of how the interaction between different formation and destruction reactions can complicate the chemistry of the disk.

2.3.2 Dust Settling

An increase in dust settling will have a large impact on the thermal (Figure 2.1) and chemical structure of the disk (Aikawa & Nomura, 2006; Jonkheid, 2006). With dust settling included, most of the regions of the disk near the midplane will have temperatures higher than the 20 K needed for CO to adsorb onto dust grains (Hasegawa & Herbst, 1993). Figure 2.8 shows the abundance of CO and CO(gr) for ϵ values of 1, 0.1 and 0.01. The PDR (top), molecular layer (middle) and freeze-out region (midplane) of the disk can be clearly seen in all three CO plots. Dust settling increases the size of the molecular layer and shifts it toward the midplane at the expense of the freeze-out region. This leads to a reduction in the overall amount of CO(gr) in the middle of the disk. For an ϵ of 1, we see a freeze-out region in the bottom third of the disk, while for an ϵ of 0.01, only the region at the very midplane of the disk has a significant amount of CO(gr). This effect can also be seen in Figure 2.9, which plots C^+, the dominant carbon-bearing species in the PDR, and CO(gr), the dominant carbon-bearing species in the freeze-out region, for $\epsilon = 1$ and 0.01 at a radius of 200 AU. Above $z \gtrsim 200$ AU the PDRs of the two ϵ values are similar, but the molecular

layer is much larger, and the freeze-out region correspondingly smaller, in the case with dust settling included.

Looking at CO allows us to illustrate the general effects of including dust settling in our model. To quantify these effects more broadly, we look at column density ratios for a range of representative species at the three different dust settling parameters. Figure 2.10 compares the column densities of species at 250 AU for different dust settling parameter values. The majority of species plotted, mostly molecular, have larger column densities for an $\epsilon = 0.1$ disk than for an unsettled disk with $\epsilon = 1$. This is especially true in the outer region of the disk and is in agreement with the results in Figure 2.8 since the more settled disk has a larger molecular layer.

Analyzing the results in more detail at $R = 250$ AU, the model with the most extreme dust settling, $\epsilon = 0.01$, shows more variations from the unsettled disk than the $\epsilon = 0.1$ model does. This is unsurprising, as more dust settling will allow the radiation to penetrate further into the disk and affect the chemical composition more. Looking at the nitrogen-bearing species specifically, HC_3N, N_2H^+, NH and NH_3 are all significantly depleted in the settled disk as compared with the disk with no dust settling. In comparison, CN is slightly enhanced. Almost all of these differences can be traced back to the increase in photodissociation rates in the settled disk. HC_3N and NH_3 are directly photodissociated by the UV radiation, while NH is destroyed by reactions with neutral O that is produced by CO and O_2 photodissociation. In comparison, N_2H^+ is destroyed through reactions with CO, which is enhanced due to the wider molecular layer in the settled disks. Because the settled disk is warmer near the midplane, most of the nitrogen-bearing species are unable to freeze onto dust grains, which leads to an excess reservoir of N in the gas phase. This also serves to increase the column density of CN, which is formed by N reacting with CH and C_2. Surprisingly, HCN does not show a significant depletion in the highly settled disk, despite being strongly dissociated by UV radiation. This is due to the formation of HCN from neutral N working to counteract the photodissociation.

Sulfur-bearing species show a similar pattern, with the higher temperatures in the settled disk leading to very few species frozen-out onto grains. The result of this is

a significant increase in the column density of species such as S, S^+, and SO in the gas-phase. SO_2 is strongly photodissociated, adding to the enhancement seen in SO and O. For the carbon-bearing species, C and C^+ are both slightly enhanced due to the lack of frozen-out species as well as photodissociation (of CO and C respectively). C_2H_4 and CH_4 are both photodissociated by the UV field as expected, leading to the significant depletion of these species in the settled disks.

The lack of water frozen-out onto grains in the settled disks due to photodesorption leads to an increase in the column density of gas-phase oxygen-bearing species such as O. The column density of OH is not enhanced as it is destroyed due to reactions with S^+, which is also enhanced in the settled disk, while H_2O is destroyed due to photodissociation. For some species, such as CO_2 and H_2CO, an increase in the photodissociation leads to a depletion in the column density.

Aikawa & Nomura (2006) explored the vertical distributions of molecules in disks with larger grains and found that the peak abundances are reached at higher A_v values for the cases with larger grains. Our results (e.g., Figure 2.10) are in general agreement with this finding. They found that the column densities of most molecular species did not depend on the size of the dust grains, with the exception of HCO^+ and $H_3{}^+$. The HCO^+ abundance was lower at higher densities, such as disks with larger grains and $H_3{}^+$ was found to be abundant in the cold midplane, which was thinner in the models with dust settling. Our models found a similar trend for $H_3{}^+$, with the abundance decreasing as dust settling increased and the cold midplane shrank. HCO^+ also showed a decrease in column density as dust settling was increased.

2.3.3 Ly α

Largely depending on whether they have a photodissociation cross section at 1216 Å or not, some species are dramatically affected by the presence of Ly α radiation while others are largely unaffected. CO falls in the latter category, with no cross section at 1216 Å and very little change between the models run with and without Ly α radiation included. A clear example of the interaction between Ly α radiation and a cross section at 1216 Å can be seen in Figure 2.11. CN does not have a

photodissociation cross section at 1216 Å and, as a result, we see very little change in abundance between the models with and without Ly α radiation included. HCN, in comparison, has a large cross section at 1216 Å and is strongly depleted when Ly α radiation is included in the model.

However, because of the numerous interconnected reactions, solely knowing the photodissociation cross section is not enough to determine the effect that adding Ly α radiation will have on the abundance of a species. H_2O and OH both have photodissociation cross sections at 1216 Å, but despite this neither species shows a significant depletion due to the presence of Ly α radiation. Figure 2.12 shows that OH is actually slightly enhanced and H_2O is slightly depleted when Ly α radiation is included in the model. These responses are because of the importance of Ly α photodesorption. H_2O(gr) will photodesorb into both H_2O and OH, mitigating the depletion of these species that would otherwise be seen due to photodissociation. Because H_2O(gr) is the dominant oxygen-bearing species for the regions where the temperature is below 100 K, this photodesorption plays a large role in determining the predicted abundances of OH and H_2O. Our treatment of photodesorption seems reasonable, as our maximum abundance for H_2O of a few times 10^{-6} is only slightly higher than the results found in Hollenbach et al. (2009) and Dominik et al. (2005). Assuming that the H_2O abundance is determined solely by a balance between photodesorption and photodissociation, a reasonable assumption based on the rates of those reactions compared to the other formation and destruction reactions of H_2O, we can calculate an estimated abundance of H_2O in the disk by setting those two reaction rates equal:

$$n(\mathrm{H_2O}) \times k_{\mathrm{photodissociation}}\ (\textit{Equation } 2.4) = n(\mathrm{H_2O(gr)} \times k_{\mathrm{photodesorption}}\ (\textit{Equation } 2.10)$$

$$n(\mathrm{H_2O}) \int \sigma(\lambda) J_\lambda d\lambda = F_{\mathrm{UV}} Y \frac{\sigma_{\mathrm{gr}}}{N_{\mathrm{sites}}} N_p \frac{n(\mathrm{H_2O(gr)})}{n_{\mathrm{ice}}} N_m^{-1} n(\mathrm{H_2O(gr)}) \tag{2.19}$$

Here $F_{\mathrm{UV}} = \int J_\lambda d\lambda$. Using an average cross section (σ) for H_2O of $5 \times 10^{-18}\mathrm{cm}^{-2}$, a

photodesorption yield (Y) of 2.36×10^{-3} and assuming that the abundance of all non H_2O species frozen onto grains is negligible, $n_{\rm ice} \sim n_{\rm H_2O(gr)}$, we calculate a maximum H_2O abundance of $\sim 10^{-6}$ for the case of $\epsilon = 0.1$, which matches our results.

The banding features in the H_2O plot with Ly α radiation included and $\epsilon = 0.01$, seen in Figure 2.12 is due to the large amounts of gas-phase CO. With dust settling included, the disk is too warm for CO to freeze-out and, so, the gas phase CO will react with H_3^+ to produce free O atoms that will eventually form H_2O molecules. This produces the wide band of H_2O seen near the midplane in the disk. In comparison, the region of high H_2O abundance seen in the unsettled disk is due to the balance between photodesorption of H_2O(gr) and photodissociation of H_2O. This region exists in the settled disk as well, but at significantly larger heights and is not the cause of the H_2O abundance near the midplane. The band of low H_2O abundance immediately above this high abundance region in the settled plot is due to the thermal structure of the disk.

To more generally see the impact of Ly α radiation on the chemistry of the disk, we have plotted the ratio of column densities for models with and without Ly α radiation included for a variety of species in Figures 2.13. In general, the Ly α radiation has a more dramatic effect when dust settling is included in the model. The more settled disks allow greater penetration of the Ly α radiation, thereby affecting chemistry in a much larger region of the disk. In the case with no dust settling, since the gas and dust opacities are connected the Ly α photons are shielded before they can have much of an effect on the chemical abundances. Unless otherwise stated, the rest of the analysis in this section will be discussing the $\epsilon = 0.01$ case, as the larger effects there are easiest to see and because recent observations indicate that most protoplanetary disks have significant dust settling (Furlan et al., 2008).

Looking at the carbon-bearing species, only a couple of species are strongly depleted. Species, such as C_2H_4 and CH_4, are significantly dissociated in the presence of Ly α radiation. Other species that we would expect to be destroyed, such as C_2H_2, are not. This lack of depletion is mostly due to an increase in the gas-phase abundance of these species that is caused by Ly α photodesorption, similar to what happens

with H_2O. For these species the photodesorption and photodissociation mostly balance each other out, leading to only small changes in the column densities of those molecules. CO_2 is slightly enhanced due to reactions with O and OH, both of which are enhanced in the disk, which counteracts the CO_2 photodissociation.

The chemistry of nitrogen-bearing species is similar to that of the carbon-bearing species. A couple of species are photodissociated by the Ly α radiation as expected, HC_3N, HCN and NH_3, but most of the chemistry is largely unaffected.

The sulfur-bearing species show the most dramatic differences in column densities when Ly α radiation is included. SO_2, as expected, is significantly depleted in the presence of Ly α radiation due to its large photodissociation rate, though only in the highly settled disk with $\epsilon = 0.01$. In the less settled disks, formation reactions between SO and OH or O are quick enough to counteract the photodissociation. SO also has a large cross section at 1216 Å, but is actually enhanced by the presence of Ly α radiation. This occurs largely due to Ly α photodesorption of SO(gr), the photodissociation of SO_2 and the numerous reactions with O and S atoms, both of which are enhanced in the presence of Ly α radiation. For OCS and S, the slight enhancement in abundances are due to Ly α photodesorption of SO which is then photodissociated to form other sulfur-bearing species.

Due to the fact that we have very few on-grain surface reactions in our network, we expect to see a correlation between the gas-phase and on-grain abundances of species. Specifically, species that are photodissociated in the gas phase will be destroyed before they have a chance to freeze out onto grains. Additionally, due to the way we dealt with photodesorption, even if those species that are sensitive to Ly α radiation did adsorb onto dust grains they would be quickly photodesorbed. As a result, the on-grain species that are strongly affected by the presence of Ly α radiation are those that have gas phase photodissociation cross sections at 1216 Å, with the effects being even more dramatic than for the equivalent gas-phase species. As can be seen in Figure 2.14, which plots the column density ratios of some important on-grain species at 250 AU, species such as C_2H_4, CH_4, HCN, NH_3, SO and SO_2 are all strongly depleted in the model with $\epsilon = 0.01$, where Ly α radiation is able to penetrate to the freeze-out

region. These species are either destroyed in the gas phase before they can freeze out on the grains or they are photodesorbed quickly once on a grain surface. One caveat to these results is the potential for hydrogenation of molecules on grains. In our models we have accounted for the hydrogenation of oxygen, which is the main mechanism for water ice formation. This water can be photodesorbed at the disk surface producing water vapor in the molecular layer. It is possible that grain surface hydrogenation of nitrogen or carbon could perhaps lead to an increased formation of species such as NH_3(gr) and CH_4(gr), though this is not included in the current model.

Our initial expectations were that any abundance changes that occurred when Ly α radiation was included in the model would be strongly correlated with the size of a species' photodissociation cross section at 1216 Å. This is clearly not the case and in fact there seems to be little to no correlation at all. The reason for this is that the interdependence of species matters more than just the cross section of a species at 1216 Å. For example, the carbon chemistry in the disk is completely dominated by the reactions involving CO, as seen in Figure 2.6. In the PDR at the top of the disk, all of the carbon is in the form of C^+. Further down in the disk where there is not enough radiation to photodissociate the CO molecule, the carbon exists in the form of CO. Finally, at the midplane the temperatures are low enough for CO to freeze out and the carbon is in the form of CO ice on the grains. There is an interesting region just between the molecular and freeze-out regions in which the temperature is too high for CO to freeze out, but cold enough for other molecules to adsorb onto dust grains. In this region we start to see the presence of more complex molecules frozen out onto the grains, such as C_3, CH_4, HCN and C_2H_2. Even though the reactions that form these molecules are fairly slow compared with the rest of the carbon chemistry, since they are being depleted from the gas phase through adsorption there is enough time to build up a substantial abundance of these more complex species and remove that carbon from the rest of the network.

CO does not have a photodissociation cross section at 1216 Å, which means that any species connected to CO will have only minor changes in abundances when Ly

α radiation is included. This effect can be seen clearly at 250 AU for species such as HCO^+, which is closely connected to CO, and CH_4, which is more weakly connected. The HCO^+ abundance is largely unaffected by the presence of Ly α radiation, while the CH_4 is strongly depleted.

The oxygen-bearing chemistry in the disk is actually fairly simple in that, like the carbon-bearing chemistry, it is dominated by a single species, H_2O. As seen in Figure 2.6, the PDR at the top of the disk is made up completely of free O atoms, which freeze out as water ice as soon as the disk is cold enough to allow it, around 100 K. There is a little oxygen in CO and CO(gr) in the molecular and freeze-out regions respectively, but these are less abundant by a factor of a few than the O and H_2O(gr).

The nitrogen-bearing chemistry is similarly straight-forward. All of the nitrogen in our model starts in the form of N_2, but is quickly dissociated to form neutral N in the PDR. Neither N_2 nor N has a large photodissociation cross section at 1216 Å, so this process is largely unaffected by the presence of Ly α radiation in the UV field. In the molecular layer, a range of nitrogen-bearing species exist, including NH_3 and HCN. Both of these have strong photodissociation cross sections at 1216 Å, so they are destroyed in the highly settled disk models leading instead to a molecular layer made up primarily of N_2. Near the midplane, the nitrogen exists in the form of N(gr) when the temperature is low enough for it to freeze out, which can be seen in Figure 2.6.

The sulfur chemistry is a little more complicated. Figure 2.6 indicates that the primary sulfur-bearing species are S^+ in the PDR and S(gr) in the midplane. However, the sulfur species with large cross-sections at 1216 Å are SO and SO_2. As was discussed above, the photodissociation of SO_2 leads to the formation of SO, which is also formed through photodesorption and reactions between O and S atoms. This means that despite the large cross section at 1216 Å, SO is actually enhanced in the presence of Ly α radiation, though the SO(gr) abundance is depleted.

2.3.4 Comparison with Observations

We have primarily focused on the outer parts of the protoplanetary disk in this chapter because that is the region of the disk probed by current millimeter and submillimeter observations. In Table 2.2 we compare the results of our model with observations taken of three disks: DM Tau, LkCa 15 and TW Hya. The column densities listed for our model were taken at a radius of 250 AU and a time of 10^6 years for each of the dust settling parameters. For each species in the table, the top line includes Ly α radiation while the second line does not. In addition, we present figures of the best-fit models versus the observations with and without Ly α radiation. These can be seen in Figure 2.15.

We did not produce source-specific models for each of these objects, but instead show our results from the generic T Tauri star model described in Section 2.2.1. The objects listed here are all transition disks, which generally have lower accretion rates and larger disk masses (Najita et al., 2007). Despite this, we feel that our models can still provide a decent approximation to the observations for two reasons. First, $\dot{M}/\alpha$, which determines the density structure, is roughly consistent between our model and these objects. For our model, $\dot{M} = 1.0 \times 10^{-8}$ and $\alpha = 1.0 \times 10^{-2}$ so $\dot{M}/\alpha = 1.0 \times 10^{-6}$. Second, the column densities derived from observations are very sensitive to assumptions about the physical structure, adding a level of uncertainty to those values. For most of the species shown here the addition of Ly α radiation does not affect the column densities much. However, for the species that are affected by Ly α radiation, HCN and HNC, the models with Ly α radiation included often produce a better agreement with the observations than those without it. The best-fit model to each set of observations was determined using a two-sample ks-test of the observations with each of the 6 models (3 dust values, with and without Ly α radiation). In all cases the statistics are severely limited as the best fit is determined by so few data points.

DM Tau. Calvet et al. (2005) determined that this object has a stellar mass of 0.65 $M_\odot$, a stellar radius of 1.2 $R_\odot$, a stellar temperature of 3720 K, an accretion rate of 2 $\times 10^{-9}$ $M_\odot$ yr^{-1} and an α of 0.0015, leading to an $\dot{M}/\alpha$ of 1.33 $\times 10^{-6}$. It has a disk

mass of 0.05 $M_\odot$ and the SED was best fit with $\epsilon = 0.1$. The observations are from Dutrey et al. (1997) who determined the gas density distribution of the disk and used this to derive the average fractional abundances with respect to H2, assuming that the fractional abundances were the same everywhere in the disk. Aikawa et al. (2002) used this data and integrated vertically to get the observed column densities listed in Table 2.2. Our models for $\epsilon = 0.1$ produced the best fit to the data, with the model without Ly α radiation included actually fitting the data slightly better, though the ks-test for the models with and without Ly α radiation were similar (Figure 2.15, top left).

LkCa 15. Espaillat et al. (2007) found that this object has a stellar mass of 1.1 $M_\odot$, a stellar radius of 1.7 $R_\odot$, a stellar temperature of 4350 K, an accretion rate of 2.4×10^{-9} $M_\odot$ yr^{-1} and an α of 0.0006, leading to an $\dot{M}/\alpha$ of 4.0×10^{-6}. It has a disk mass of 0.1 $M_\odot$ and the best-fit SED model was with $\epsilon = 0.001$. Looking at our results for $\epsilon = 0.01$ we find that our models are actually a slightly poorer fit to the interferometric data when Ly α is included (Figure 2.15, top right), but our models with Ly α radiation included and $\epsilon = 0.01$ produced the best fit to the single dish observations (Figure 2.15, bottom left). One of the largest differences between our model and the single-dish data occurs in the column densities of H_2CO, where our models significantly underestimate the observed values. This is not unexpected, as Öberg et al. (2009a) has suggested that on-grain reactions can be a critical formation pathway for H_2CO, which is not currently included in our model.

TW Hya. This object has been studied extensively and has been found to have a stellar mass of 0.6 $M_\odot$, a stellar radius of 1.0 $R_\odot$, a stellar temperature of 4000 K (Calvet et al., 2002), an accretion rate of 3.5 $\times 10^{-9}$ $M_\odot$ yr^{-1} (C. Espaillat, private communication) and an α of 0.0025 (Espaillat, private communication), leading to an $\dot{M}/\alpha$ of 1.4×10^{-6}. It has a disk mass of 0.06 $M_\odot$ (Calvet et al., 2002) and the best-fit SED model was with $\epsilon = 0.01$ (Espaillat, private communication). For the observed column densities, the disk was assumed to be 165 AU in radius. Our model with $\epsilon = 0.01$ and no Ly α radiation included produced the best fit to the observations, though again the fit for the model with and without Ly α radiation

were very similar (Figure 2.15, bottom right). In this case the inclusion of Ly α radiation actually produces too little HCN in the model.

Column densities for a larger subset of species from our model can be seen in Table 2.3 for $\epsilon = 0.01$, $R = 250$ AU and time steps of 3×10^5 and 1×10^6 years.

2.4 Discussion and Summary

The existing data sets are quite sparse and our ability to compare between model and observations is somewhat hampered by the methods chosen for column density determination. With these caveats in mind, our best match is obtained with both dust settling and Ly α radiation included. Since both of these features are known to be present in accreting gas-rich disk systems, in particular TW Hya, DM Tau, GM Aur, and LkCa 15, we believe that these physical effects need to be incorporated into protoplanetary disk chemistry models. The dust settling had the expected effect of increasing the UV penetration as the dust settling increases (Dullemond & Dominik, 2004). This changed the size and location of the molecular layer and freeze-out regions, which in turn affected the column densities of molecules in the disk. Most of the differences that occurred between the different dust settling models came about due to an increase in photodissociation reaction rates as dust settling increased. In addition, the smaller freeze-out regions of the settled disks allowed species such as N_2H^+ to be depleted due to the increased molecular layers in those disks. Some of these changes were multiple orders of magnitude effects and since most disks appear to be heavily settled, (D'Alessio et al., 2006; Furlan et al., 2006) leaving dust settling out of protoplanetary disk models will produce results that are less likely to match observations. For the few objects where we were able to compare our results with observations, all three disks were fit best with a disk where some dust settling was included.

As with dust settling, the inclusion of Ly α radiation transfer to the protoplanetary disk model had a significant effect on the resulting chemical abundances. While not all species with large photodissociation cross sections at 1216 Å were heavily depleted, many species had column densities that were changed by an order of magnitude or

more. Some of the most depleted species included HC_3N, HCN, NH_3, SO_2, C_2H_4 and CH_4, all of which were strongly photodissociated by the inclusion of Ly α radiation. In addition, some species had column densities that were enhanced, such as S, SO and CO_2, due to the photodissociation of other species with cross sections at 1216 Å.

For some species, the effects of Ly α induced photodesorption played a large role in determining how that species was affected by the inclusion of Ly α radiation. Species such as H_2O and OH had their abundances increased due to Ly α photodesorption which counteracted the destruction of these molecules by photodissociation.

Comparing the results from our models with the observations of three disk systems indicated that in general the models with Ly α radiation included produced similar or slightly better fits to the data. However the statistics on these fits were very limited as only a handful of species were observed and only two of those were species that were affected by the presence of Ly α radiation. Despite this, we feel it is promising that the models with Ly α radiation included in them often produced better fits than those without Ly α radiation.

As mentioned previously, the most molecule rich disks all have indications of either strong Ly α emission (e.g., TW Hya) or broad Ly α wing emission (e.g., DM Tau, GM Aur and LkCa 15). In both of these cases there is also indirect evidence for Ly α emission through fluorescent lines of molecular hydrogen. Therefore we believe that Ly α emission is an intrinsic feature of most, if not all, accreting disks. Our models have shown that the inclusion of both Ly α radiation (and specifically Ly α radiation transfer) and dust settling are important components for understanding disk chemistry. At present the observational data do not allow for definitive statements regarding which physical effect dominates, but this will change as we head into the age of ALMA.

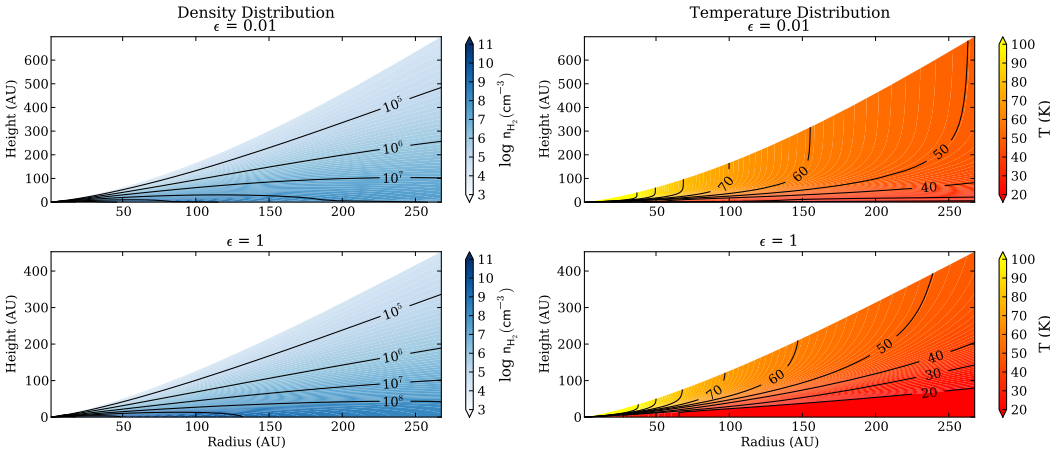

Figure 2.1. Density (*left*) and Temperature (*right*) structure of a disk model with $\epsilon = 0.01$ and $\epsilon = 1$. The model was run with the parameters for a typical T Tauri star with radius $R_* = 2\ R_\odot$, mass $M_* = 0.5\ M_\odot$, mass accretion $\dot{M} = 10^{-8} M_\odot \mathrm{yr}^{-1}$ and temperature $T_* = 4000$ K (e.g., Kenyon & Hartmann, 1995). The dust composition and settling were taken from D'Alessio et al. (2006) with $\mathrm{a}_{\mathrm{max,\ small}} = 0.25\ \mu$m and $\mathrm{a}_{\mathrm{max,\ large}} = 1.00$ mm.

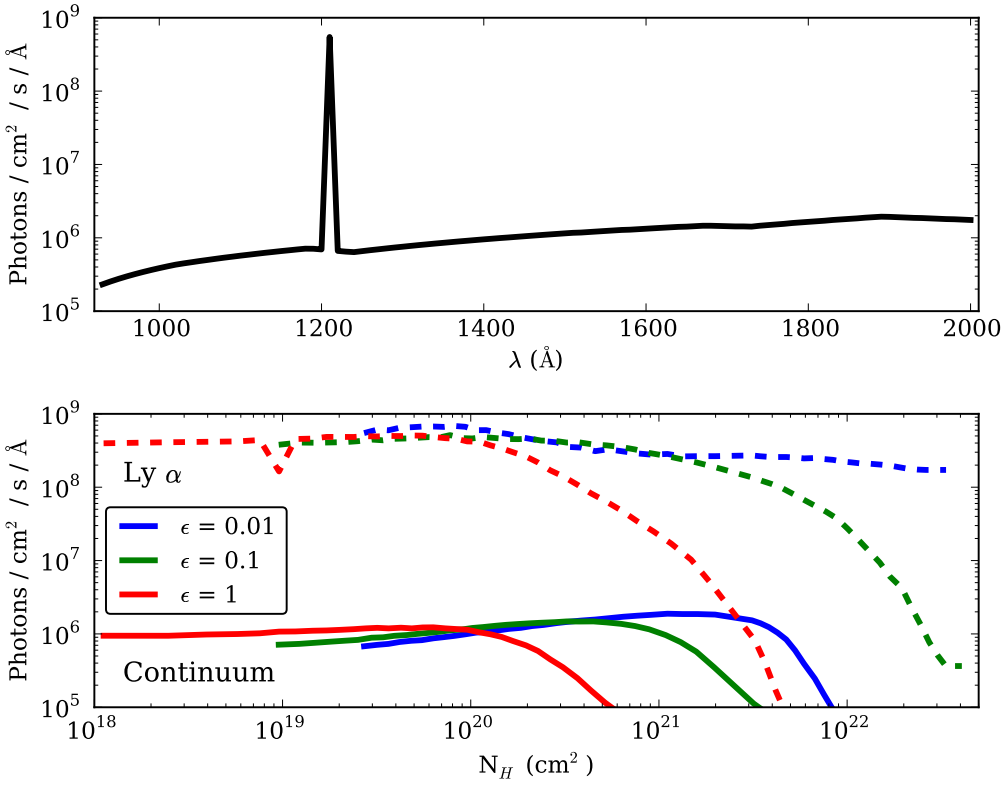

Figure 2.2. Top Panel: sample stellar UV field from Bethell et al. (2010). This example was taken from just below the top of the disk for a radius of 208 AU and an ϵ of 0.01. Bottom Panel: the effects of scattering and attenuation on the UV field in the disk. Solid lines are the continuum, dashed lines are Ly α radiation.

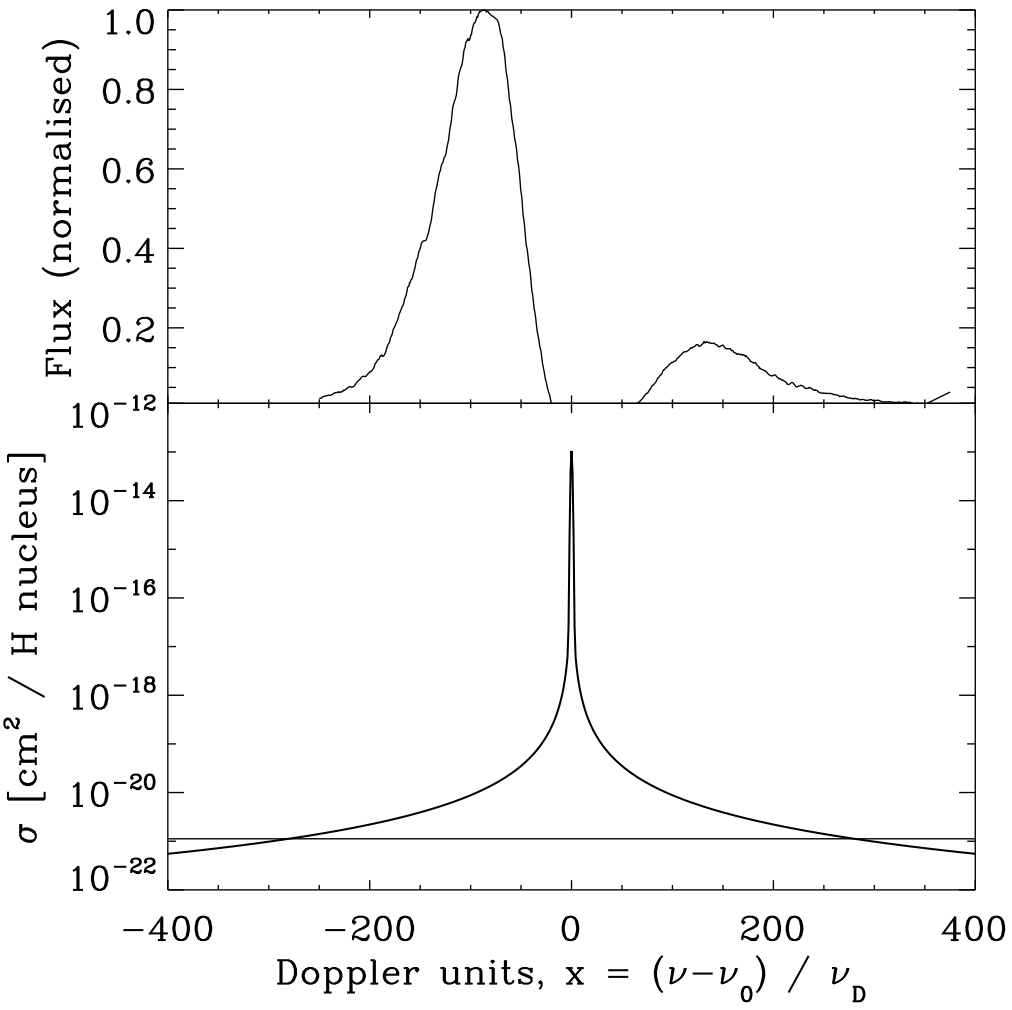

Figure 2.3. Stellar Ly α line profile of TW Hya (upper panel, taken from Herczeg et al. 2002) and resonant scattering (Voigt) profile due to HI atoms in the disk (lower panel). The horizontal line in the lower panel represents the dust opacity.

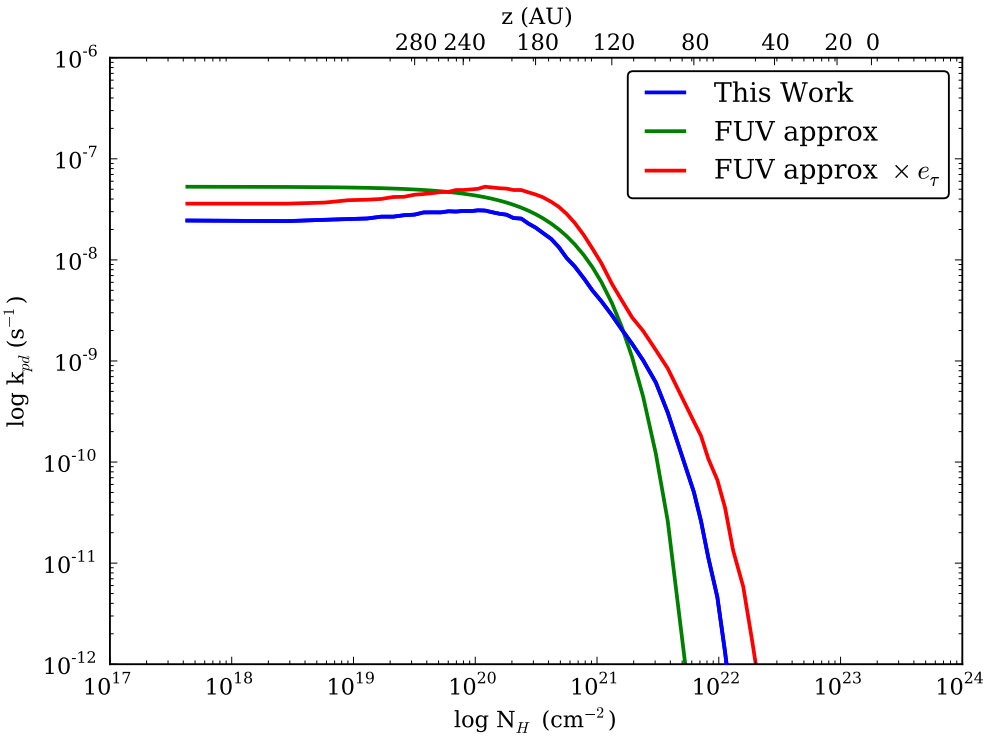

Figure 2.4. Plot of three different photodissociation rates of HCN at radius $R = 208$ AU and $\epsilon = 1$. The dashed line (FUV approx) assumes a normal ISRF scaled to match the FUV flux of a typical T Tauri star without any scattering included. The dotted line (FUV approx $\times$ e_τ) includes e_τ, which incorporates the attenuation and scattering of the UV field in the disk. The solid line is the result of calculating the photodissociation rate from the wavelength-dependent cross section of HCN.

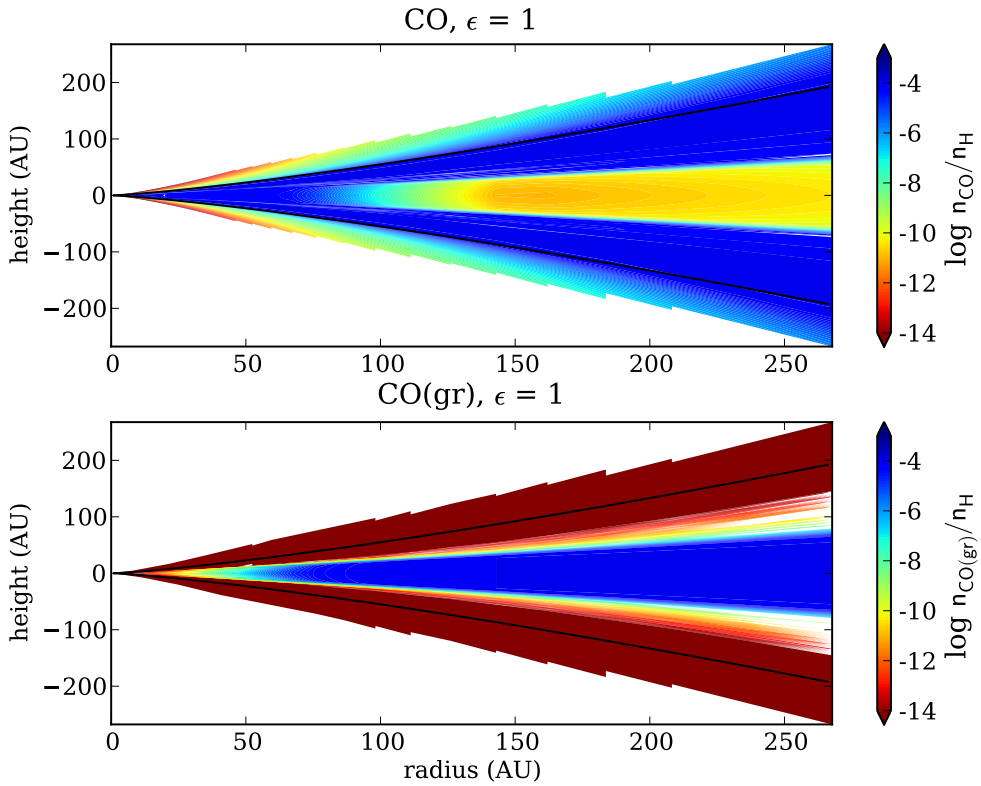

Figure 2.5. Contour plot of CO and CO(gr) abundances for a model with no dust settling included. The solid lines indicate the $\tau = 1$ surface in the disk.

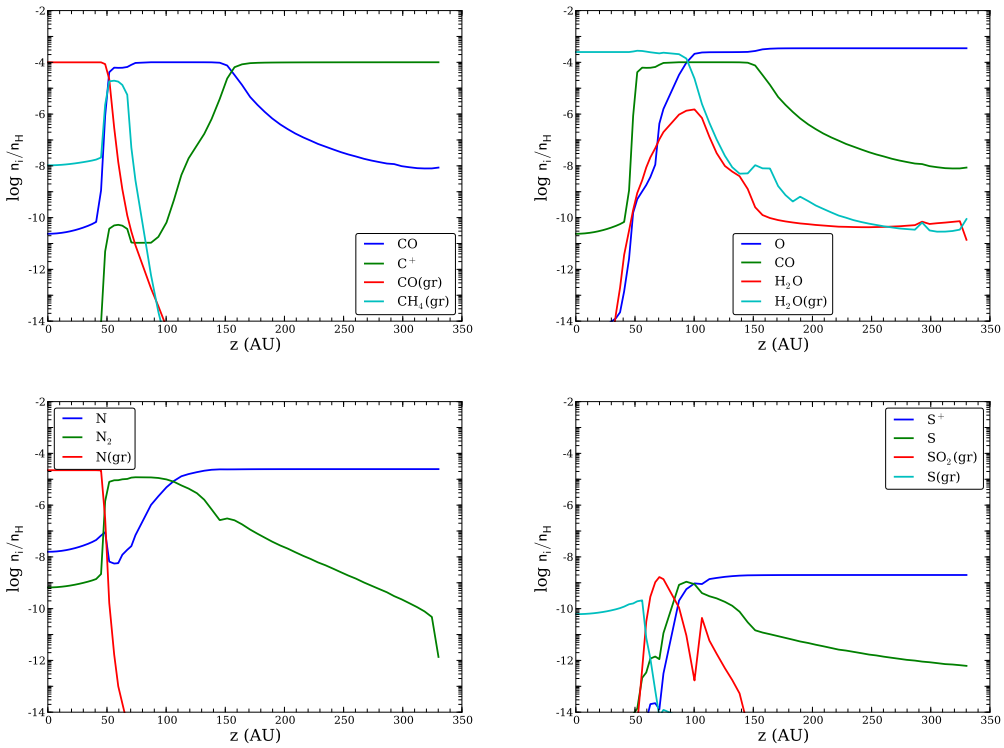

Figure 2.6. Plot of the vertical distribution of relative abundances of carbon-bearing (top left), oxygen-bearing (top right), nitrogen-bearing (bottom left) and sulfur-bearing (bottom right) molecules at $R = 208$ AU and $\epsilon = 1$.

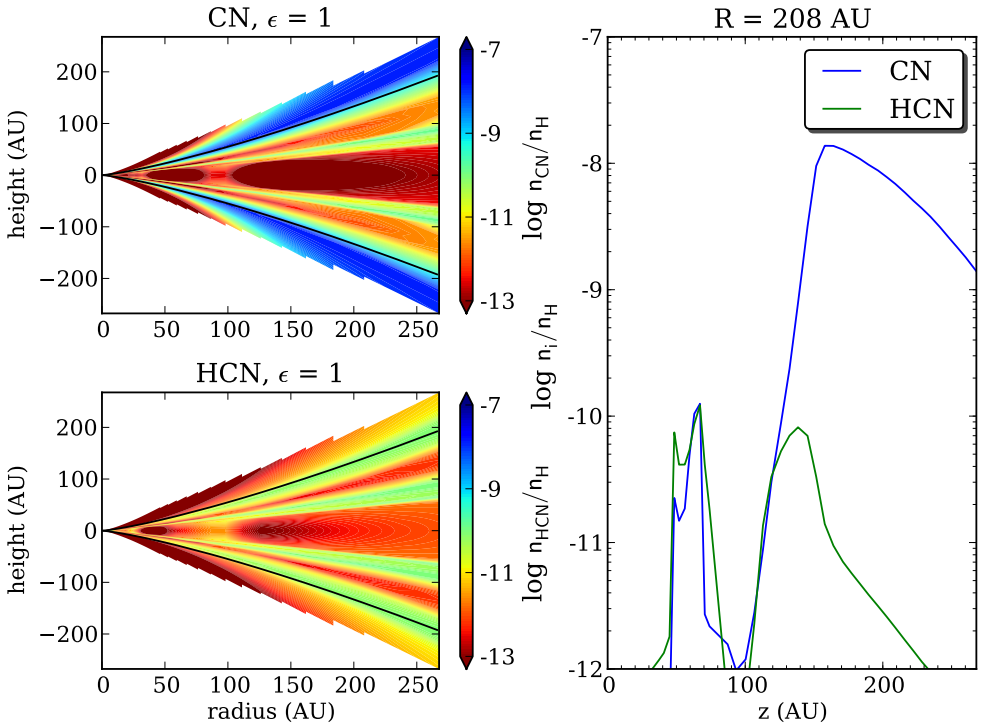

Figure 2.7. Left Panels: contour plots of the abundances of CN (top) and HCN (bottom) for a disk model with $\epsilon = 1$. The solid lines indicate the $\tau = 1$ surface in the disk. Right Panel: plot of the vertical distribution of the abundance of CN and HCN in the disk at $R = 208$ AU and $\epsilon = 1$. The peak at z $\sim$ 100 AU is due to the UV field being shielded, but the temperatures remaining high enough for CN and HCN to exist in the gas phase. The HCN abundance falls off more quickly than the CN abundance at high z values due to reactions with C^+, which is abundant in the PDR and destroys HCN molecules.

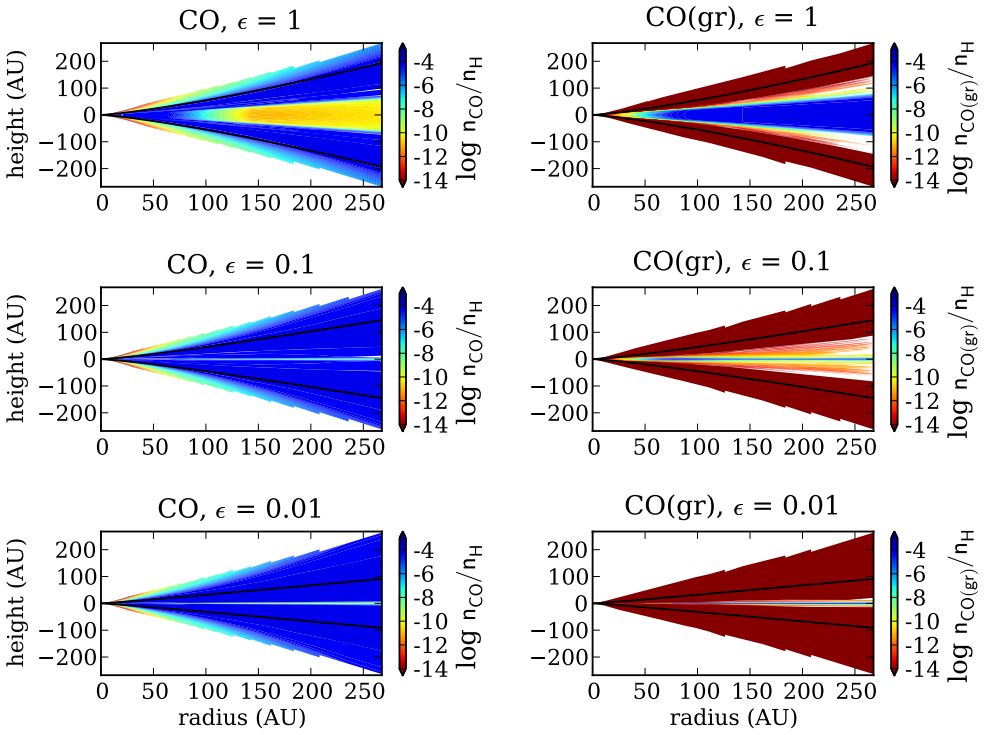

Figure 2.8. Contour plot of CO and CO(gr) abundances for models with three different ϵ values. The solid lines indicate the $\tau = 1$ surface in the disk.

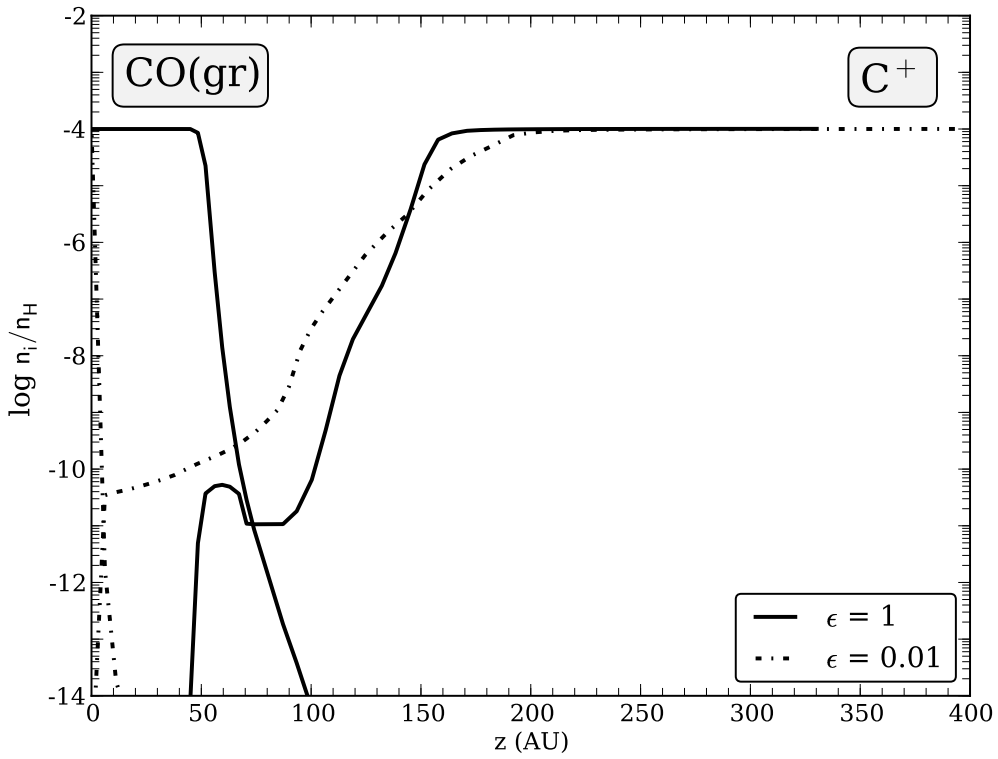

Figure 2.9. Plot of C^+ and CO(gr) vs. height at $R = 208$ AU for dust settling parameters of $\epsilon = 1$ and $\epsilon = 0.01$.

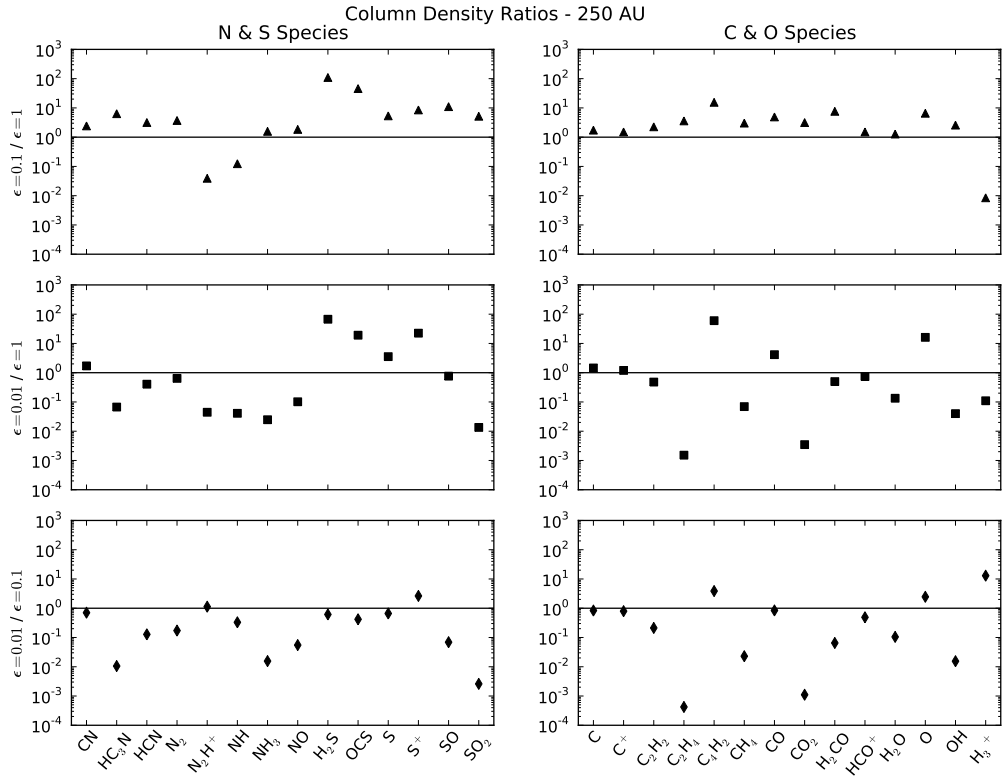

Figure 2.10. Column density ratios for models with different dust settling parameters, computed at 250 AU.

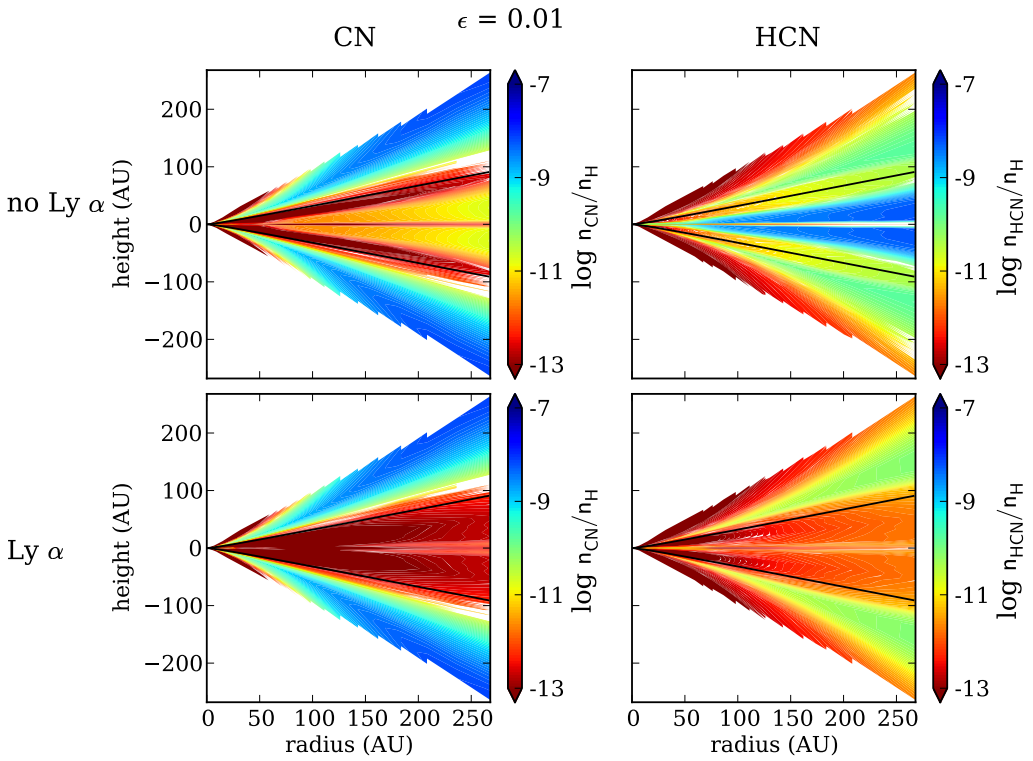

Figure 2.11. Top Panels: contour plot of the abundance of CN (left) and HCN (right) for a model with $\epsilon = 0.01$ and no Ly α radiation. Bottom Panels: contour plot of the abundance of CN (left) and HCN (right) for a model with $\epsilon = 0.01$ and Ly α radiation included.

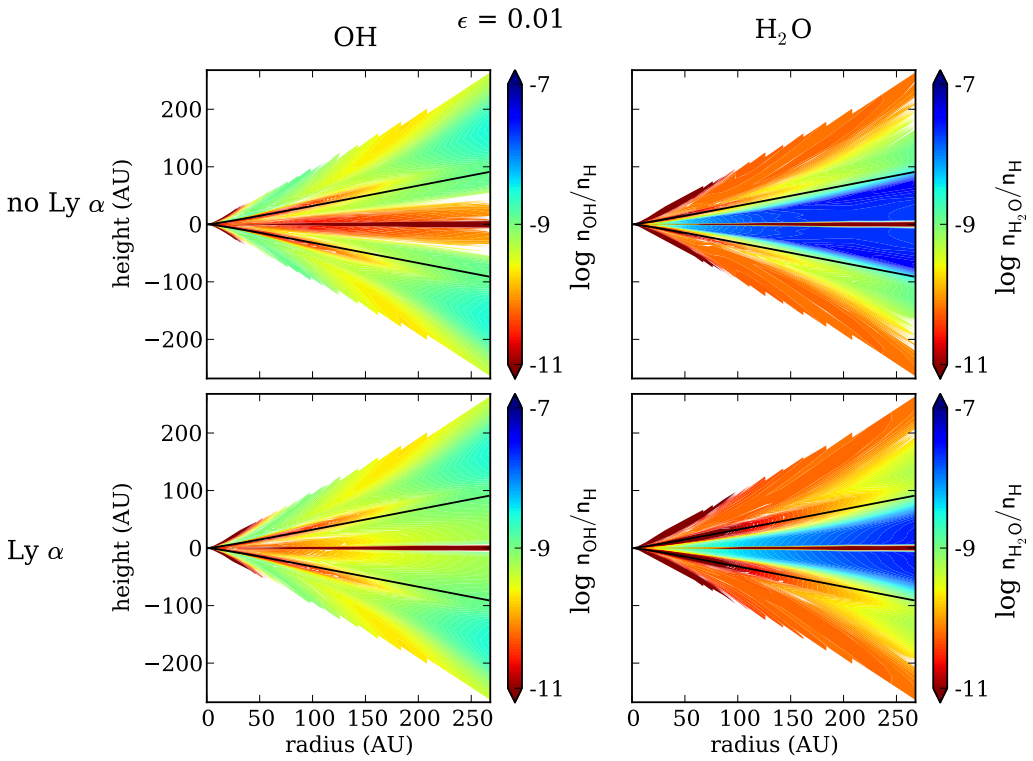

Figure 2.12. Top Panels: contour plot of the abundance of OH (left) and H_2O (right) for a model with $\epsilon = 0.01$ and no Ly α radiation. Bottom Panels: contour plot of the abundance of OH (left) and H_2O (right) for a model with $\epsilon = 0.01$ and Ly α radiation included.

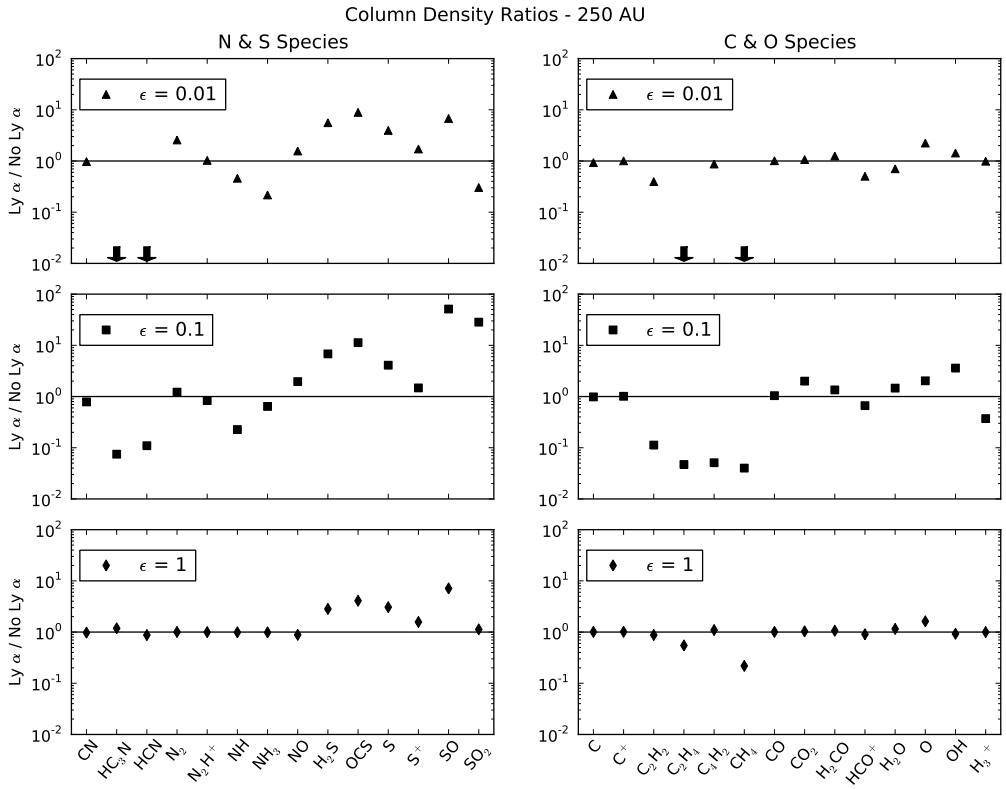

Figure 2.13. Column density ratios for models with and without Ly α radiation included, computed at 250 AU.

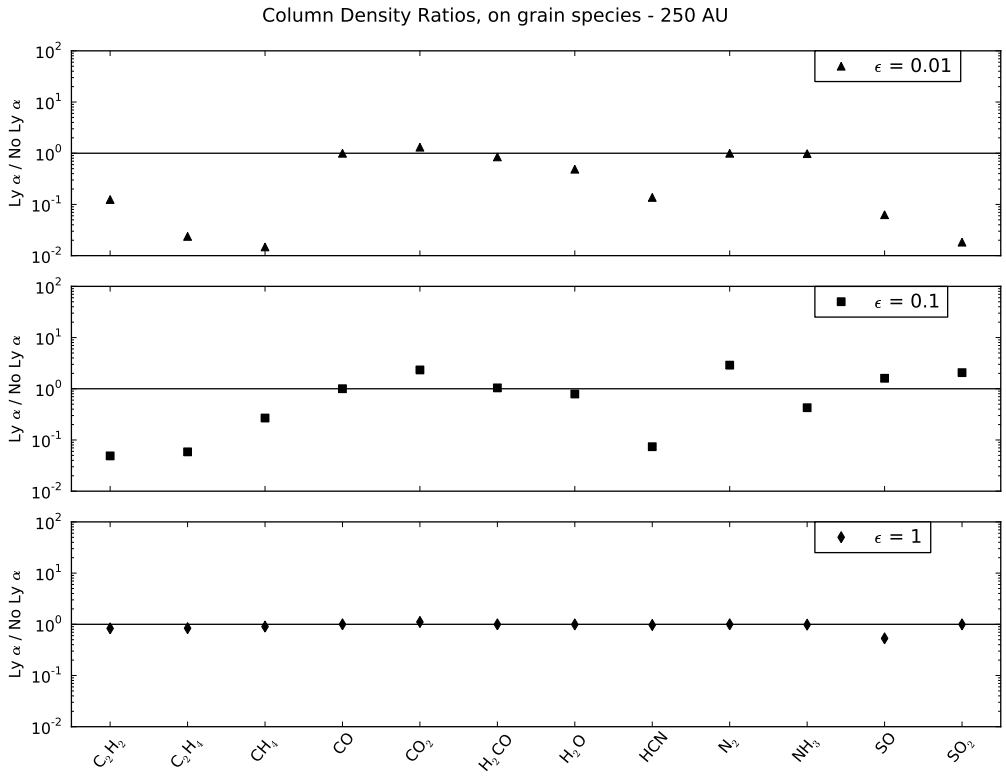

Figure 2.14. Column density ratios of on-grain species for models with and without Ly α radiation included, computed at 250 AU.

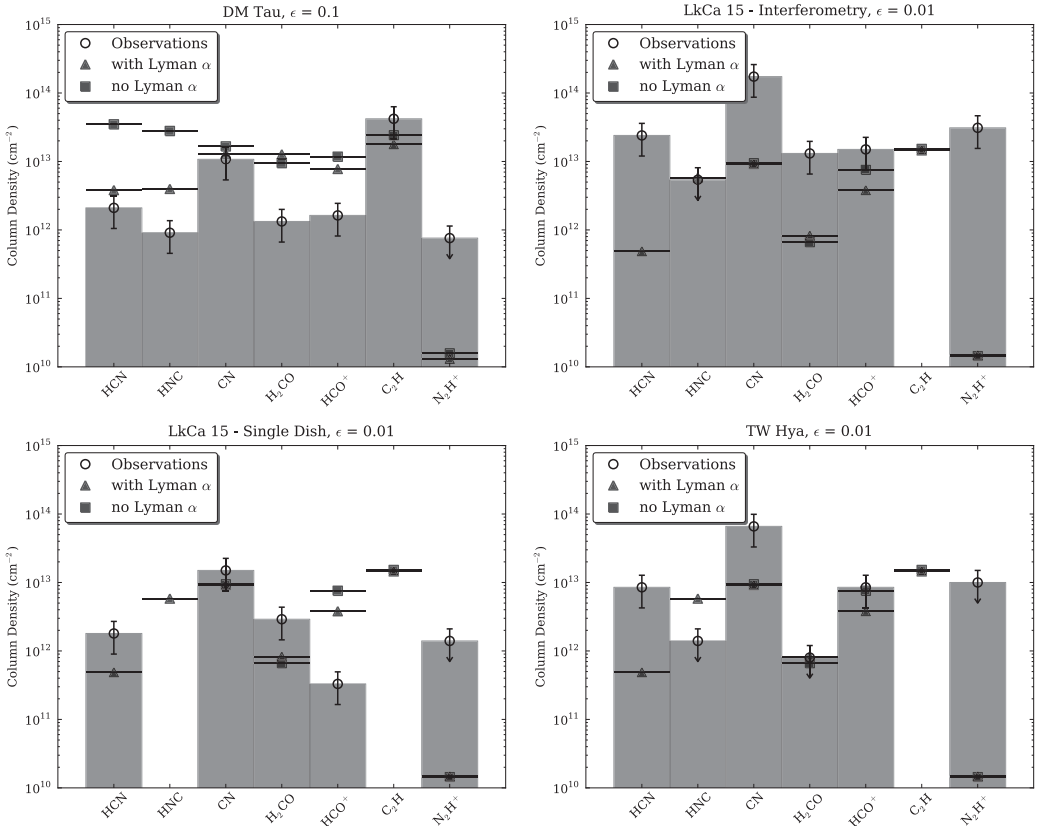

Figure 2.15. Figures comparing our model with $\epsilon = 0.01$ (except for DM Tau, which is $\epsilon = 0.1$) and observations of three disks. The gray bars and open circles represent the observations, with error bars of 50%. The triangles show our model with Ly α radiation included and the squares show our model with Ly α radiation not included.
Top left: DM Tau (Aikawa et al., 2002), $\epsilon = 0.1$.
Top right: LkCa 15, Interferometric observations (Qi, 2001; Qi et al., 2003; Aikawa et al., 2003).
Bottom left: LkCa 15, single-dish observations (Thi et al., 2004).
Bottom right: TW Hya (Thi et al., 2004; van Dishoeck et al., 2003).

Table 2.1. Initial Abundances[a]

Species	Abundance	Species	Abundance
H	1.00	CO	1.00E-4
He	1.40E-1	N_2	1.00E-6
N	2.25E-5	C	7.00E-7
CN	6.00E-8	NH_3	8.00E-8
H_3^+	1.00E-8	HCN	2.00E-8
S^+	1.60E-6	C^+	1.00E-8
Si^+	1.60E-9	HCO^+	9.00E-9
Mg^+	3.00E-8	H_2CO	8.00E-9
Fe^+	2.00E-8	C_2H	8.00E-9
H_2O(gr)	2.50E-4	CS	2.00E-9
GRAIN	6.00E-12		

[a] The initial abundances are by number density relative to the total hydrogen abundance.

Table 2.2. Comparison of the Model with Observations

	Models			LkCa 15			
Species	$\epsilon = 1$	$\epsilon = 0.1$	$\epsilon = 0.01$	DM Tau[a]	Interferometer[b]	Single Dish[c]	TW Hya[c]
H_2	8.3 (22)	3.8 (22)	3.1 (22)	3.8 (21)	···	···	···
	8.3 (22)	3.8 (22)	3.1 (22)				
CO	1.2 (18)	6.0 (18)	5.1 (18)	5.7 (16)	1.7 (18)[d]	1.9 (16)	3.2 (16)
	1.2 (18)	5.8 (18)	5.0 (18)				
HCN	1.2 (12)	3.8 (12)	4.9 (11)	2.1 (12)	2.4 (13)	1.8 (12)	8.5 (12)[e]
	1.4 (12)	3.5 (13)	1.4 (14)				
HNC	1.2 (12)	4.0 (12)	5.8 (12)	9.1 (11)	<5.4 (12)	···	<1.4 (12)
	1.3 (12)	2.8 (13)	1.2 (14)				
CN	5.4 (12)	1.3 (13)	9.2 (12)	9.5-12 (12)	9.7-25 (13)	1.5 (13)	6.6 (13)
	5.5 (12)	1.7 (13)	9.4 (12)				
H_2CO	1.7 (12)	1.3 (13)	8.3 (11)	7.6-19 (11)	7.2-19 (12)[f]	7.1-51 (11)	<8.0 (11)
	1.6 (12)	9.5 (12)	6.6 (11)				
HCO^+	5.2 (12)	7.8 (12)	3.8 (12)	4.6-28 (11)	1.5 (13)	3.3 (11)	8.5 (12)[e]
	5.7 (12)	1.2 (13)	7.6 (12)				
C_2H	6.8 (12)	1.8 (13)	1.5 (13)	4.2 (13)	···	···	···
	6.9 (12)	2.4 (13)	1.5 (13)				
N_2H^+	3.3 (11)	1.3 (10)	1.5 (10)	<7.6 (11)	3.1 (13)[d]	<1.4 (12)	<1.0 (13)
	3.4 (11)	1.6 (10)	1.4 (10)				

Model column densities (cm^{-2}) are calculated at $t = 1 \times 10^6$ yr and $R = 250$ AU. For each species, the first row includes Ly α radiation while the second line does not. The table of observations was compiled by Willacy (2007).

[a] Aikawa et al. (2002, derived from Dutrey et al. 1997).

[b] Qi (2001) unless otherwise noted.

[c] Thi et al. (2004) unless otherwise noted.

[d] Qi et al. (2003).

[e] van Dishoeck et al. (2003).

[f] Aikawa et al. (2003).

Table 2.3. Column Densities at $\epsilon = 0.01$ and $R = 250$ AU[a]

Species	3×10^5 yr	1×10^6 yr	Species	3×10^5 yr	1×10^6 yr
C	1.183×10^{15}	1.188×10^{15}	HCN	5.250×10^{11}	4.885×10^{11}
C^+	3.271×10^{16}	3.282×10^{16}	N	1.017×10^{18}	1.043×10^{18}
C_2H_2	3.228×10^{11}	3.229×10^{11}	N_2	1.175×10^{17}	1.045×10^{17}
C_2H_4	4.647×10^5	4.492×10^5	N_2H^+	2.150×10^{10}	1.484×10^{10}
C_3H_2	6.682×10^{10}	6.689×10^{10}	NH	3.643×10^{11}	2.474×10^{11}
C_4H_2	1.768×10^{10}	1.769×10^{10}	NH_3	1.484×10^{11}	1.157×10^{11}
CH_4	1.816×10^{12}	1.744×10^{12}	NO	3.491×10^{13}	3.134×10^{13}
CN	9.151×10^{12}	9.160×10^{12}	O	9.123×10^{18}	1.019×10^{19}
CO	5.085×10^{18}	5.085×10^{18}	O_2	2.037×10^{15}	2.111×10^{15}
CO_2	2.000×10^{11}	1.693×10^{11}	OCS	1.856×10^9	1.534×10^9
H_2	3.126×10^{22}	3.127×10^{22}	OH	4.639×10^{13}	4.253×10^{13}
H_2CO	9.022×10^{11}	8.270×10^{11}	S	1.027×10^{13}	8.855×10^{12}
H_2O	6.234×10^{14}	6.172×10^{14}	S^+	8.713×10^{13}	8.580×10^{13}
H_2S	9.149×10^9	7.222×10^9	S_2	1.520×10^5	7.997×10^4
$H_3{}^+$	2.016×10^{12}	2.024×10^{12}	SO	1.602×10^{11}	1.300×10^{11}
HCO^+	3.892×10^{12}	3.810×10^{12}	SO_2	4.937×10^8	5.013×10^8
HC_3N	6.732×10^7	6.699×10^7			

[a] Column densities are all in cm^{-2}.

CHAPTER 3

X-ray Opacity and Ionization Fraction

3.1 Introduction

Observations of protoplanetary disks indicate that they generally have mass accretion rates onto the central star of about 10^{-8} $M_\odot$ / yr (Hartmann et al., 1998), but achieving this requires a mechanism for the transport of angular momentum through the disk. Current theories point to magnetohydrodynamic (MHD) turbulence generated by magnetorotational instability (MRI; Balbus & Hawley, 1991) as the primary source for this angular momentum transport. This process requires that the gas in the disk be sufficiently ionized that the neutral component of the gas can be coupled to the magnetic field via ion-neutral collisions.

Angular momentum transport and turbulence are factors not only in building up the stellar mass, but also for understanding the evolution and formation of planets as planetesimal and proto-planet growth are dependent on the velocity dispersion of material (e.g., Wetherill & Stewart, 1993; Kokubo & Ida, 2000; Thommes et al., 2003). In addition, 'dead' zones, regions without enough ionization for turbulence, provide a calm region for planet formation and planet migration (Matsumura et al., 2009). It is therefore necessary to obtain a detailed understanding of the structure of turbulent disks and the angular momentum transport mechanisms in order to fully understand planet formation.

MRI requires $x_e \gtrsim 10^{-13}$ in the gas for it to be active and efficient in powering disk accretion (Gammie, 1996; Perez-Becker & Chiang, 2011). In general the electron abundance x_e can be written as:

$$x_e \approx \sqrt{\frac{\xi}{\beta n_H}} \tag{3.1}$$

where ξ is the ionization rate, β is the recombination coefficient and n_H is the number density of hydrogen. For an attenuated cosmic ray ionization rate of 2.7×10^{-18} s^{-1}, $\beta = 2 \times 10^{-6}$ $T^{-1/2}$ cm^3 s^{-1} (Igea & Glassgold, 1999) and midplane density at R = 5 AU of 1.2×10^{13} cm^{-3} (Hayashi, 1981) this leads to $x_e = 9.4 \times 10^{-13}$, marginally satisfying the condition that the disk is sufficiently ionized for it to be active, but indicating that inside of 5 AU it will be dense and therefore inactive. The simplest ionization mechanism that generates sufficient ionization levels is collisional ionization. However, collisional ionization requires very high temperatures, T > 1000 K, to be efficient which exist only in the innermost regions of the protoplanetary disk closest to the central star. At R $\gtrsim$ 0.1 AU, where most of the mass resides, non-thermal mechanisms such as the decay of radionuclides, UV radiation, X-ray radiation from the central star (Glassgold et al., 1997) and cosmic rays (Umebayashi, 1983), must play important roles in determining the ionization fraction of the disk.

Table 3.1 lists the non-thermal processes along with the region of the disk in which they will affect the chemistry, based on the effective column needed to shield the disk from that radiation and prevent ionization. The highest energy UV radiation is able to penetrate to a mass column of 1.3×10^{-3} g cm^{-2}, meaning that the upper layers of the disk is ionized due to UV radiation. In the molecular layer of the disk, the UV radiation is now shielded, but X-rays and cosmic rays are still able to produce electrons as they can penetrate to mass columns of 2.1 g cm^{-2} and 96 g cm^{-2} respectively. In the midplane, the mass column is likely to be too great for X-rays to penetrate and the only ionizing source remaining is cosmic rays. In addition, dust settling will affect how far the UV and X-ray (Bethell & Bergin, 2011) radiation penetrates into the disk, which may allow for ionizing mechanisms to affect a much greater portion of the disk mass than would otherwise be possible.

Under this schematic, the protoplanetary disk can be separated into an 'active' region near the disk surface, where the ionization fraction is high enough for the

neutral gas to couple to the magnetic field, and a 'dead' region near the midplane, which has few ions and is decoupled from the magnetic field. The active layer of the disk is unstable due to the MRI, leading to turbulence and angular momentum transport in the disk (e.g., Gammie, 1996; Sano et al., 2000; Fleming & Stone, 2003; Balbus, 2003, and references therein).

The specific fraction of the disk that is active vs. dead is highly dependent on the physical and chemical composition of the disk. Previous studies have looked at the effects of small-scale networks on the ionization fraction (e.g., Ilgner & Nelson, 2006; Semenov et al., 2004) and explored a variety of physical disk structures, from a layered α-disk model (Gammie, 1996), to a minimum mass solar nebula model from Hayashi (1981) (Sano et al., 2000), to an externally heated, passive disk (Matsumura & Pudritz, 2003), to a disk with UV heating from the central star and internal viscous heating (Semenov et al., 2004). Ilgner & Nelson (2006) and Semenov et al. (2004) looked at the effect of the chemical network complexity on the ionization fraction in the disk and found significant differences in the location and size of the dead zone between the simplest and most complex chemical networks.

The dominant charge carriers in each layer consist of H^+ and C^+ in the upper layer, HCO^+, $H_3{}^+$ and H_3O^+ in the molecular region and HCO^+ and N_2H^+ in the midplane (Semenov et al., 2004). Of these molecules, HCO^+ and N_2H^+ have both been observed in protoplanetary disks with current instruments (e.g., Dutrey et al., 1997; Qi et al., 2003; Dutrey et al., 2007a; Kastner et al., 2008; Öberg et al., 2010). One important factor to consider is the effect of dust settling on the presence and location of these charge carriers, which is relatively unexplored. This omission is despite the fact that dust settling is seen in many disks (e.g., Sicilia-Aguilar et al., 2004; Furlan et al., 2006) and that dust settling plays a large role in the radiation penetration into the disk (e.g., Dullemond & Dominik, 2004). Dust settling will affect which species are dominant in disk regions, both radially and vertically.

For this chapter we have taken the full disk chemical model presented in Fogel et al. (2011), which includes cosmic ray ionzation, dust settling dependent UV ionization and gas-grain reactions, and added dust settling dependent X-ray ionization cross-

sections from Bethell & Bergin (2011) in order to analyze the resulting active zone in the protoplanetary disk. In Section 3.2 we briefly describe the model used and the sources of ionizing radiation. In 3.3.1 we look at the effects on chemical abundances of including dust-settling dependent X-ray opacities, in Section 3.3.2 we present the ionization fraction and active zones resulting from the model runs, and in Section 3.4 we discuss the implications of these results on the overall disk chemistry and on mass accretion in the disk.

3.2 Model

A more detailed description of the chemical model and network used can be found in Chapter 2. Here, we review some of the important details of the model as well as any modifications made. We used the physical structure from D'Alessio et al. (2006), who provided several models tracing a range of dust settling values. The dust settling parameter, ϵ, is defined as the dust-to-gas mass ratio of the small grains in the upper regions of the disk relative to the standard dust-to-gas mass ratio (D'Alessio et al., 2006). A value of $\epsilon = 1$ means that no settling has taken place, while a smaller value of ϵ indicates a depletion of dust grains in the upper regions of the disk and a corresponding increase in large dust grains near the midplane. The disk extends to 400 AU and orbits around a typical T Tauri star of radius $R_* = 2\ R_\odot$, mass $M_* = 0.5\ M_\odot$, mass accretion rate $\dot{M} = 10^{-8} M_\odot\ \mathrm{yr}^{-1}$ and temperature $T_* = 4000$ K (e.g., Kenyon & Hartmann, 1995). We include ionization from cosmic rays, UV photonionization and X-rays, which is described in more detail below.

3.2.1 Ionization Sources

The ionization rates used strongly affect the location of the active zone in a disk. For the model presented in this chapter we only include chemical species composed of H, He, C, O and N. Other species, such as those composed of Fe, Mg, Si and S, are depleted in pre-stellar cores (Maret & Bergin, 2007) and thus we assume they are not present in significant quantities in the gaseous state in protoplanetary disks. However, we do assume they are incorporated into grains and present as absorbing

material. In addition, we do not include the effects of ionization by radionuclides. Work by Umebayashi & Nakano (1981); Ilgner & Nelson (2006) have shown that the ionization rate of radionuclides is small compared with that for stellar X-rays and cosmic rays for all regions of the disk except for the inner 1 AU. Finally, we also do not include thermal ionization in our model. Again, this effect is significant only in the very inner region of the disk. For this chapter we are focusing primarily on the outer regions of the disk where most of the mass resides, thus radionuclides and thermal ionization will not change the results presented.

Cosmic Ray Ionization

For cosmic ray ionization we have followed the formalism presented by Semenov et al. (2004) with cosmic rays striking the disk vertically on both sides of the disk with an attenuation column of 96 g cm^{-2} (Umebayashi & Nakano, 1981) and an unshielded cosmic ray ionization rate of 1.3×10^{-17} s^{-1}.

UV Photonionization

The UV photoionization is calculated using Equation 2.6, the same method as the photodissociation rate for those species that did not have measured cross sections in Section 2.2.3. An illustration of how dust settling affects UV penetration can be seen in this simple calculation in Equation 2.5. The visual extinction in the disk as a function of the gas-to-dust mass ratio, ξ, can be calculated (from Bergin, 2011) as

$$A_V = 1.086 \frac{3}{4} \frac{\xi \mu m_H}{\rho_{gr} a_{gr}} N Q_V \sim \left(\frac{\xi}{0.01} \right) \left(\frac{Q_V}{1} \right) 10^{-21} N \tag{3.2}$$

where ξ is the gas-to-dust mass ratio, Q_V is the extinction efficiency in the visible wavelengths and N is the column density. Dust settling means that dust is removed from the upper layers while the gas is untouched. This leads to a large decrease in the gas-to-dust mass ratio, ξ, in the upper layers of the disk, which in turn allows for greater penetration of the UV radiation in a given gas column. Including dust settling is therefore necessary to properly treat the penetration and effects of UV radiation in protoplanetary system (van Zadelhoff et al., 2003; Dullemond & Dominik, 2004; Fogel

et al., 2011; Vasyunin et al., 2011) and to determine the location and abundance of ionized species.

X-ray Ionization

Observations of T Tauri stars have shown that they emit strongly in X-rays, with luminosities between 10^{28} - 10^{31} erg s^{-1} (Glassgold et al., 1997; Feigelson & Montmerle, 1999; Flaccomio et al., 2009). Bethell & Bergin (2011) analyzed the effects of dust settling on the X-ray opacity in protoplanetary disks and found that there is a floor to the X-ray opacity, at which point further dust settling did not further decrease the opacity. More specifically, as the metal rich grains settle there are fewer metals in the upper layers of the disk to absorb the X-rays. However, once dust grains are completely settled there are still some volatiles in the gas (e.g., CO) that are able to absorb the X-rays and these species produce the floor on the X-ray opacity. Figure 3.1 demonstrates how this dust settling dependence affects the overall X-ray opacity. As with the UV radiation, dust settling allows for the X-ray radiation to penetrate further into the disk, in this case by decreasing the opacity by almost an order of magnitude when ϵ changes from 1.0 to 0.001 for 10 keV X-rays. This increases the penetration depth of the most energetic X-rays, those at 10 keV, from 2.1 g cm^{-2} to 14.3 g cm^{-2}. This effect, as well as UV photolysis induced by X-rays (Aikawa & Herbst, 1999, 2001), are included in our model.

3.3 Results

Our standard model can be seen in Chapter 2.3 and in this section we explore the deviations from that standard model. In Section 3.3.1 we discuss the effects of including dust settling dependent X-ray opacities on chemical abundances as well as the location of ionized species in the disk. In Section 3.3.2 we analyze the ionization fraction and dead zone locations in our disk and in Section 3.3.3 we look at the effects of dust settling on the dead zone location.

3.3.1 Dust Settling Dependent X-ray opacity and Molecular Composition

In this section we analyze the effects of including dust-dependent X-ray opacities on the chemistry of the disks. Figure 3.2 plots the percent change in abundance for several important species when the dust-dependent X-ray opacity is included. These plots were made for a model with $\epsilon = 0.001$ and $L_x = 10^{31}$ ergs s^{-1}. Those parameters were chosen to highlight any dust-dependent effects. Blue indicates an increase in the abundance of that species while yellow or red indicates a decrease in the abundance of that species and green indicates no change.

Not surprisingly, the abundance of CO exhibits little change when dust-dependent X-ray opacities are included in the model. While slightly more of the carbon is in the form of C^+, as shown in the upper right panel of Figure 3.2, this does not alter the abundance of CO. The other four plots in this figure show the species that make up the majority of the ionization fraction in the disk, H^+, HCO^+, $H_3{}^+$ and H_3O^+. For these species there is an increase in abundance when the X-ray opacity is decreased due to dust depletion. This is as expected, as the further penetration of the X-rays directly produces more $H_2{}^+$ in the disk, which then reacts very quickly to create $H_3{}^+$ and then other species, such as the ions mentioned above. The $H_3{}^+$ dissociative recombination branching ratios (McCall et al., 2004) and reaction rates (McCall et al., 2005) used in our network were obtained through ion storage ring experiments at low temperatures and are relatively robust.

Another comparison can be seen in Figure 3.3, which plots the percent change in the column density of a variety of species at R = 250 AU and $L_x = 10^{31}$ ergs s^{-1}. The $\epsilon = 1$ panel is included as a confirmation that the abundances do not change at all when there is no dust settling included, as the X-ray opacity in the compared models should be the same in that case. For the other panels, it is not surprising that the species most strongly affected are those that connect strongly to $H_3{}^+$. In addition, the UV photolysis induced by the X-rays acts to desorb some of the water frozen out onto the grain surfaces, thereby slightly increasing the column of water that we observe. In general, however, the changes in column density due to dust-dependent X-ray opacities are fairly minimal, rarely being more than a factor of 2.

Figure 3.4 shows the charge carriers at each height in the disk at R = 10 AU for $\epsilon = 1$ (top left), $\epsilon = 0.1$ (top right), $\epsilon = 0.01$ (bottom left) and $\epsilon = 0.001$ (bottom right). Each bar represents 100% of the ionized abundance in that zone, with the bars colored depending on how much of that ionization fraction consists of H^+, C^+, HCO^+, $H_3{}^+$ or H_3O^+. All other ionized species are represented by the gray portion of the bar.

For all of the dust settling parameters, the upper layers of the disk consist primarily of C^+ with a little bit of H^+ in the very uppermost zones. The UV radiation dissociates CO, which is then ionized to form C^+. Below the C^+ layer is the molecular layer, where the H_3O^+ forms, with the specific location of the region being dependent on the penetration depth of the X-ray radiation. As X-rays penetrate deeper into the disk, they ionize H_2 to form $H_2{}^+$, which then quickly reacts with H_2 to form $H_3{}^+$ and then with CO to form HCO^+. In the more settled disks, the temperature in this region is above 100 K, so H_2O is able to thermally desorb from dust grains and react with the HCO^+ to form H_3O^+. Finally, in the midplane, temperatures at this radii are above the 17 K needed for CO to freeze-out, so the carbon is all in the form of gas-phase CO. CO therefore is able to react with $H_3{}^+$ created by cosmic rays and X-rays to form HCO^+. These plots indicate the importance of including dust-dependent X-ray opacities, as the differences between the plots are largely due to the effects of dust depletion on the X-ray opacities.

The same plots, but calculated at R = 100 AU, are shown in Figure 3.5. The pattern here is similar to that at 10 AU. The upper layers of the disk consist primarily of C^+ with a molecular region immediately below. Unlike the plots at 10 AU, however, at 100 AU the disk is too cold for H_2O to desorb off of dust grains and form H_3O^+, leading instead to a molecular region that consists of nitrogen-bearing species in the case of $\epsilon = 1$ and HCO^+ in all other cases. At the midplane, the disk is now cold enough for CO to freeze-out onto dust grains, so $H_3{}^+$ is unable to react with CO to form HCO^+ and instead the charge carriers are made up predominantly of $H_3{}^+$ molecules.

3.3.2 Ionization Fraction - General Structure

There are two issues to consider when calculating the location of the active region in the disk. Both the coupling of the gas with the magnetic field, which requires a sufficiently high magnetic Reynolds number, and the ion-neutral collision rate, which requires sufficiently high ambipolar diffusion, are necessary to achieve an active zone in the disk. Both of these values were calculated based on the equations in Perez-Becker & Chiang (2011):

$$Re_M = \frac{c_s h}{D} \approx \left(\frac{x_e}{10^{-13}}\right)\left(\frac{T}{100K}\right)^{0.5}\left(\frac{a}{AU}\right)^{1.5} \tag{3.3}$$

$$Am = \frac{x_i n_{H_2} \beta_{in}}{\Omega} \approx \left(\frac{x_i}{10^{-8}}\right)\left(\frac{n_{H_2}}{10^{10} cm^{-3}}\right)\left(\frac{a}{AU}\right)^{1.5} \tag{3.4}$$

where c_s is the gas sound speed, $h = c_s/\Omega$ is the scale height, Ω is the Kepler orbital frequency, $D = 234(T/K)^{1/2} x_e^{-1}$ is the magnetic diffusivity, x_e is the electron density relative to hydrogen, T is the temperature of the gas and a is the radial distance from the central star. In the equation for A_m, x_i is the abundance of ions relative to hydrogen, n_{H_2} is the number density of hydrogen and $\beta_{in} \approx 1.9 \times 10^{-9} cm^3 s^{-1}$ is the collisional rate coefficient for ions colliding with neutrals (Draine et al., 1983). While it is fairly well established that an Re_M value of ~ 100 is needed for an active layer (e.g., Fleming et al., 2000), the required value of Am is much less well defined. For this chapter we use an Am value of 0.1 to define the active disk (Bai & Stone, 2011).

The results from our model can be seen in Figure 3.6. The colored background shows the electron abundance relative to hydrogen at a time of 10^6 years and $\epsilon = 1$. The lines indicate the $Re_M = 100$ surfaces for different dust settling values. Looking only at the $\epsilon = 1$ case, the dead zone of the disk extends to a radius of almost 40 AU and matches well with the structure seen in previous studies (e.g., Semenov et al., 2004). The same plot, but for Am instead of Re_M, can be seen in Figure 3.7. Again, focusing on the $\epsilon = 1$ case we see a very similar dead zone in the midplane of the disk to that calculated from the Re_M values. The finger structure that exists in the

dead zone is due to the interplay between the ionization fraction and density in those regions of the disk. The major difference between the dead zones calculated using A_m and Re_M is that the uppermost zones of the disk are also 'dead' when calculated with A_m, due to the low densities in those regions.

There are three main sources of ionizing radiation included in our model - UV photoionization, cosmic ray ionization and X-Ray ionization. UV radiation is the dominant mechanism in the upper layers of the disk, but the penetration depth is strongly dependent on dust settling. Below the upper layers, most of the UV radiation is shielded, which means that other sources of radiation are needed in order to achieve an electron abundance high enough for an active disk. To demonstrate this we plot the Re_M values for a disk with X-ray ionization and cosmic ray ionization both turned off in Figure 3.8. Without those sources of ionization, the entire disk below the upper layers has a low enough ion abundance to be considered dead. Figure 3.9 shows the effects of adding cosmic rays back into the model, but continuing to leave out the X-rays in an unsettled disk. There are only slight differences between this plot and the one shown in Figure 3.6, indicating that for our models the cosmic rays dominate the ionizing radiation once the UV field is fully shielded.

3.3.3 Ionization Fraction - Dust Settling

Dust settling will have significant effects on both the UV photoionization and the X-ray ionization rates, which in turn will affect the location and size of the dead zone. The consequence of these effects can be seen in Figure 3.6. The lines in this plot indicate the $Re_M = 100$ surfaces for $\epsilon = 1$ (solid line), $\epsilon = 0.1$ (dashed line), $\epsilon = 0.01$ (dot-dashed line) and $\epsilon = 0.001$ (dotted line). As the dust settling increases, the dead zone shrinks and shifts towards smaller radii as a result of the increased radiation penetration leading to more ionization. Figure 3.7 shows the effect of dust settling on the $A_m = 0.1$ surface. Again, the more settled disks have smaller dead zones that are shifted inwards.

This effect can also be seen in Figures 3.4 and 3.5, where we show the main ionization carriers for different values of the settling parameter ϵ. While the cosmic ray

ionization rate stays largely constant throughout the disk, the UV and X-ray radiation both penetrate further in the settled cases. These plots also show the ionization fraction of each region of the disk in white diamonds overlaid on the histograms. There is a clear trend towards higher ionization fractions for regions near the midplane in settled disks due to increased radiation penetration to those layers.

3.4 Discussion

Previous MHD simulations have looked primarily at the magnetic Reynolds number (Re_M) to determine whether a region in the disk could be considered active. Recent work has suggested that the ion-neutral collision rate (A_m) must also be considered when determining if the magnetic field is able to couple well to the primarily neutral gas of the disk (Perez-Becker & Chiang, 2011). If either of these values are too low, turbulence cannot be sustained and the disk returns to a non-turbulent state. The exact critical values depend on the specific magnetic fields and are under discussion, but some simulations find that turbulence can be sustained when $Re_M \geq 100$ (Fleming et al., 2000) and $A_m \geq 1$ (Turner et al., 2010). However there are large uncertainties on the latter value with some work requiring an A_m of two orders of magnitude higher (Hawley & Stone, 1998) and some indicating that might even be as low as 0.1 (Bai & Stone, 2011).

For this chapter we looked at how the active zone of the disk looked when calculated from both Re_M and A_m values as well as what effects dust settling would have on the active zone location and size. The magnetic Reynolds number Re_M, is calculated using Equation 3.3. Figure 3.10 shows the Re_M value vs. column density at radii of 5 and 10 AU for each of the four dust settling parameters, $\epsilon = 1$, 0.1, 0.01, 0.001. In all cases the upper regions of the disk are well above the critical value needed for good coupling of the ions with the magnetic field, with the Re_M in those regions mostly dependent on the column density of the disk, since the entire disk in that region is ionized. In the inner regions of the disk, the more settled the disk the larger the active region. As settling increases, UV and X-ray radiation are able to penetrate deeper, leading to greater ionization fractions near the midplane and

better coupling with the magnetic field. There is no significant difference between the results at 5 and 10 AU from the central star.

The second method used to determine if a disk is active is the ion-neutral collisional frequency A_m, calculated using Equation 3.4. Figure 3.11 shows the A_m value vs. column density at radii of 5 and 10 AU for each of the four dust settling parameters. Unlike the case with Re_M, the upper regions of the disk have a low enough density that these regions are not considered active. Instead, there is a narrow region in the middle of the disk where the disk is clearly active and then the region near the midplane is very close to our chosen critical value. Dust settling does not play a large role in the shape of the curves, other than in the specific details of exactly where near the midplane the disk would be considered active. Since this is sensitive to the choice of critical A_m value, we do not feel that this region is significant.

Looking at both methods of calculating the active region of the disk, the combined active region is almost identical to the active region calculated from the A_m value alone. This is because the active region determined from the Reynolds number covers a larger region of the disk than that from the ion-neutral collisional frequency. The exception to this is the situation in settled disks, where the A_m value sometimes produces a small active region near the midplane. However, the presence of this active region is extremely sensitive to the value of A_m; with even slightly higher critical values of A_m removing the presence of an active zone deep in the disk. In both cases, beyond a few tens of AU the disk can be considered completely active, in agreement with observations (Andrews et al., 2009).

3.4.1 Mass of Active Region

More interesting than just the location of the active zone, at least in terms of angular momentum transport, is how much mass is present in the active regions of the disk. The mass column for the active regions of the disk for models with $L_x = 10^{31}$ ergs s^{-1} and $\epsilon = 1$, $\epsilon = 0.1$, $\epsilon = 0.01$ and $\epsilon = 0.001$ are shown in Figure 3.12 for Re_M and Figure 3.13 for A_m. At radii larger than R $\sim$ 40 AU the disk is completely active, so the plots trace the total mass column at those radii. The spikes at small radii are

a numerical artifact due to the grid selected for the models. The steep rise shows the transition from a disk that is partially active to one that is fully active. Within the partially active portions of the disk, the mass column is roughly constant, but as soon as a region has enough mass the UV and X-rays are shielded and the disk will likely become dead due to the lack of ionizing radiation.

From the mass column we are able to estimate the mass accretion rate expected due to the MRI from this active region (Z. Zhu, private communication). Rearranging equation 2.1 we are able to estimate the mass accretion rate, $\dot{M}$, as:

$$\dot{M} = 3\pi\nu\Sigma \tag{3.5}$$

$$\nu = \alpha H c_s \tag{3.6}$$

$$H = \frac{c_s}{\Omega} \tag{3.7}$$

$$c_s = \sqrt{\frac{k_B T}{\mu m_H}} \tag{3.8}$$

$$\Omega = \sqrt{\frac{G M_*}{R^3}} \tag{3.9}$$

where ν is the viscosity, Σ is the mass column of the active region, α is the disk parameter, H is the scale height, c_s is the sound speed and Ω is the rotational frequency. In the equations for c_s and Ω, k_B is the Boltzmann constant, T is the temperature, μ is the mean molecular weight, m_H is the mass of a hydrogen atom, G is the gravitational constant, M_* is the mass of the central star and R is the disk radius. In order to match the observed mass accretion rates of $\sim 10^{-8}$ $M_\odot$ yr^{-1} we need a mass column of ~ 10 g cm^{-2} at a radius of 10 AU (e.g., Sano et al., 2000; Igea & Glassgold, 1999). Looking at the mass column densities determined from ambipolar diffusion, Figure 3.13, we calculate a mass accretion rate of $\sim 10^{-11}$ $M_\odot$ yr^{-1} for a disk with no dust settling, in agreement with the results found by Perez-Becker & Chiang (2011). For a disk with $\epsilon = 0.1$ our model still produces too small an active zone, but for the disks with $\epsilon = 0.01$ and $\epsilon = 0.001$ our model has enough mass in the active regions to achieve $\sim 10^{-8}$ $M_\odot$ yr^{-1}.

For the Reynolds number calculation, Figure 3.12, we see a similar effect with the calculated accretion rate being too low to match observed accretion rates in the unsettled disk. In the settled disk cases, by comparison, the mass column density is large enough at R $\sim$ 10 AU for us to achieve $\dot{M} \approx 10^{-8} M_{\odot}$ yr^{-1} in all three cases. Both this plot and the one for A_m indicate the importance of dust settling for these dead zone calculations. In an unsettled disk, in both cases the active region is too small to support the mass accretion rates that we observe. In comparison, once dust settling is included in the models the active zones quickly become massive enough to permit the observed values.

We should note that while we have enough mass in the active regions at 10 AU to match the observed accretion rates, the mass in the active region must increase as the radius decreases, as 1/R, in order for the star to be accreting at the observed rate (Gammie, 1996). Our model does not produce this larger active zone mass at smaller radii. This is partially due to the lack of thermal ionization processes in our network, which will become increasingly more important at smaller radii as the temperature increases.

3.4.2 Cosmic Rays

Based on the properties inferred from disk observations we have found that the MRI appears capable of powering accretion in these systems, which differs from what has been found in previous studies. Our models are active because they are permissive to cosmic ray radiation, meaning that cosmic rays are able to penetrate all regions of the disk, as seen in Figure 3.14 which plots the ionization rates for a model with $\epsilon = 0.001$ at a radius of 5 AU.

The dead zones calculated from a model in which X-ray ionization was removed from the calculations, Figure 3.9, looks almost identical to the dead zones calculated with X-ray ionization included, Figure 3.6. This is due to the fact that our disks are so permissive to cosmic rays that cosmic ray ionization is the dominant ionization mechanism near the midplane. The penetration depth of cosmic rays is 96 g cm^{-2} (Umebayashi & Nakano, 1981), but the total mass column at R = 5 AU in our

unsettled disk is half that value (D'Alessio et al., 2006, Figure 6). As a result, cosmic rays are able to permeate the entire disk and dominate the ionization radiation in the lower layers. The disks calculated in D'Alessio et al. (2006) reproduce the observed disk spectral energy distributions (SEDs). In a settled disk the temperature increases, which leads to a lower disk mass needed to match the observed SED and therefore greater cosmic ray penetration.

There are some potential issues with our model. The dust emissivity is not well determined and may suggest significantly larger disk masses from the SED observations (Hartmann, 2008). For example, the mass column in our model is lower at small radii than that in the Minimum Mass Solar Nebula (MMSN; Hayashi, 1981), which has a mass column at 5 AU of ~ 150 g cm^{-2}. A larger disk mass in these inner regions would prevent the cosmic rays from penetrating as deeply.

In our own solar system the solar wind deflects lower energy, < 100 MeV, Galactic cosmic rays away from the ecliptic plane, thereby protecting planetary atmospheres from the ionizing effects of cosmic rays. Assuming that T Tauri stars have magnetocentrifugal winds similar to the solar wind, this would similarly protect the inner regions of the disk from cosmic ray ionization (Glassgold et al., 1997). In order to mimic the effects of such a wind, we removed cosmic rays inside of 85 AU, roughly the distance of the heliopause in our solar system (e.g., Burlaga et al., 2008; Decker et al., 2008). The results of this can be seen in Figure 3.15, with a large dead zone throughout the disk until a radius of 85 AU, at which point the disk has a sharp transition to being active for all ϵ values.

The calculated active zone masses for this model can be seen in Figures 3.16 from the Re_M value and 3.17 from the A_m value. Based on the Reynolds number, the maximum active zone disk mass is ~ 3 g cm^{-2} at R = 10 AU for the most settled disk. This is slightly below the 10 g cm^{-2} needed to produce a mass accretion rate of 10^{-8} M$_\odot$ yr^{-1}, though it is almost an order of magnitude higher than the 0.4 g cm^{-2} achieved in the unsettled disk. The calculations for A_m are even more problematic, with the maximum mass column reaching just 1 g cm^{-2} for the $\epsilon = 0.001$ disk.

3.4.3 Conclusions

In conclusion, we present the results of a full chemical network with dust settling dependent X-ray opacity and discuss the implications on ambipolar diffusion and the magnetic Reynolds number when UV radiation and dust settling included. In particular, our conclusions are as follows:

1. Dust settling increases the mass column of the active region by almost an order of magnitude.

2. The mass accretion rates are fairly low, 10^{-11} $M_\odot$ yr^{-1}, when calculated from ambipolar diffusion in the unsettled disk, but match with those determined by Perez-Becker & Chiang (2011). However, the location of the active region in the disk is highly dependent on dust settling and, in turn, so are the mass accretion rates calculated. In a settled disk, the accretion rates calculated from A_m, as well as Re_M, match observations of 10^{-8} $M_\odot$ yr^{-1}.

3. Our adopted disk models have low surface densities at the inner radii, below that of the MMSN, which causes cosmic ray ionization penetrating through to the midplane. Removing cosmic ray ionization leads to active zone mass columns below what is needed to produce the observed accretion rates.

4. The main ionized species in the disk vary when dust settling is included, but in general have the same structure in every disk. The upper regions of the disk consist primarily of C^+ due to UV photoionization, with the charge carriers in the molecular layer below that being made of H_3O^+ or HCO^+ depending on whether the temperature is high enough for H_2O to thermally desorb. The size of this layer is dependent on dust settling due both to the temperature needed for desorption of H_2O and to how deep into the disk the X-rays are able to penetrate. Finally, in the midplane the cosmic rays produce $H_3{}^+$ which reacts with CO in the gas phase to form HCO^+.

5. Including dust-dependent X-ray opacity has only minor effects on the calculated molecular column densities of species in the disk. Column densities vary by only

a factor of 2 in even the largest cases.

6. The active zone when calculated from the ambipolar diffusion value is strongly dependent on the critical value of A_m used. A slightly different value can lead to a larger or smaller active region, so the uncertainties in this value are important for accurately determining the active zone of the disk.

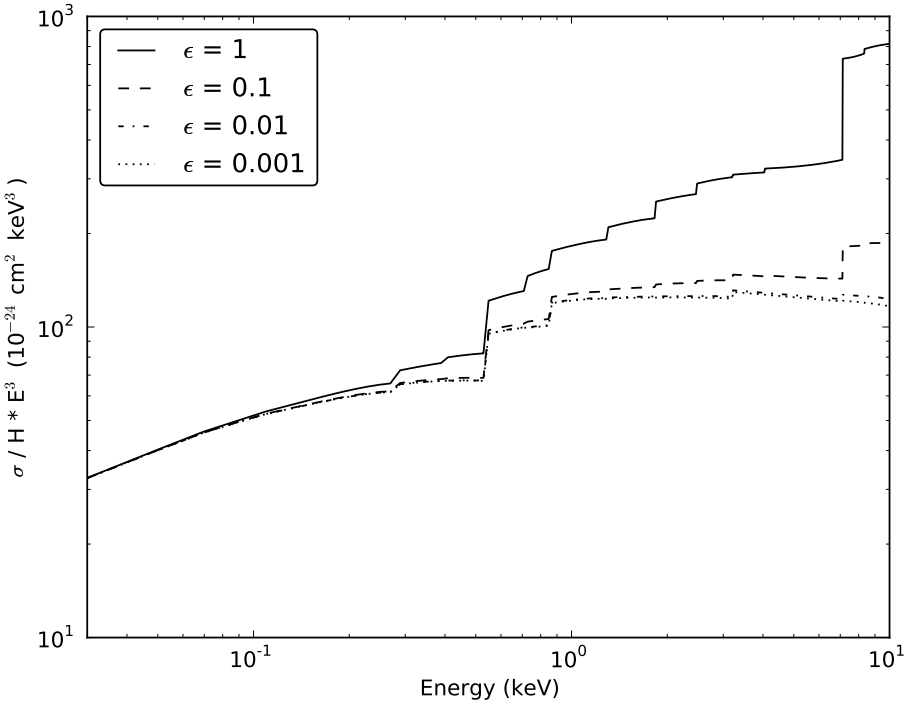

Figure 3.1. The contribution to the X-ray opacity by grains as a function of the dust settling parameter, ϵ. Originally from Bethell & Bergin (2011).

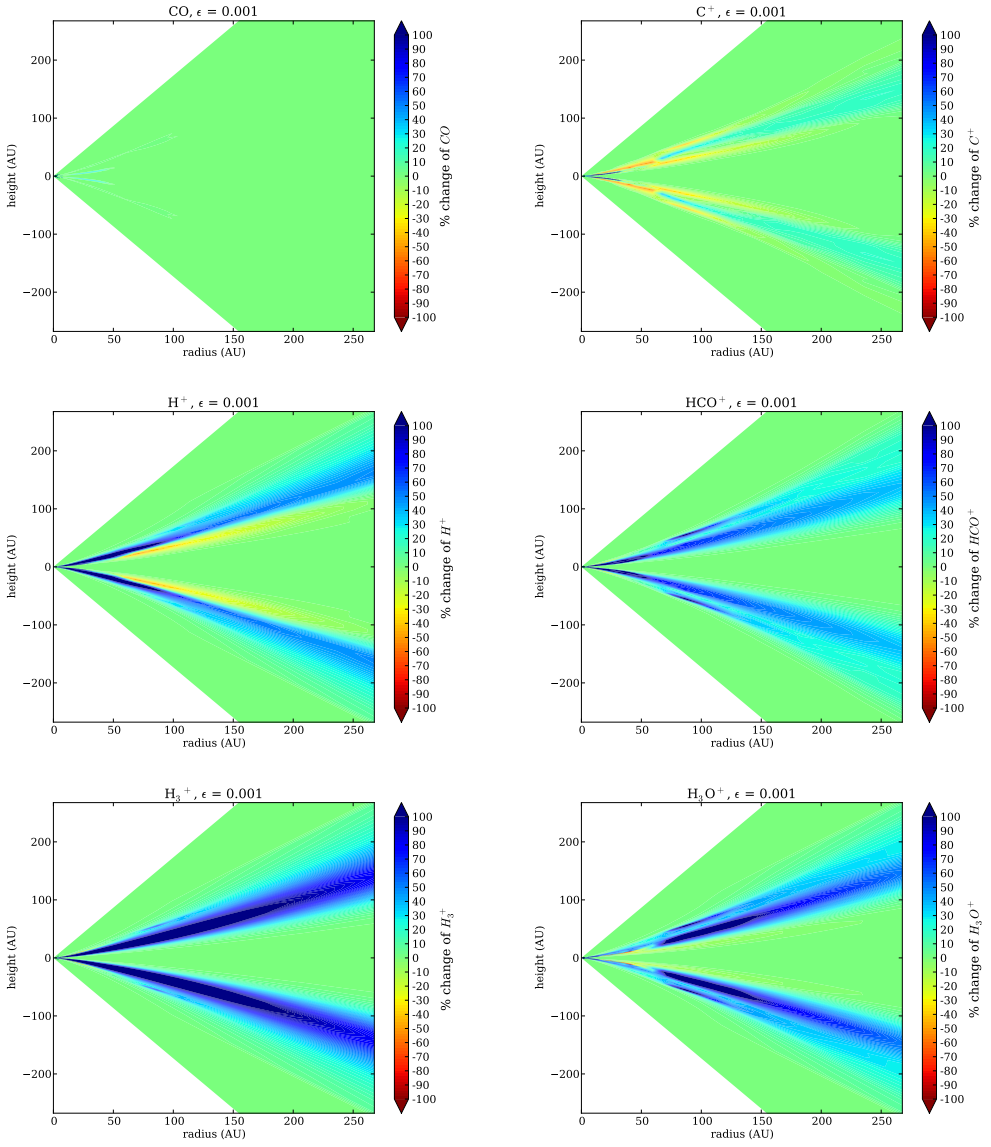

Figure 3.2. Percent change in abundance when including dust-dependent X-ray opacity in a disk with $\epsilon = 0.001$ and $L_x = 10^{31}$ ergs s^{-1} for CO (top left), C^+ (top right), H^+ (middle left), HCO^+ (middle right), $H_3{}^+$ (bottom left) and H_3O^+ (bottom right).

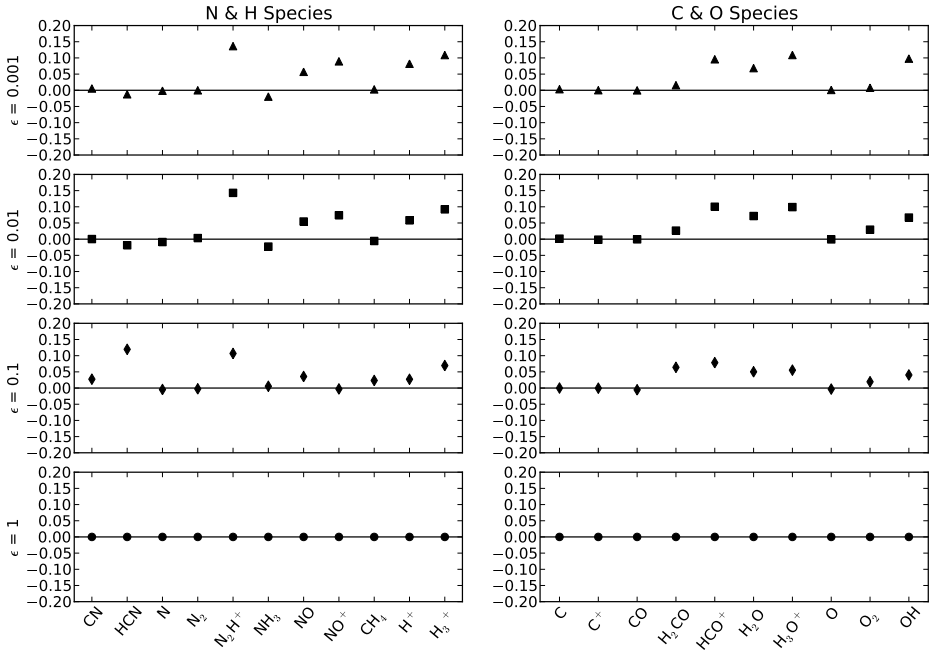

Figure 3.3. Percent change in column density for models with $L_x = 10^{31}$ ergs s^{-1} and different dust settling parameters, computed at R = 250 AU.

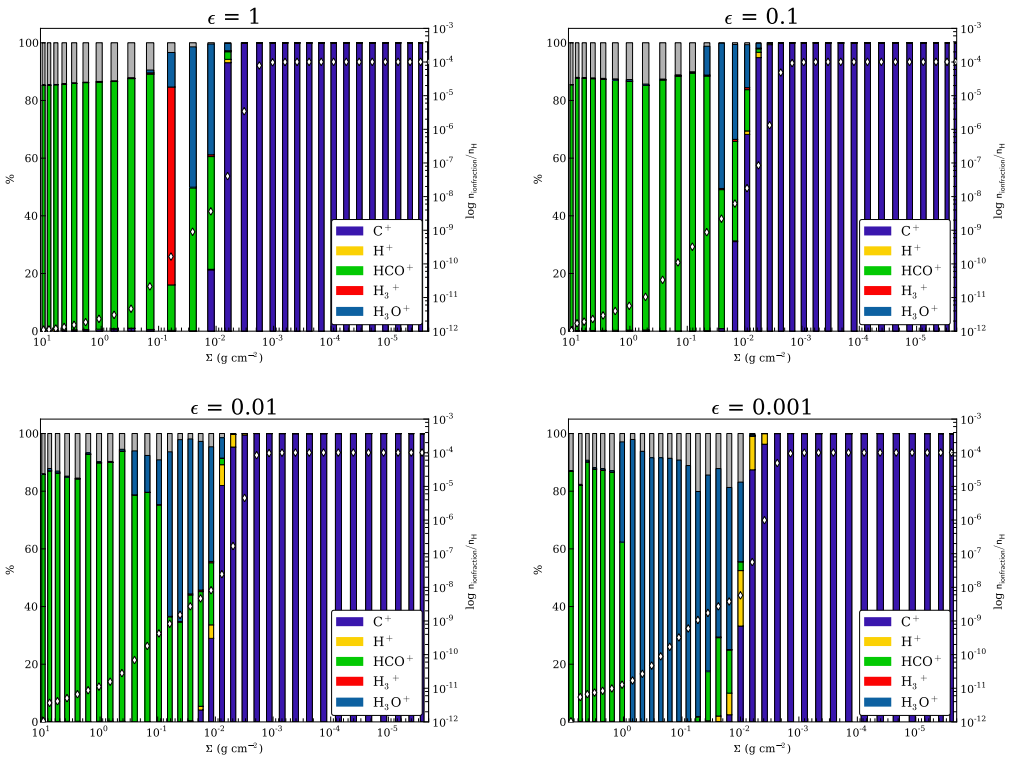

Figure 3.4. Stacked histograms of ionization fraction constituents for a disk at R = 10 AU and $L_x = 10^{31}$ ergs s^{-1} for $\epsilon = 1$ (top left), $\epsilon = 0.1$ (top right), $\epsilon = 0.01$ (bottom left) and $\epsilon = 0.001$ (bottom right). White points indicate the total ionization fraction of the disk at that point.

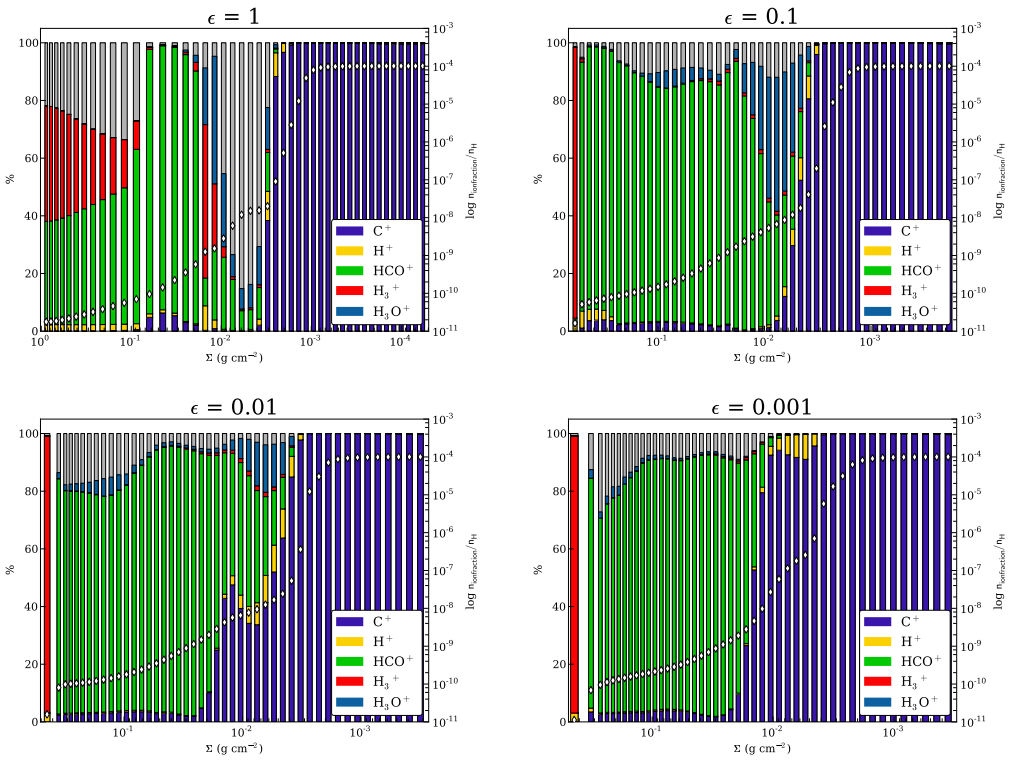

Figure 3.5. Stacked histograms of ionization fraction constituents for a disk at R = 100 AU and $L_x = 10^{31}$ ergs s^{-1} for $\epsilon = 1$ (top left), $\epsilon = 0.1$ (top right), $\epsilon = 0.01$ (bottom left) and $\epsilon = 0.001$ (bottom right). White points indicate the total ionization fraction of the disk at that point.

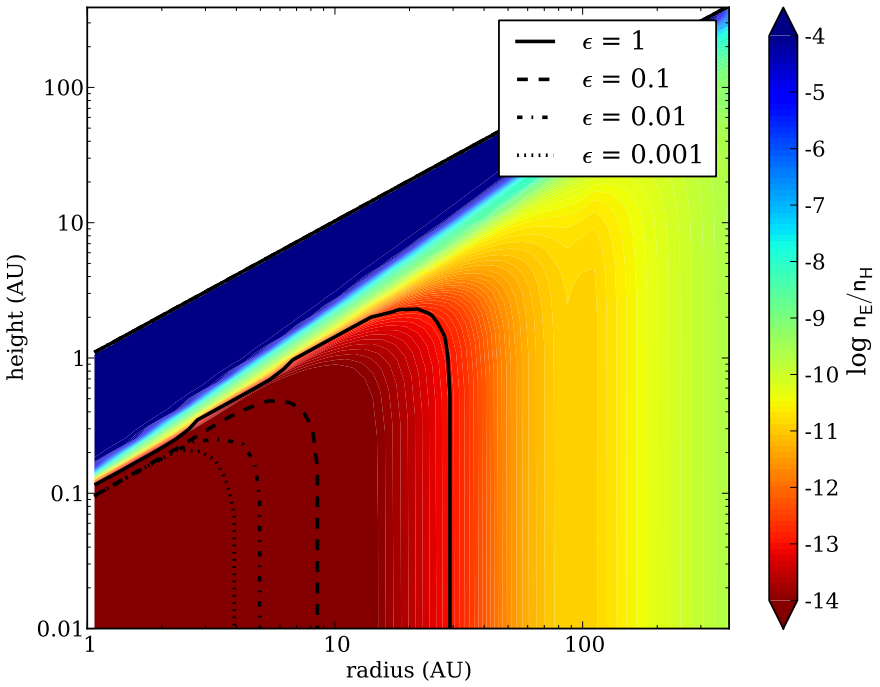

Figure 3.6. Colored surface plot of the electron density for a disk with $\epsilon = 1$ and $L_x = 10^{31}$ ergs s^{-1}. Lines plotted indicate the $Re_M = 100$ surfaces for $\epsilon = 1$ (solid), $\epsilon = 0.1$ (dashed), $\epsilon = 0.01$ (dash-dotted) and $\epsilon = 0.001$ (dotted).

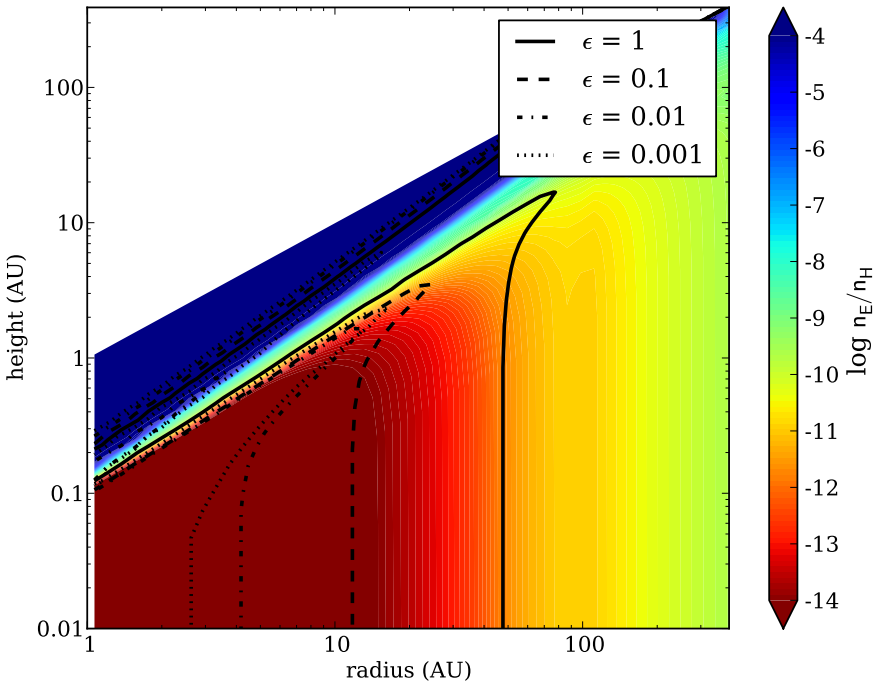

Figure 3.7. Colored surface plot of the electron density for a disk with $\epsilon = 1$ and $L_x = 10^{31}$ ergs s^{-1}. Lines plotted indicate the $A_m = 0.1$ surfaces for $\epsilon = 1$ (solid), $\epsilon = 0.1$ (dashed), $\epsilon = 0.01$ (dash-dotted) and $\epsilon = 0.001$ (dotted).

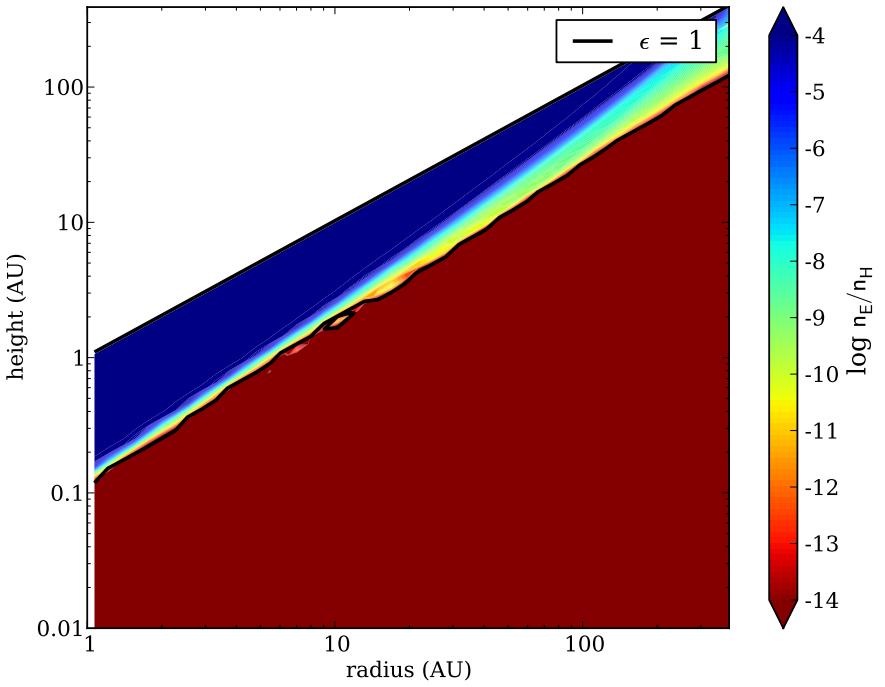

Figure 3.8. Colored surface plot of the electron density for a disk with $\epsilon = 1$ and $L_x = 10^{31}$ ergs s^{-1} with no X-ray or cosmic ray ionization included. Solid line indicates the $Re_M = 100$ surface.

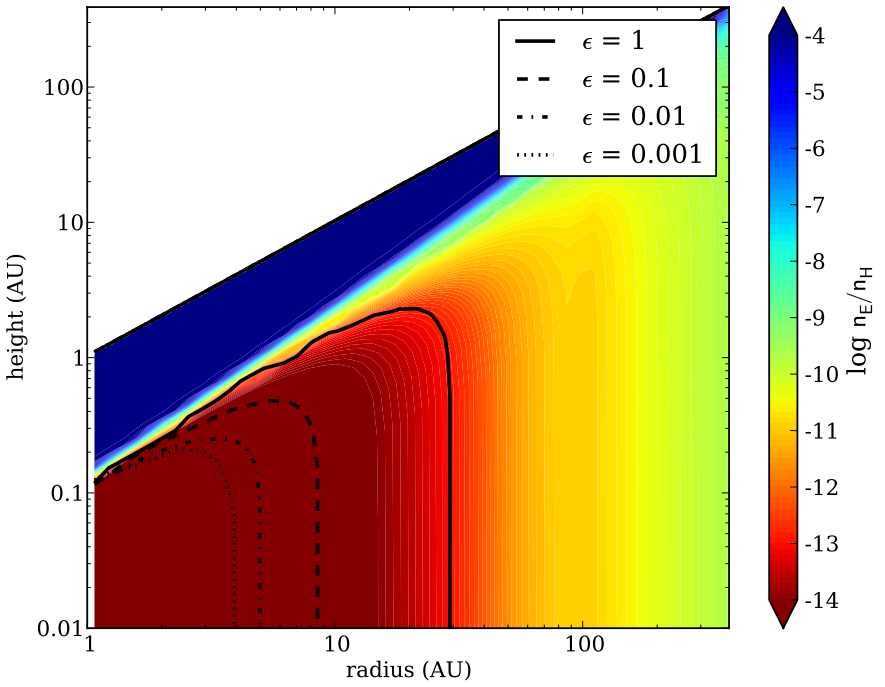

Figure 3.9. Colored surface plot of the electron density for a disk with $\epsilon = 1$ and $L_x = 10^{31}$ ergs s^{-1} with no X-ray ionization included. Solid line indicates the $Re_M = 100$ surface.

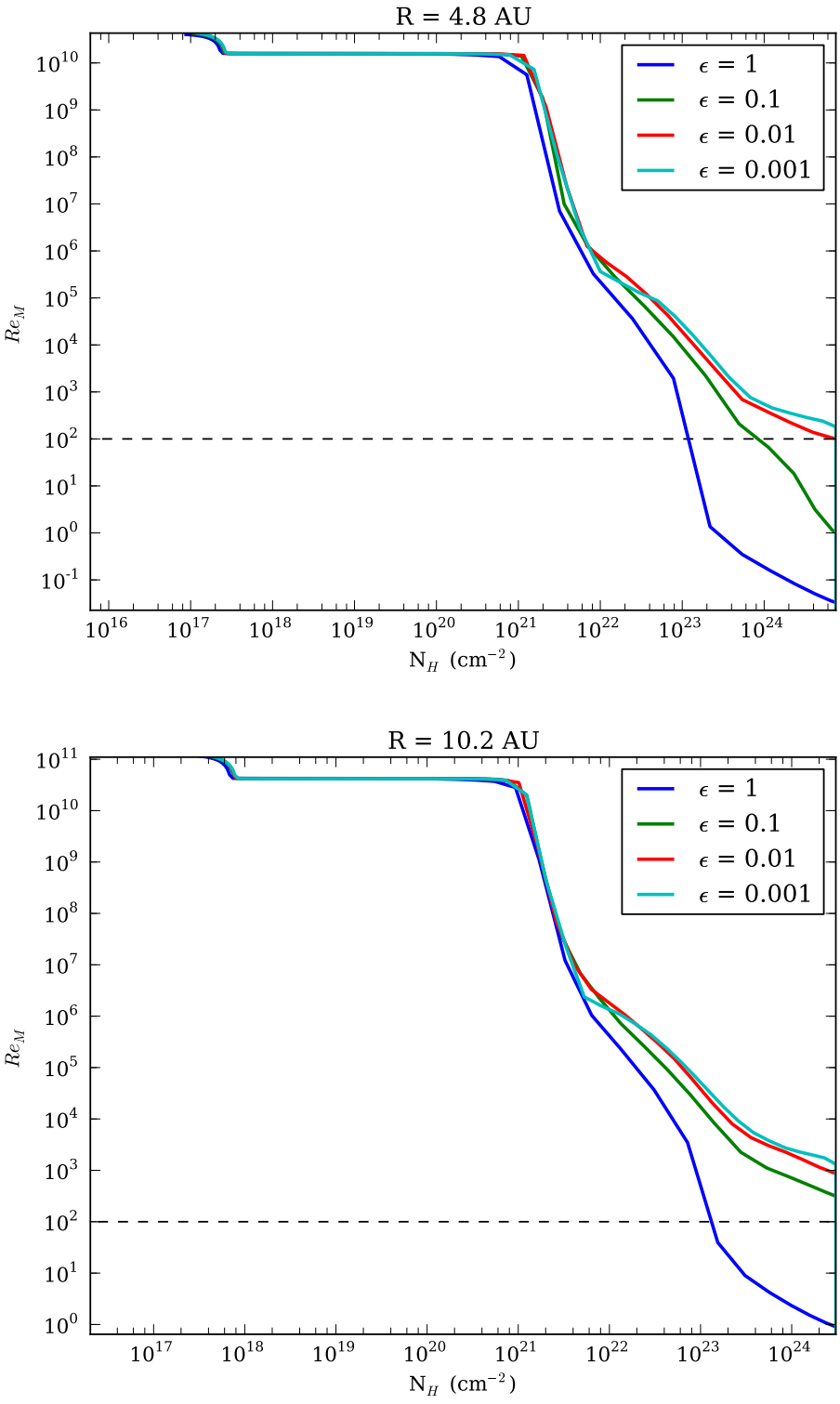

Figure 3.10. Plot of magnetic Reynolds number (Re_M) vs. column density for different dust settling parameters at R $\sim$ 5 and 10 AU.

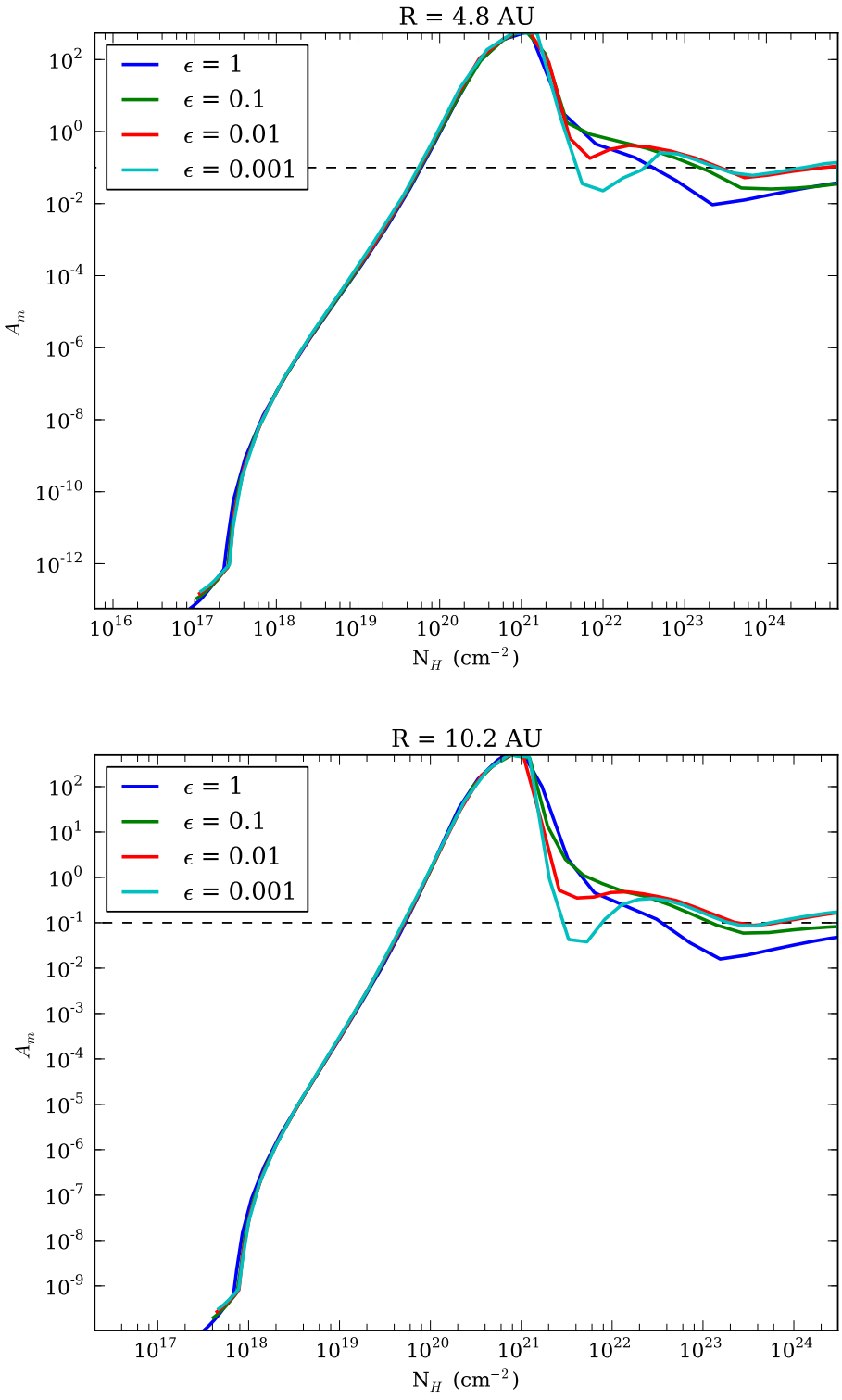

Figure 3.11. Plot of ambipolar diffusion value (A_m) vs. column density for different dust settling parameters at R $\sim$ 5 and 10 AU.

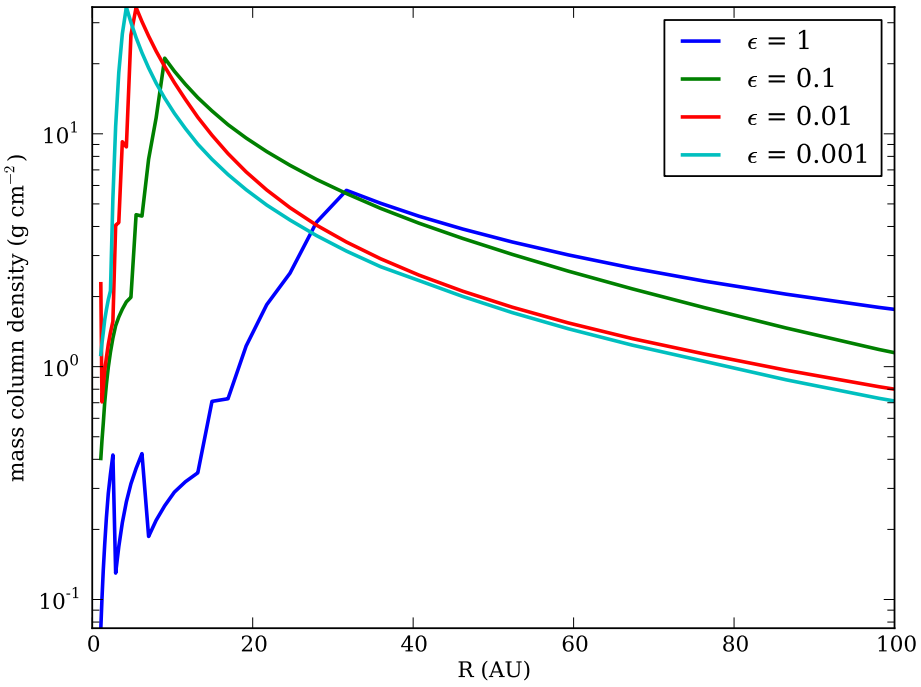

Figure 3.12. Plot of the mass column of the active region of the disk vs. radius, calculated from the Re_M value, for different dust settling parameters.

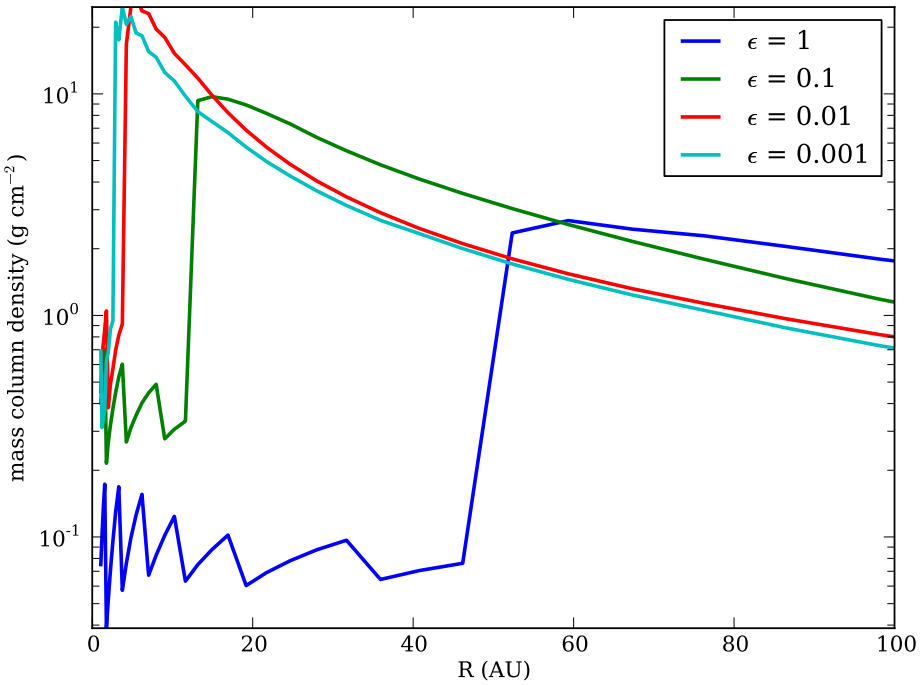

Figure 3.13. Plot of the mass column of the active region of the disk vs. radius, calculated from the A_m value, for different dust settling parameters.

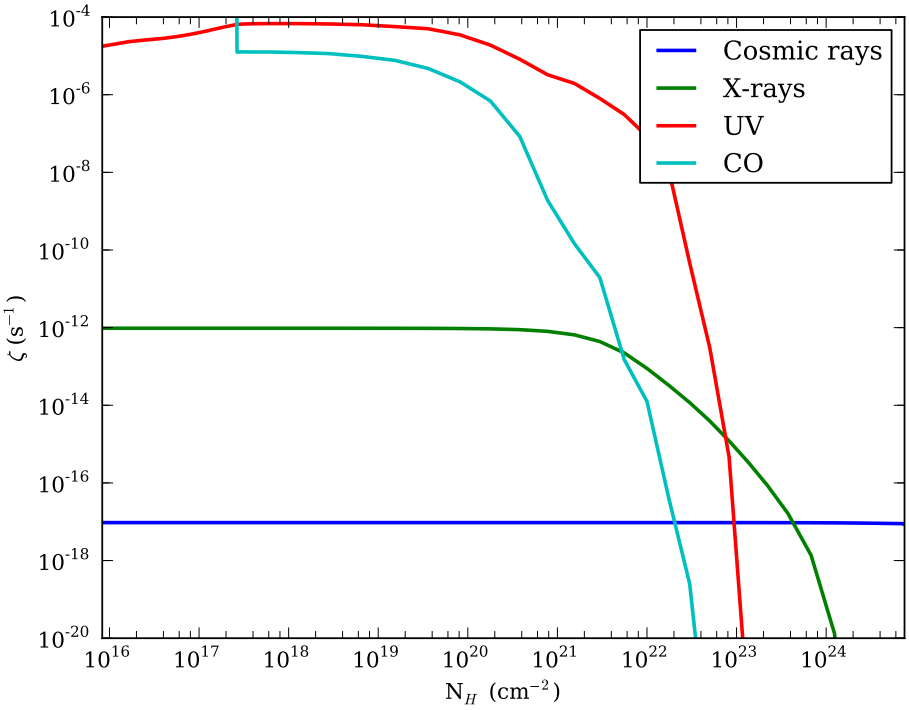

Figure 3.14. Ionization rates vs column density for a disk at R = 5 AU and $\epsilon = 0.001$ for UV, X-rays and cosmic rays. The CO photodissociation rate included for comparison.

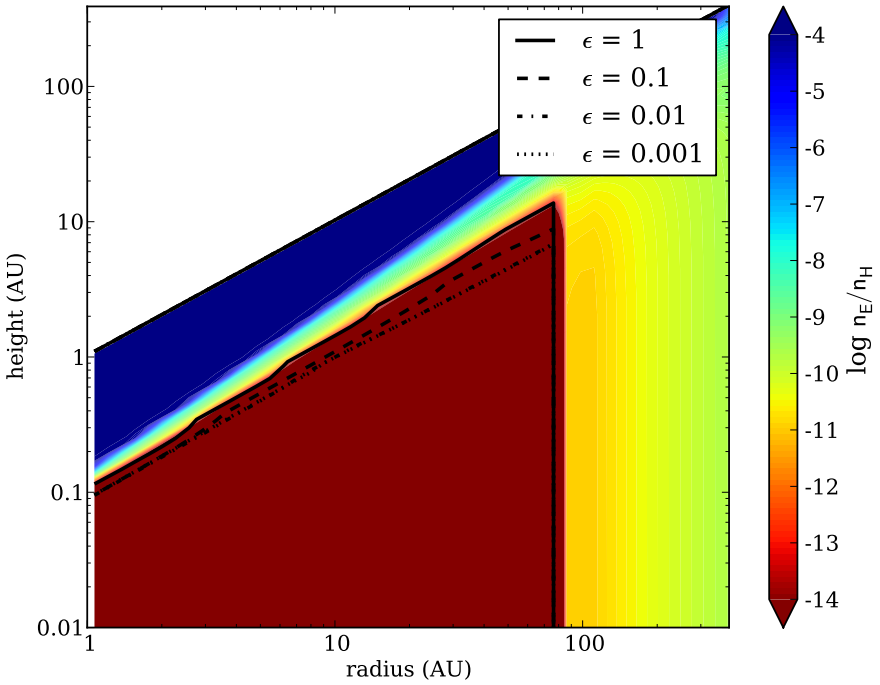

Figure 3.15. Colored surface plot of the electron density for a disk with $\epsilon = 1$ and $L_x = 10^{31}$ ergs s^{-1} with cosmic ray ionization turned off inside of R = 85 AU to mimic the heliopause. Lines plotted indicate the $Re_M = 100$ surfaces for $\epsilon = 1$ (solid), $\epsilon = 0.1$ (dashed), $\epsilon = 0.01$ (dash-dotted) and $\epsilon = 0.001$ (dotted).

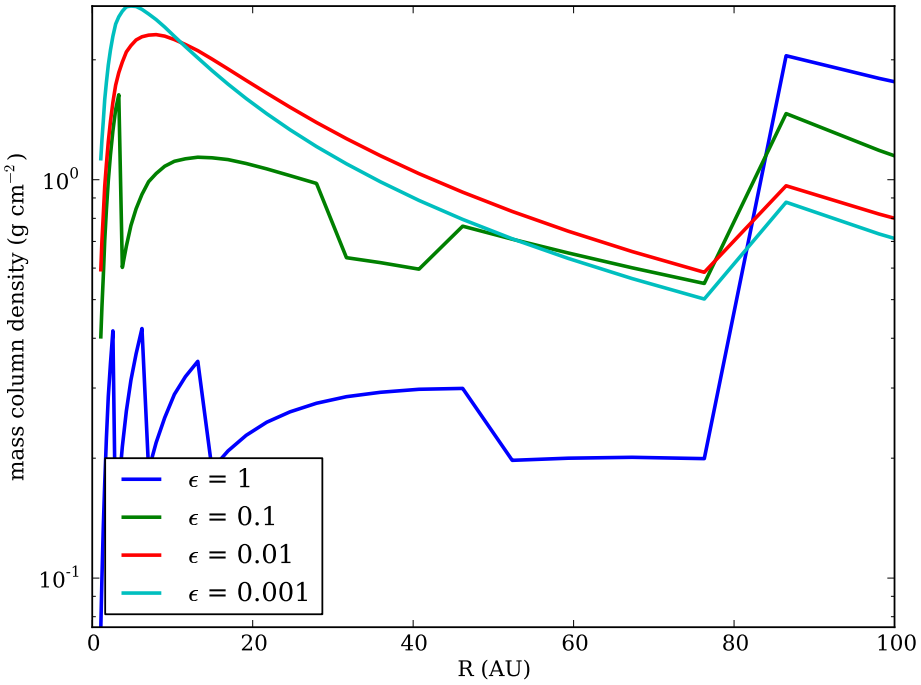

Figure 3.16. Plot of the mass column of the active region of the disk vs. radius, calculated from the Re_M value, for different dust settling parameters with cosmic ray ionization turned off inside of R = 85 AU to mimic the heliopause.

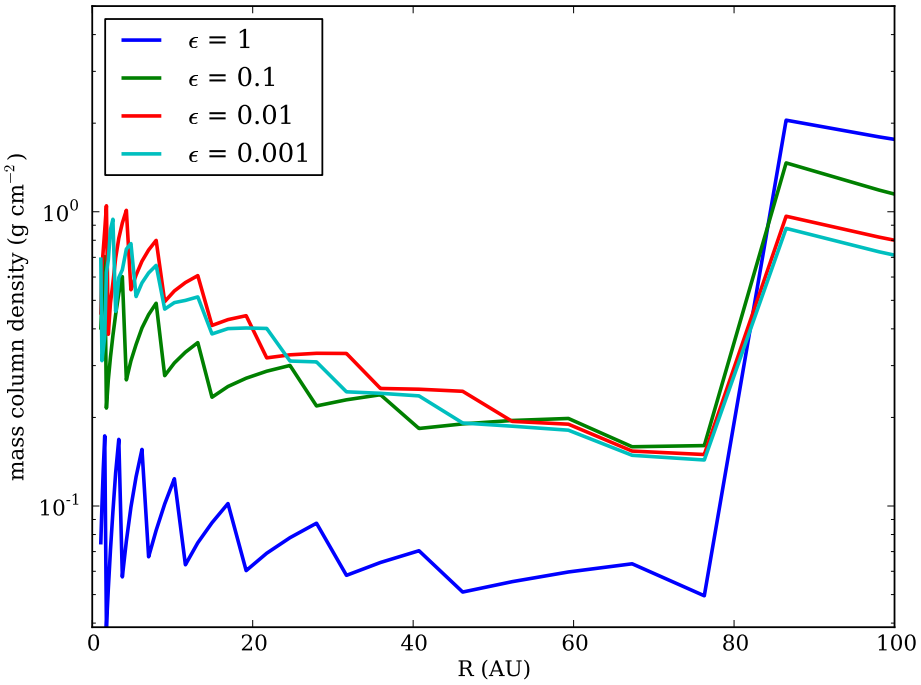

Figure 3.17. Plot of the mass column of the active region of the disk vs. radius, calculated from the A_m value, for different dust settling parameters with cosmic ray ionization turned off inside of R = 85 AU to mimic the heliopause.

Table 3.1. Disk Ionization Processes and Vertical Structure[a]

Layer/Carrier	Ionization Mechanism	$\Sigma_{\tau=1}$ (g cm^{-2})[b]
Upper Surface	UV photoionization of H[c]	6.9×10^{-4}
Lower Surface	UV photoionization of C[d]	1.3×10^{-3}
Warm Mol.	Cosmic [e] and X-ray[f] Ionization	96 (CR)
		0.05 (1 keV)
		2.1 (10 keV)
Midplane	Cosmic ray[e] Ionization and Radionuclides[g]	

[a] Based on the Table in Bergin et al. (2007).
[b] Effective penetration depth of radiation (e.g., $\tau = 1$ surface).
[c] Estimated at 100 AU assuming 10^{41} s^{-1} ionizing photons (Hollenbach et al., 2000) and $\sigma = 6.3 \times 10^{-18}$ cm^2 (H photoionization cross-section at threshold). This is an overestimate as we assume all ionizing photons are at the Lyman limit.
[d] Rate at the disk surface at 100 AU using the radiation field from Bergin et al. (2003).
[e] $\Sigma_{cr} = 96$ g cm^{-2} as given in Umebayashi & Nakano (1981).
[f] Calculated from Bethell & Bergin (2011)

CHAPTER 4

Central Star Spectral Type

4.1 Introduction

There is clear evidence for circumstellar disks around both low and high mass stars, with spectral types ranging from M through A/B stars. Light from the central star is one of the dominant terms in determining the physical structure of the disk (Calvet et al., 1991, 1992; Chiang & Goldreich, 1997). In particular, the higher luminosities of more massive stars will lead to the disks surrounding those stars having higher central midplane temperatures. Thus there is a clear expectation that the central midplane, as well as the upper layers of the disk, will have chemical composition strongly dependent on the central star spectral type.

Observational surveys of chemistry in molecule-rich disks have found, and isolated, some of these differences in a limited number of objects (e.g., Dutrey et al., 1997; Qi, 2001; Dutrey et al., 2007b; Schreyer et al., 2008; Pascucci et al., 2009; Öberg et al., 2010). These observations are hindered by relatively small angular size, $\sim 1''$-$4''$, which requires interferometric millimeter and submillimeter observations to observe the dominant molecules. However even the best resolution of current facilities such as the Submillimeter Array and the IRAM Plateau de Bure Interferometer is only able to resolve disks at tens of AU scales.

One of the first observational studies of chemistry in protoplanetary disks was done by Qi (2001), who systematically observed LkCa 15 (spectral type K3), GM Aur (K5), MWC 480 (A3) and HD 163296 (A1) with the OVRO millimeter array. They found a connection between the central star luminosity and the chemistry in the disks, with higher luminosity stars generally having larger CN/HCN ratios. Dutrey

et al. (2007b) detected N_2H^+ emission around LkCa 15 and DM Tau (M1.5), two low mass stars, but not around MWC 480. Similarly, Schreyer et al. (2008) looked at the disk around AB Aur, a type A0 star, and observed relatively poor molecular content when compared with the disk around DM Tau. Pontoppidan et al. (2010) found that out of 25 Herbig Ae stars, there was not a single detection of HCN, C_2H_2 or OH. This is in comparison with stars of spectral type later than F, for which the detection rate of these molecules was $\sim 40\%$.

The DISCS study (Öberg et al., 2010) observed six disks with a range of spectral types and detected molecules such as N_2H^+ and H_2CO around the T Tauri stars, but not the Herbig stars, in their sample. The common argument for this variation is that the disks around more massive stars are warmer due to the higher luminosities from the central stars. This would lead to an increase in temperature in the disk midplane which would, in turn, lead to species such as CO being desorbed off of the dust grains in the midplane, providing gas-phase CO to react with and destroy the N_2H^+ in the disk. We have constructed disk chemical models to explore whether this hypothesis is correct and to investigate further the implications of a warm CO-rich vs. a cold CO-poor midplane.

There have been many models of protoplanetary disk chemistry around both K type T Tauri stars (e.g., Aikawa et al., 2002; Willacy, 2007; Nomura et al., 2007) as well as Herbig stars (Jonkheid, 2006). However, these studies generally focused on a single spectral type and not on comparisons across types. Pinte et al. (2010) is one of the first studies to compare models across spectral types and has found a correlation between the flux of the [O I] 63 μm line and stellar luminosity.

For this chapter we present the results of a chemical model run for a range of central star spectral types (A6, F1, G0, K7, M5) surrounded by circumstellar disks. We will focus primarily on the chemistry of the midplane, where most of the mass resides, so as to remove any uncertainties in the model. The midplane chemical abundances will be primarily dependent on temperature, which is simpler to understand and explain. Most emission arises from the exposed surface and hence observations do not directly probe the midplane, though the trends there will extend to the up-

per layers of the disk as well. In addition, if the midplane gas is warm enough, the freeze-out zone will disappear and the molecular layer will extend down to include the midplane, producing observational consequences. Thus, by looking at the midplane we can more clearly see how temperature affects the chemistry. In Section 4.2 we describe in detail the model that we are using, in Section 4.3 we present the results of changing the central star spectral type and in Section 4.4 we discuss the observational implications for our results.

4.2 Model

The chemical model used for this work was described in detail in Chapter 2. Here, we discuss some of the important details of the model as well as variations from the canonical model presented in that chapter. The physical structures of the disks used were provided by C. Espaillat (private communication) and are based on the models presented in D'Alessio et al. (2006). Table 4.1 shows the stellar and disk parameters for each of the spectral types looked at in this work. The luminosities of the stars we used ranged from 0.19 $L_\odot$ to 160 $L_\odot$, with a large jump in luminosities occurring between the K7 and G0 type stars. The sharp transition was due to our selecting stellar parameters that match the youngest stars for the G0, F1 and A6 types, thereby increasing the luminosities of those stars. This might potentially lead to more extreme differences between the cooler two spectral types and the hotter three spectral types than would otherwise be anticipated. In all cases the mass accretion rate $\dot{M} = 10^{-8} M_\odot$ yr^{-1} and the viscosity parameter $\alpha = 0.01$.

4.2.1 Density & Temperature

The temperature and density structures of the disks were calculated using the procedures of D'Alessio et al. (2006). We have decided not to include the effect of dust settling in the models presented in this chapter. While dust settling will play a large role in determining the temperature of the upper layers of the disk, it has a less significant effect on the midplane temperature.

The temperature and density structure vs. radius of the midplane of the five disks

used around stars of spectral types A6, F1, G0, K7 and M5 can be seen in Figures 4.1 and 4.2 respectively. While the density structures of the disks are fairly similar across the five spectral types, the temperature structures are demonstrably different. This variation will lead to large changes in the chemistry, as the temperature of the midplane will determine which species are frozen onto dust grains and which are in the gas. These specific spectral types were chosen so as to be able to compare our results with the observational results of the DISCS study (Öberg et al., 2010), which observed a range of spectral types from M1.5 through A3.

4.2.2 Sources of Ionization

As seen in Table 3.1 there are three main ionization sources in the disk. UV photoionization will primarily be important only in the upper layers of the disk, due to the low surface density required to completely shield the disk from UV radiation. Thus the effect of UV radiation, and the UV field shape, is not important in the midplane as the UV field will be completely shielded before it reaches that layer. However, for consistency, the UV fields we included in the model are shown in Figure 4.3. These were created by combining the closest matching Kurucz spectrum, the photosphere of the star, with the observed TW Hya spectra, to account for the UV emission due to the accretion shock (Calvet & Gullbring, 1998). Cosmic rays will penetrate to the midplane at most radii and therefore are a dominant ionization source in that portion of the disk. X-rays are important in the outer regions of the disk, where the surface density of the midplane drops below 2.1 g cm^{-2}, the penetration depth of 10 keV X-rays, but likely not in the inner radii, R $\lesssim$ 40 AU, of the disk midplane.

4.3 Results

For the results presented in this chapter we focus exclusively on the midplane of the disk so as to analyze the effects of the central star spectral type while ignoring the effects of dust settling. All quoted abundances are relative to total hydrogen unless otherwise stated. We focus primarily on molecules that have been observed by surveys such as Öberg et al. (2010).

CO is likely the second most abundant gas-phase molecule in the disk after H_2 and is the primary reservoir of carbon in the disk for all layers except the photoionization region at the top of the disk. In general, carbon will freeze-out onto dust grains as CO(gr) at temperatures below 17 K (Hollenbach et al., 2009), will exist as C or C^+ if the ionizing radiation is strong enough and otherwise will be in the form of gas-phase CO. Figure 4.4 demonstrates that the CO abundance can be explained almost purely by this temperature dependence. The right panel plots the density-weighted midplane abundance along the y-axis vs. the density-weighted midplane temperature along the x-axis, calculated as:

$$T(weighted) = \frac{\sum_i T_i M_i}{\sum_i M_i} \tag{4.1}$$

$$n(weighted) = \frac{\sum_i n_i M_i}{\sum_i M_i} \tag{4.2}$$

$$M_i = \rho_i H_i \pi (R_i^2 - R_{i-1}^2) \tag{4.3}$$

where T_i is the temperature of the i^{th} zone, n_i is the chemical abundance of a given species in the i^{th} zone, ρ_i is the mass density of the i^{th} zone, H_i is the scale height of the i^{th} zone (defined in Equation 3.7), calculated from the midplane temperature and R_i is the radius of the i^{th} zone. The midplane temperature will be the coldest region of the disk, so if the disk is generally above 17 K in the midplane, as is the case for the G0, F1 and A6 stars, the carbon, in the form of CO, will rarely freeze-out onto dust grains. This can be seen in the left panel as well; those three spectral types have a constant CO abundance similar to the initial abundance of 1×10^{-4} throughout the disk, while the K7 and M5 stars only have gas-phase CO in the inner regions of the disk where the temperature rises above 17 K. Not surprisingly, the CO(gr) abundance, shown in Figure 4.5, demonstrates a complementary trend. In the more massive stars there is a small amount of CO(gr) in the outer portions of the disk, while for the cooler stars most of the disk's midplane consists of CO(gr) with only a small region towards the inner radii where it transitions to gas-phase CO.

One problem with our results is that we see CO frozen-out in comets in our own Solar System, around a G2 type star (e.g., Ehrenfreund et al., 2004). Based on the above argument, the disk around a G2 star would seem to be too warm for CO to freeze-out into the midplane material that forms comets. However, the luminosity used to calculate the physical structure for the disk around the G0 type star is fairly large and may not be representative of most G type young stellar objects. A lower luminosity will lead to a less radiation deposited in the disk, potentially cooling the disk enough for CO to freeze-out, at least in the outer radii.

The plots in Figure 4.6 show the location of the N_2H^+ in each disk respectively. In the three hot stars the N_2H^+ abundance is consistently fairly low, while for the M5 and K7 stars there is a spike in the abundances towards the inner radii of the disk. These patterns can be explained by looking at the major pathway for simple nitrogen-bearing molecules:

$$N + OH \rightarrow NO + H \tag{4.4}$$

$$NO + N \rightarrow N_2 + O \tag{4.5}$$

$$N_2 + H_3{}^+ \rightarrow N_2H^+ + H_2 \tag{4.6}$$

$$N_2H^+ + CO \rightarrow HCO^+ + N_2 \tag{4.7}$$

From the above chemical reactions we can see that if there is abundant gas-phase CO in a region of the disk, it is likely that N_2H^+ will be destroyed. Additionally, if there is no gas phase OH, then N_2H^+ will not form. Based on these constraints the spike in abundance in Figure 4.6 is understandable. As the CO is desorbed off of dust grains, some gas-phase O is formed, which allows for the reactions above to move forward and form N_2H^+. However, once there is a significant abundance of CO in the gas phase, this N_2H^+ is quickly destroyed, leading to only a small region of high N_2H^+ abundance. This region exists closer to the central star in the M5 case due to the dependence on the CO desorption temperature. The G0, F1 and A6 stars are all too hot for CO to freeze-out onto dust grains, so any N_2H^+ that forms is quickly

destroyed through reactions with CO.

Looking now at the rest of the nitrogen-bearing chemistry, Figures 4.7, 4.8, 4.9, 4.10 and 4.11 show the abundances and density-weighted abundances for N, N_2, CN, HCN and NH_3 respectively. For N, CN, HCN and NH_3 we see plots similar to the one for N_2H^+. The hot stars have roughly constant abundances, similar to each other, while the M5 and K7 stars display a spike in the abundances at R $\sim$ 40 AU and R $\sim$ 100 AU respectively due to the narrow region in which CO is beginning to desorb, but has not yet dominated the disk chemistry. In general, the nitrogen-bearing chemistry is dependent on the gas-phase N abundance, as seen above in Equation 4.4. Eventually, the temperature in the midplane becomes high enough that N_2 also desorbs from dust grains, leading to a plot for N_2 that is similar to that for CO with constant high abundances for the hot stars and a transition region from little N_2 to high abundances of N_2 for the cooler stars.

In the hotter stars the temperature at the midplane becomes high enough at the inner radii that all of the more complex nitrogen-bearing species also desorb off of the dust grains. This is most clearly seen in Figure 4.11, the plots for NH_3, where the NH_3 abundance jumps significantly in the inner regions of the disks, where the temperature is high. We should note that there is the possibility that NH_3 formation on grain surfaces could be important, if not dominant, but that reaction is not included in our model at this time.

Figure 4.12 shows the HCO^+ abundances and density-weighted abundances for the normal models (top plots). The abundance for the hotter stars is constantly declining towards the inner radii, while the abundance for the cooler stars shows a significant increase at those inner radii. HCO^+ is formed through reactions between ions, formed mainly through cosmic ray ionization at the midplane and gas-phase CO. As a result, there is HCO^+ in the three hottest disks, but in the K7 and M5 disks HCO^+ only forms in the inner regions of the disk where it is warm enough for CO to thermally desorb.

Cosmic rays are an important ionizing source in the midplane of the disk, especially in the inner regions where the densities are high enough that both UV and

X-ray radiation is shielded. In our solar system, however, the cosmic rays responsible for this ionization are deflected away from the ecliptic by the solar wind at all radii inward of $\sim$ 85 AU, the heliopause (e.g., Burlaga et al., 2008; Decker et al., 2008). Given that cosmic rays are important for the formation of HCO^+, we were interested as to the effect a similar stellar wind would have on the midplane abundance of HCO^+. The bottom two panels of Figure 4.12 demonstrate what happens if the inner 60 AU of the disk is shielded from cosmic rays. Without any cosmic rays to provide ionizing radiation in the midplane, there is no HCO^+ formed in any of the disks inside of 60 AU. This leads to the conclusion that HCO^+ potentially could serve as a good observational tracer for the presence of cosmic rays in a disk. If HCO^+ is detected, that indicates a region that both is warm enough to have gas-phase CO and is permeable to cosmic rays or some other form of ionizing radiation.

H_2CO, seen in Figure 4.13, shows similar plots to those for CO, with a largely constant abundance for the hotter stars and an increase in abundance for the cooler stars at the inner radii. However, this transition occurs much closer in to the stars than it does for CO. This is due to the fact that, with a binding energy of $\sim$ 1700 K, the transition to gas-phase H_2CO occurs at higher temperatures than that for CO. In the hotter stars the H_2CO is mostly in the gas-phase except for the very outermost regions of the disk. For the cool stars, the very innermost regions of the disks are warm enough to desorb the H_2CO off of dust grains and so there is some gas-phase H_2CO, but only in the very innermost regions. In the inner regions of the disks around the hot stars, the combination of high temperature and strong ionizing radiation is enough to dissociate the H_2CO, which causes a decrease in the abundances there. One issue with our results for H_2CO is that there have been studies suggesting that formation on grains is a critical pathway to produce H_2CO (Öberg et al., 2009a), a reaction that is not included in our model. However, this reaction will not be important for the higher mass stars since CO is not frozen onto dust grains in those disks and, so, cannot hydrogenate to form H_2CO. Thus, the addition of H_2CO formation on grains would only affect the H_2CO abundance in the colder disks systems.

Figure 4.14 shows that most of the H_2O exists frozen onto dust grains in all five

disks. This is as expected, as the thermal desorption temperature of H_2O is about 100 K, well higher than the density-weighted midplane temperatures of any of the disks. Only in the very inner regions of the disk, where the midplane temperature is able to rise above 100 K, do we see any H_2O in the gas phase. We should point out that we do not include self-shielding of H_2O in our model, which was shown in Bethell & Bergin (2009) to potentially be important in determining the gas-phase abundance of H_2O in the inner regions of protoplanetary disks. In this chapter we are mostly concerned with temperature effects, as very little UV flux is going to be able to penetrate to the midplane, so we do not believe that H_2O self-shielding will change this result significantly.

4.4 Discussion and Conclusions

The DISCS survey (Öberg et al., 2010) has observed emission of N_2H^+ around DM Tau, LkCa 15, GM Aur and a tentative detection around AA Tau, all M or K type stars. No N_2H^+ emission was found around the F and A type stars that they observed (CQ Tau and MWC 480). This matches well with the model results presented in this chapter. The hotter stars do not allow for CO to be frozen onto dust grains which prevents the formation of N_2H^+ while the colder stars have regions where N_2H^+ can form due to transition zone in which CO is beginning to desorb, providing gas-phase OH molecules, but before all of the CO desorbs off of dust grains and destroys the N_2H^+. N_2H^+ therefore provides a clear diagnostic of the temperature structure of the disk, i.e. the presence of cold regions with $T \leq 17$ K. The spike in the abundance of the nitrogen-bearing species will lead to sharp gradients in abundance that could be detectable by future ALMA observations.

Looking just at the midplane abundances of chemical species for five disks around different spectral type stars we can determine that there are some major differences in the predicted composition. The differences are primarily due to the temperature structure, with the determining factor being the location of the freeze-out region for important molecules. If the density-weighted temperature of a disk was too warm for a molecule to freeze-out, then the abundance of that molecule would look similar

throughout the entire disk. If the temperature changed enough to produce a distinct transition region, then the chemistry would be heavily dependent on where that transition region occurred.

The simplest example of a transition determined by temperature is CO. If the temperature of the disk is below 17 K, then CO freezes-out onto dust grains. If it is higher than that value, CO is in the gas. In addition, when CO is in the gas-phase, it interacts with other species, such as N_2H^+, further affecting the chemistry seen. In the G0, F1 and A6 disks, the entire disk midplane was above 17 K, so the CO remains in the gas. In the K7 and M5 disks, the CO transitioned to the gas-phase at around 150 and 70 AU respectively.

Temperature dependent effects will play a strong role on the observed chemistry and will serve to allow us to use this molecular chemistry as tracers of the physical properties. One clear example of this is HCO^+. If HCO^+ is present, that indicates both that there is gas-phase CO and that ionizing radiation can penetrate to that region of the disk. The presence of HCO^+ therefore tells us something about the temperature structure of the disk, since the temperature has to be above 17 K, and about the presence or absence of cosmic rays, the most likely ionizing source.

The inclusion of dust settling in our models would primarily affect the midplane temperatures. As discussed in Section 2.2.1, the inclusion of dust settling would actually lower the midplane dust temperatures, as opposed to the rest of the disk where the temperatures would be increased. This change in temperature as the dust settles from $\epsilon = 1$ to $\epsilon = 0.001$ would range from $\sim$ 5 K at 150 AU to $\sim$ 30 K at 2 AU. This could potentially lead to some changes in chemical abundances in the inner regions of the disk, and even smaller changes in the outer regions. As a result, this would not strongly affect the density-weighted abundances displayed earlier. The largest changes would be the location of specific transitions, especially ones such as CO to CO(gr), that are primarily temperature dependent. The UV radiation would also penetrate deeper into the disk when dust settling was included. However, it would not reach the midplane until the disk becomes optically thin, which is not the phase modeled in our work.

In general, current and even future observations of protoplanetary disks primarily trace the surface layers of the disk, as we need to detect optically thin isotopologues in order to observe deeper into the disk. As we enter the ALMA age, however, surveys in a variety of systems will become common and some of the simple predictions presented here will be tested.

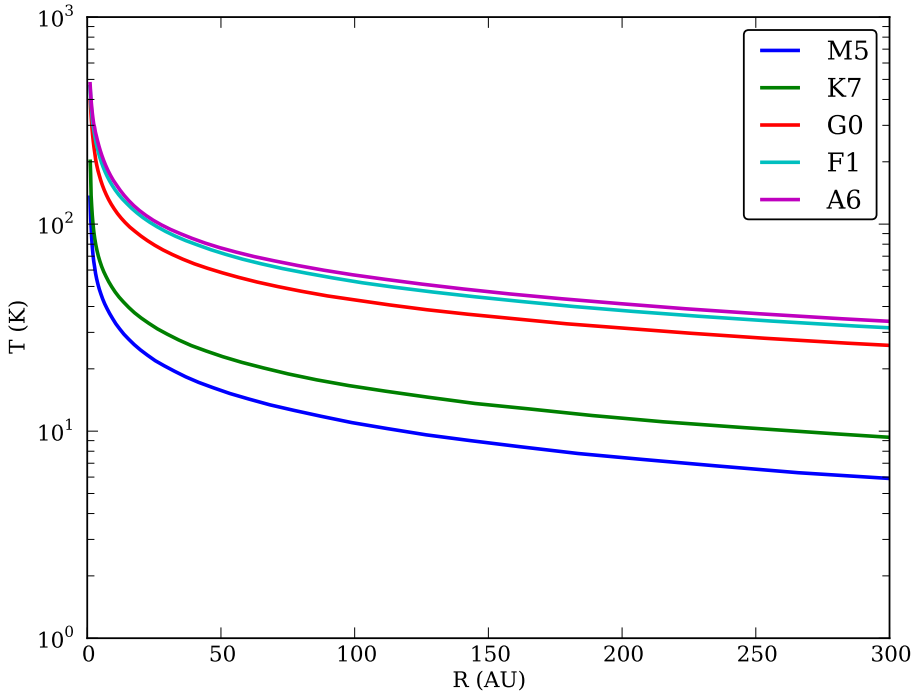

Figure 4.1. Plot of midplane temperature vs. radius for five disk models irradiated by central stars with different spectral types.

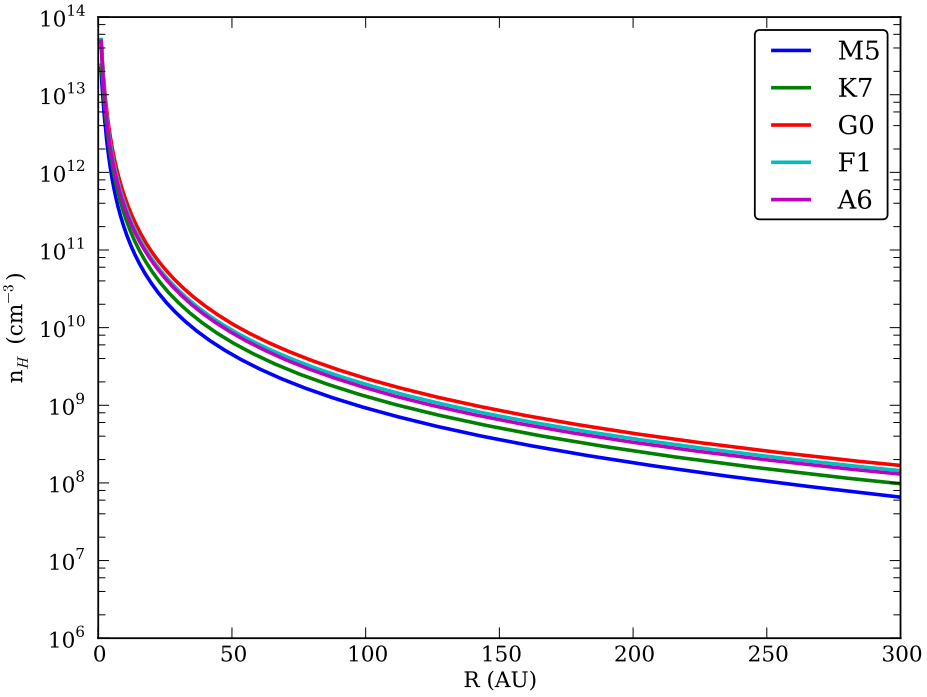

Figure 4.2. Plot of midplane density vs. radius for five disk models irradiated by central stars with different spectral types.

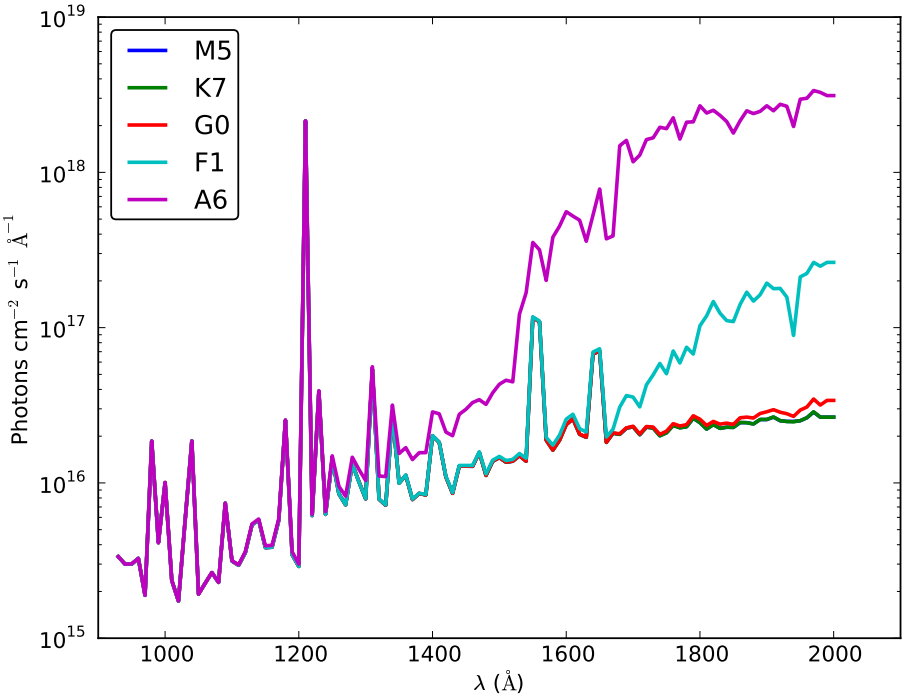

Figure 4.3. Plot of UV fields at the stellar surface for five spectral types used.

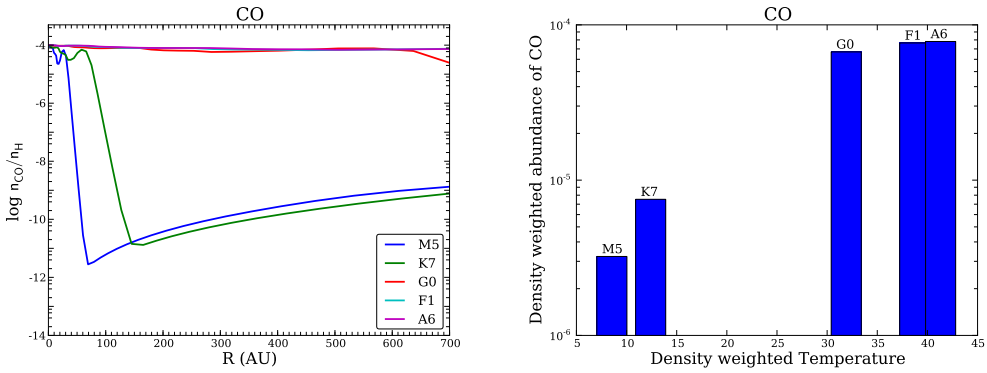

Figure 4.4. Plot of midplane CO abundance relative to total hydrogen vs. radius (left). Plot of density-weighted midplane abundance vs. density-weighted midplane temperature (right).

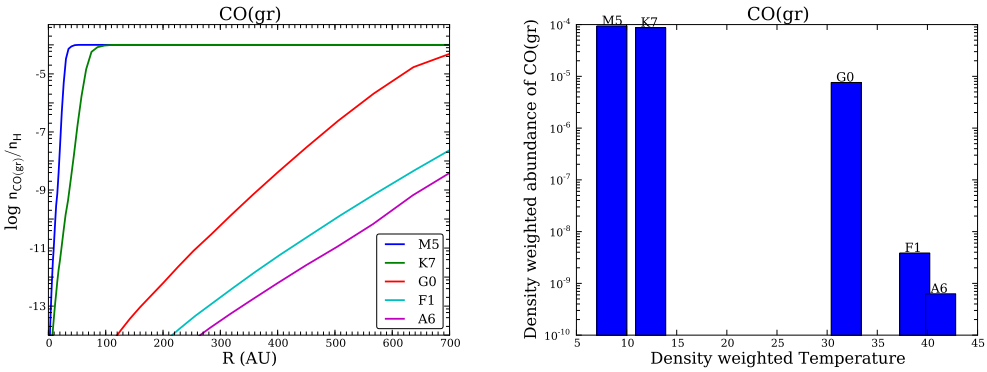

Figure 4.5. Plot of midplane CO(gr) abundance relative to total hydrogen vs. radius (left). Plot of density-weighted midplane abundance vs. density-weighted midplane temperature (right).

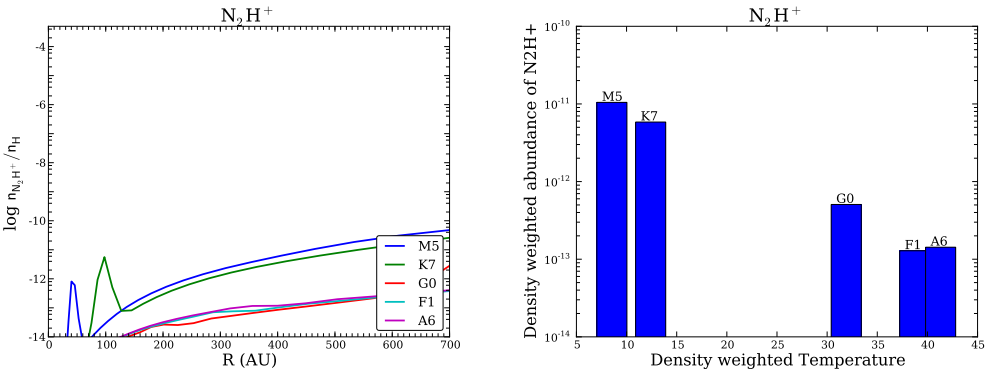

Figure 4.6. Plot of midplane N_2H^+ abundance relative to total hydrogen vs. radius (left). Plot of density-weighted midplane abundance vs. density-weighted midplane temperature (right).

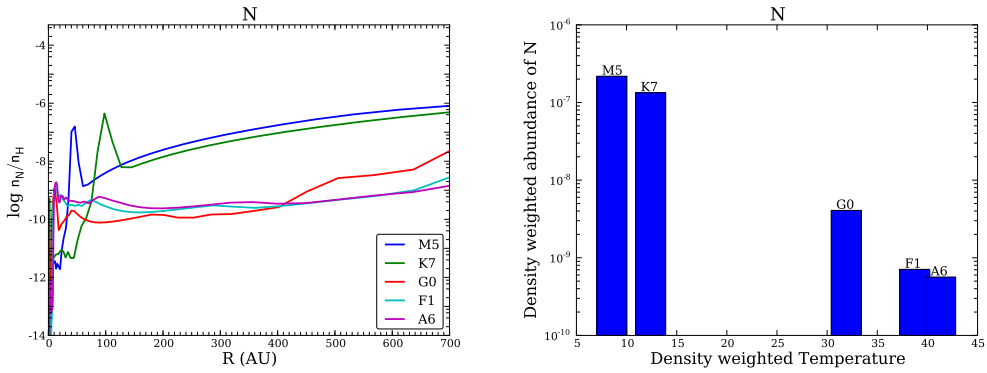

Figure 4.7. Plot of midplane N abundance relative to total hydrogen vs. radius (left). Plot of density-weighted midplane abundance vs. density-weighted midplane temperature (right).

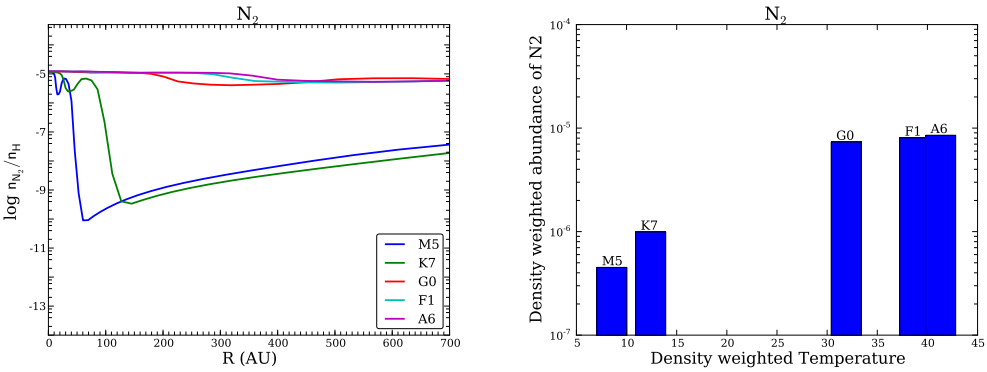

Figure 4.8. Plot of midplane N_2 abundance relative to total hydrogen vs. radius (left). Plot of density-weighted midplane abundance vs. density-weighted midplane temperature (right).

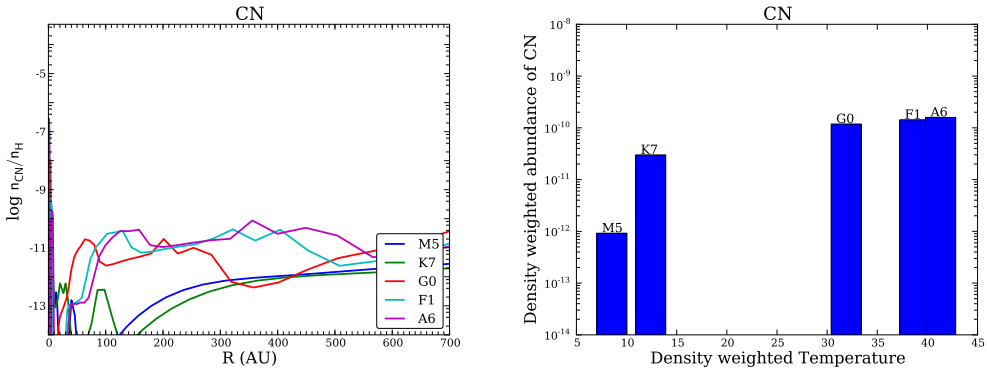

Figure 4.9. Plot of midplane CN abundance relative to total hydrogen vs. radius (left). Plot of density-weighted midplane abundance vs. density-weighted midplane temperature (right).

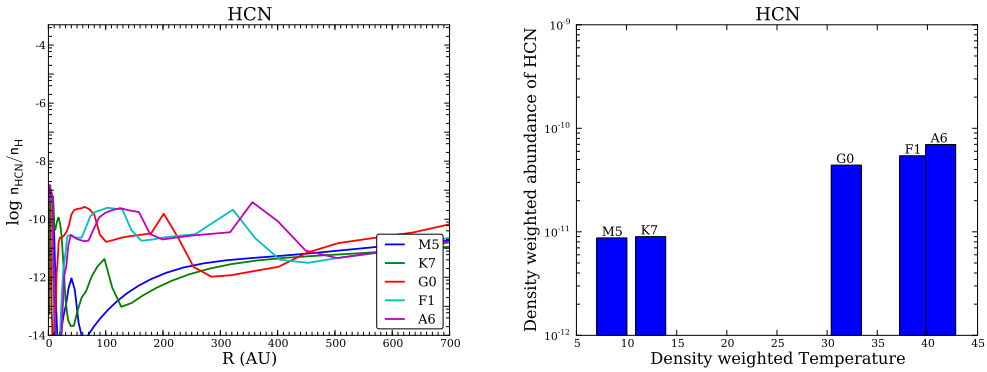

Figure 4.10. Plot of midplane HCN abundance relative to total hydrogen vs. radius (left). Plot of density-weighted midplane abundance vs. density-weighted midplane temperature (right).

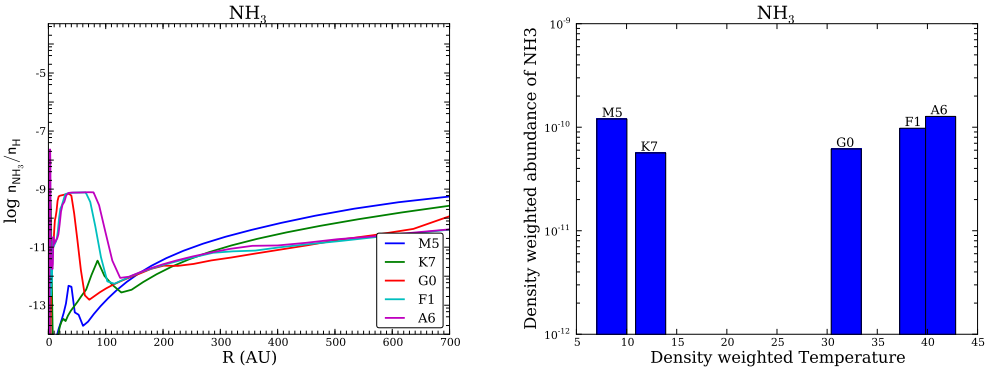

Figure 4.11. Plot of midplane NH_3 abundance relative to total hydrogen vs. radius (left). Plot of density-weighted midplane abundance vs. density-weighted midplane temperature (right).

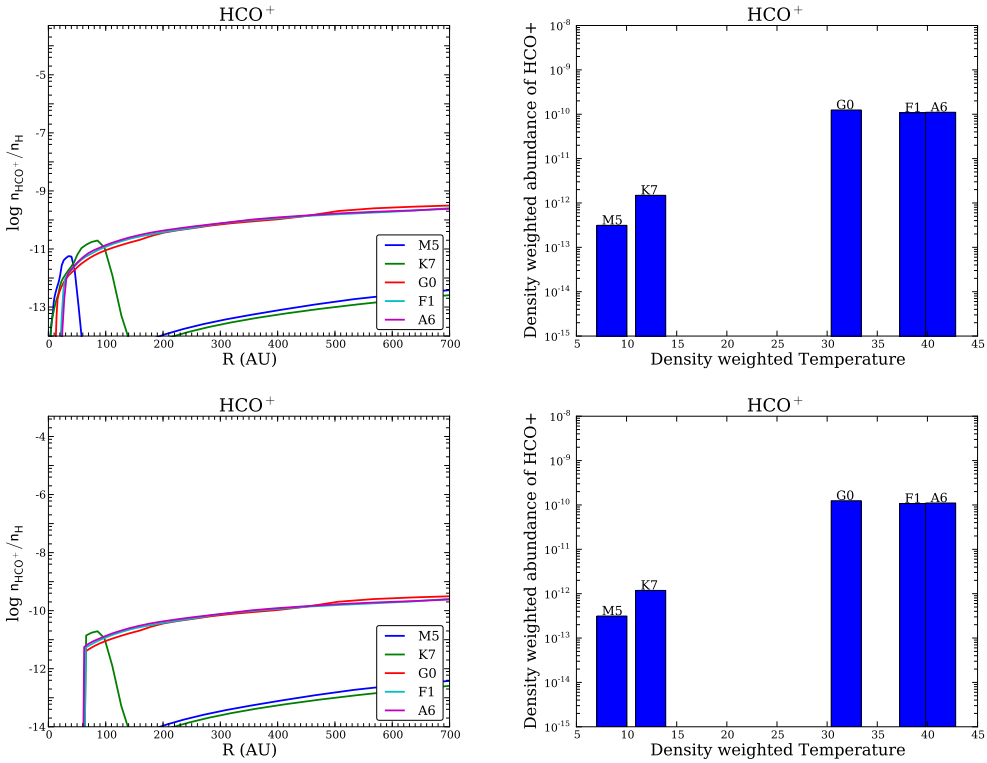

Figure 4.12. Plot of midplane HCO^+ abundance relative to total hydrogen vs. radius (top left). Plot of density-weighted midplane abundance vs. density-weighted midplane temperature (top right). Bottom plots are the same, but with cosmic rays shielded for the inner 60 AU of the disk to mimic a heliopause.

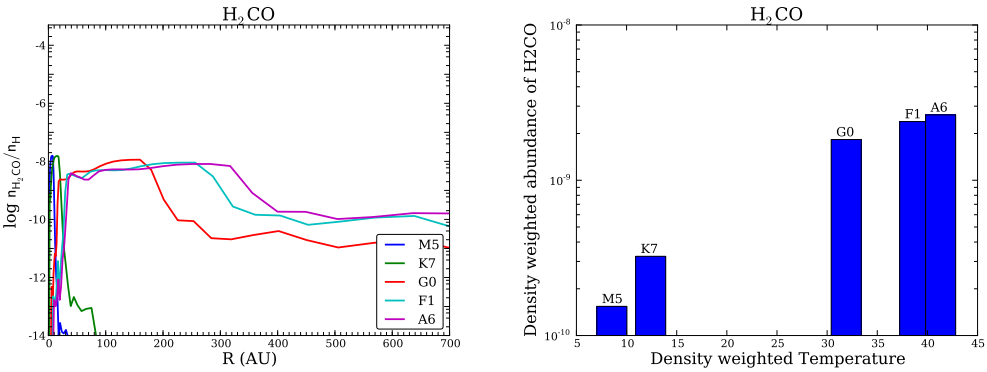

Figure 4.13. Plot of midplane H_2CO abundance relative to total hydrogen vs. radius (top left). Plot of density-weighted midplane abundance vs. density-weighted midplane temperature (top right).

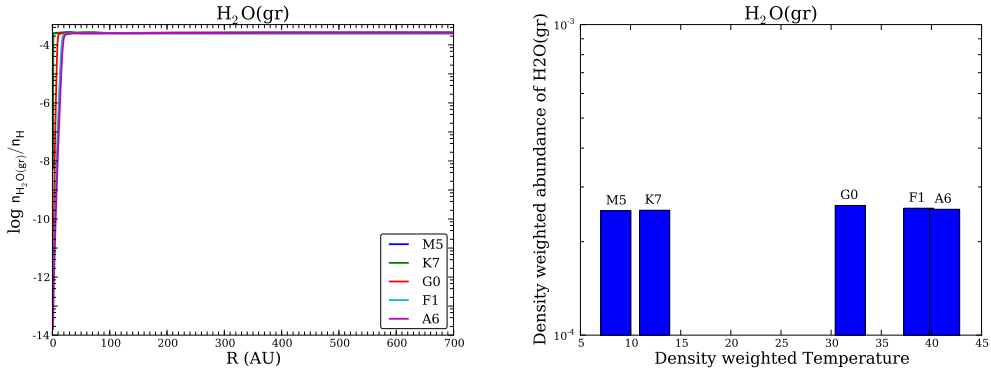

Figure 4.14. Plot of midplane H_2O(gr) abundance relative to total hydrogen vs. radius (top left). Plot of density-weighted midplane abundance vs. density-weighted midplane temperature (top right).

Table 4.1. Star & Disk Physical Parameters

Parameter	M5	K7	G0	F1	A6
$R_{disk,max}$ (AU)	300	700	700	700	700
M_{disk} ($M_\odot$)	0.0147	0.0343	0.0403	0.0358	0.0337
R_{star} ($R_\odot$)	1.40	2.00	7.13	7.78	6.69
M_{star} ($M_\odot$)	0.2	0.5	3.5	4.0	4.0
T_{star} (K)	3240	4000	6000	7000	8000
L_{star} ($L_\odot$)	0.19	0.91	58	130	160

CHAPTER 5

Conclusions

5.1 Summary of Results

In this dissertation, we presented a new model of protoplanetary disk chemical evolution and analyzed the effects that disk physical structure has on chemical composition. Our model incorporated UV radiative transport, including Ly α radiation, dust settling, dust-dependent X-ray opacity and the effects of central star spectral type along with a full chemical network.

In Chapter 2, we presented a detailed description of our basic model and demonstrated the effects that including Ly α radiation and dust settling had on protoplanetary disk chemistry. The inclusion of Ly α radiation gave us slightly better fits to the observed data, though with the small number of species observed and only two of them being affected by Ly α radiation those results are somewhat preliminary. In general, Ly α radiation affected those species having photodissociation cross sections at 1216 Å. This included HC_3N, HCN, NH_3, SO_2, C_2H_4 and CH_4, which were depleted by an order of magnitude or more when Ly α radiation was added to the model.

We also discussed the effects of incorporating dust settling on the disk chemical composition. As expected, dust settling increased the UV penetration, which in turn affected the size and location of the molecular and freeze-out regions. As the disk became more settled, UV radiation penetrated deeper into the disk, shrinking the freeze-out zone. In addition, the molecular layer increased in size, which enhanced the abundance of species such as gas-phase CO. This in turn depleted some species like N_2H^+, which are destroyed in the presence of CO. We also found that, in general, the models which included dust settling produced better fits to the observations.

In Chapter 3, we discussed whether the inclusion of dust settling dependent X-ray opacities impacted the active region of the disk. While dust-dependent X-ray opacities did not have a large effect on the chemistry of the disk, rarely more than a factor of two in column density, we showed once again that dust evolution is an important component of a protoplanetary disk chemical model. Without dust settling included, the active regions of the disk were not large enough to produce the observed mass accretion rates. When dust settling was included, however, we easily were able to achieve the 10 g cm^{-2} required at 10 AU to produce accretion rates of 10^{-8} $M_{\odot}$ yr^{-1}. For our model, due to the relatively low disk mass, cosmic rays had an unexpectedly strong impact on the location and size of the active zone. Without cosmic rays included, the mass of the active region was too small to match observed mass accretion rates.

Finally, in Chapter 4 we looked at the effect of central star spectral type on the chemistry of the disk midplane. Because we only modeled the midplane, the spectral type dependent chemical changes were largely due to changes in the temperature. The higher mass stars, types G0, F1 and A6, had warm disks in which species such as CO did not freeze-out onto dust grains. In disks around the M5 and K7 stars, by comparison, the midplane was cooler and there was a clear transition region from CO(gr) to CO. There also were regions in which N desorbed off of dust grains, thereby providing enough free nitrogen to produce some of the more complex nitrogen-bearing species. From our analysis there were two distinct observational consequences of central star spectral type. The first was that for the higher mass stars, the disks were too warm for CO to freeze-out and, as a result, N_2H^+ was unable to form. This means that the presence of N_2H^+ is an indication of a region cold enough for CO to freeze-out onto dust grains, but warm enough for N to desorb. The second was that HCO^+ was able to form only in the regions of the disk where CO existed in the gas phase and where there was some form of ionizing radiation to produce $H_3{}^+$. While we looked only at midplane abundances, which are unobservable with current instruments and will be able to be detected only through optically thin chemical isotopologues with ALMA, these effects will occur in vertical regions of the disks as

well and, so, can act as important tracers of the physical environment in the disk.

5.2 Future Work

Large scale protoplanetary disk chemical surveys are just starting to occur (e.g., Öberg et al., 2010). With instruments such as ALMA and JWST on the horizon, the amount of data we soon will be able to collect on these objects will open up a new frontier in our understanding of disk chemical evolution. The upcoming improvements in resolution and sensitivity will allow the detection of numerous molecules that are unobservable today and chemical surveys will become commonplace. In order to understand and analyze the upcoming data, good theoretical models of the protoplanetary disk chemistry are needed, especially ones that connect the physical and chemical structure.

In order to use our chemical model to match these upcoming observations, a number of aspects of the model presented in this dissertation likely need to be enhanced. One of the most important would be to combine the physical structure and chemical models so that the gas and dust temperatures could be calculated independently. In the densest regions of the disk, coupling these temperatures together appears to be a valid assumption (Kamp & Dullemond, 2004), however in the upper layers of the disk where $A_V < 0.1$, this approximation breaks down. De-coupling the physical and chemical structure will lead to puffier disks, with the stellar energy being deposited in higher layers above the midplane. This in turn will affect where the important chemistry will occur (Woitke et al., 2009).

An additional major modification to the code would be to convert it from the current 1+1D structure to a full 2D framework. This would have the advantage that horizontal processes, such as turbulence, could be included along with the chemical calculations. While it is not certain that these processes play a large role in the observed chemistry of protoplanetary disks (e.g., Willacy et al., 2006), these effects may become more important as our observational resolution improves.

Another way to expand the model would be to extend the chemical network that is used. This could include the addition of more on-grain chemical reactions, such

as the hydrogenation of N, C and CO on grain surfaces to form NH_3, CH_4 and H_2CO respectively. Some species, such as CH_3OH and the ones just mentioned, are thought to have significant formation pathways that occur on the surfaces of dust grains (Öberg et al., 2009a). Leaving out these reactions potentially could lead to underestimating their abundances, especially in the coldest regions in which gas phase reactions occur more slowly. In addition, the inclusion of isotopic chemistry will be important, as many deuterated species have been observed, such as H_2D^+, DCO^+ and DCN (e.g., Ceccarelli et al., 2004; van Dishoeck et al., 2003; Qi et al., 2008). These species can serve as probes of the physical structure of the disk, but in order to understand the observations fully it is important to include deuteration reactions in our chemical network.

Finally, it would be useful to repeat the study done in chapter 4 on the effect that spectral type has on disk chemistry, including dust settling and analyzing the entire disk composition instead of just the midplane. While this would be a complicated study, understanding exactly how all of these processes impact the chemistry and which ones produce observable signatures would allow us to further interpret current and future observations. Ultimately, the ideal situation would be to produce a source-specific model for each observed protoplanetary disk. This model would match the observed physical structure of each object, instead of trying to match them with a generic model, and may lead to better agreement on the chemical composition.

With ALMA on the horizon, large scale surveys of protoplanetary disks will soon be possible, with many more objects and molecular species observable than is possible with current instruments. In order to understand the observations we need detailed chemical models that explore the connection between the physical structure evolution and the chemical composition. With such models, we will be able to learn more about the material that composes planets, which will help us to determine how planets, and ultimately life, formed in protoplanetary disks.

BIBLIOGRAPHY

Aikawa, Y. & Herbst, E. 1999, A&A, 351, 233

—. 2001, A&A, 371, 1107

Aikawa, Y., Miyama, S. M., Nakano, T., & Umebayashi, T. 1996, ApJ, 467, 684

Aikawa, Y., Momose, M., Thi, W., van Zadelhoff, G., Qi, C., Blake, G. A., & van Dishoeck, E. F. 2003, PASJ, 55, 11

Aikawa, Y. & Nomura, H. 2006, ApJ, 642, 1152

—. 2008, Physica Scripta Volume T, 130, 014011

Aikawa, Y., Umebayashi, T., Nakano, T., & Miyama, S. M. 1997, ApJ, 486, L51+

—. 1999, ApJ, 519, 705

Aikawa, Y., van Zadelhoff, G. J., van Dishoeck, E. F., & Herbst, E. 2002, A&A, 386, 622

Alexander, R. D., Clarke, C. J., & Pringle, J. E. 2005, MNRAS, 358, 283

Andrews, S. M. & Williams, J. P. 2005, ApJ, 631, 1134

Andrews, S. M., Wilner, D. J., Hughes, A. M., Qi, C., & Dullemond, C. P. 2009, ApJ, 700, 1502

Apai, D. & Lauretta, D. S., eds. 2010, Protoplanetary Dust, Cambridge Planetary Science No. 12 (Cambridge University Press)

Ardila, D. R., Basri, G., Walter, F. M., Valenti, J. A., & Johns-Krull, C. M. 2002, ApJ, 566, 1100

Bai, X. & Stone, J. M. 2011, ArXiv e-prints

Balbus, S. A. 2003, ARA&A, 41, 555

Balbus, S. A. & Hawley, J. F. 1991, ApJ, 376, 214

Beckwith, S. V. W. & Sargent, A. I. 1993, ApJ, 402, 280

Beckwith, S. V. W., Sargent, A. I., Chini, R. S., & Guesten, R. 1990, AJ, 99, 924

Bergin, E., Calvet, N., D'Alessio, P., & Herczeg, G. J. 2003, ApJ, 591, L159

Bergin, E., Calvet, N., Sitko, M. L., Abgrall, H., D'Alessio, P., Herczeg, G. J., Roueff, E., Qi, C., Lynch, D. K., Russell, R. W., Brafford, S. M., & Perry, R. B. 2004, ApJ, 614, L133

Bergin, E. A. 2011, The Chemical Evolution of Protoplanetary Disks, ed. P. J. V. Garcia (Physical Processes in Circumstellar Disks around Young Stars - University of Chicago Press, Theoretical Astrophysics Series), in press, arXiv:0908.3708

Bergin, E. A., Aikawa, Y., Blake, G. A., & van Dishoeck, E. F. 2007, Protostars and Planets V, 751

Bethell, T. & Bergin, E. 2009, Science, 326, 1675

Bethell, T. & Bergin, E. A. 2011, in prep.

Bethell, T., Bergin, E. A., & Calvet, N. 2010, in prep.

Bethell, T. J., Zweibel, E. G., & Li, P. S. 2007, ApJ, 667, 275

Bisschop, S. E., Fraser, H. J., Öberg, K. I., van Dishoeck, E. F., & Schlemmer, S. 2006, A&A, 449, 1297

Bitner, M. A., Richter, M. J., Lacy, J. H., Greathouse, T. K., Jaffe, D. T., & Blake, G. A. 2007, ApJ, 661, L69

Black, J. H. & van Dishoeck, E. F. 1987, ApJ, 322, 412

Bonilha, J. R. M., Ferch, R., Salpeter, E. E., Slater, G., & Noerdlinger, P. D. 1979, ApJ, 233, 649

Bringa, E. M. & Johnson, R. E. 2004, ApJ, 603, 159

Burke, J. R. & Hollenbach, D. J. 1983, ApJ, 265, 223

Burlaga, L. F., Ness, N. F., Acuña, M. H., Lepping, R. P., Connerney, J. E. P., & Richardson, J. D. 2008, Nature, 454, 75

Calvet, N., D'Alessio, P., Hartmann, L., Wilner, D., Walsh, A., & Sitko, M. 2002, ApJ, 568, 1008

Calvet, N., D'Alessio, P., Watson, D. M., Franco-Hernández, R., Furlan, E., Green, J., Sutter, P. M., Forrest, W. J., Hartmann, L., Uchida, K. I., Keller, L. D., Sargent, B., Najita, J., Herter, T. L., Barry, D. J., & Hall, P. 2005, ApJ, 630, L185

Calvet, N. & Gullbring, E. 1998, ApJ, 509, 802

Calvet, N., Magris, G. C., Patino, A., & D'Alessio, P. 1992, Rev. Mexicana Astron. Astrofis., 24, 27

Calvet, N., Patino, A., Magris, G. C., & D'Alessio, P. 1991, ApJ, 380, 617

Cazaux, S. & Tielens, A. G. G. M. 2004, ApJ, 604, 222

Ceccarelli, C., Dominik, C., Caux, E., Lefloch, B., & Caselli, P. 2005, ApJ, 631, L81

Ceccarelli, C., Dominik, C., Lefloch, B., Caselli, P., & Caux, E. 2004, ApJ, 607, L51

Chiang, E. I. & Goldreich, P. 1997, ApJ, 490, 368

D'Alessio, P., Calvet, N., Hartmann, L., Franco-Hernández, R., & Servín, H. 2006, ApJ, 638, 314

D'Alessio, P., Calvet, N., Hartmann, L., Lizano, S., & Cantó, J. 1999, ApJ, 527, 893

D'Alessio, P., Canto, J., Calvet, N., & Lizano, S. 1998, ApJ, 500, 411

Decker, R. B., Krimigis, S. M., Roelof, E. C., Hill, M. E., Armstrong, T. P., Gloeckler, G., Hamilton, D. C., & Lanzerotti, L. J. 2008, Nature, 454, 67

Dominik, C., Ceccarelli, C., Hollenbach, D., & Kaufman, M. 2005, ApJ, 635, L85

Draine, B. T. 2003, ARA&A, 41, 241

Draine, B. T. & Bertoldi, F. 1996, ApJ, 468, 269

Draine, B. T., Roberge, W. G., & Dalgarno, A. 1983, ApJ, 264, 485

Dullemond, C. P. & Dominik, C. 2004, A&A, 421, 1075

Dullemond, C. P. & Natta, A. 2003, A&A, 408, 161

Dullemond, C. P., van Zadelhoff, G. J., & Natta, A. 2002, A&A, 389, 464

Dutrey, A., Guilloteau, S., & Guelin, M. 1997, A&A, 317, L55

Dutrey, A., Guilloteau, S., & Ho, P. 2007a, Protostars and Planets V, 495

Dutrey, A., Henning, T., Guilloteau, S., Semenov, D., Piétu, V., Schreyer, K., Bacmann, A., Launhardt, R., Pety, J., & Gueth, F. 2007b, A&A, 464, 615

Ehrenfreund, P., Charnley, S. B., & Wooden, D. 2004, From interstellar material to comet particles and molecules, ed. Festou, M. C., Keller, H. U., & Weaver, H. A., 115–133

Espaillat, C., Calvet, N., D'Alessio, P., Hernández, J., Qi, C., Hartmann, L., Furlan, E., & Watson, D. M. 2007, ApJ, 670, L135

Fegley, Jr., B. & Prinn, R. G. 1989, in The Formation and Evolution of Planetary Systems, ed. H. A. Weaver & L. Danly, 171–205

Feigelson, E. D. & Montmerle, T. 1999, ARA&A, 37, 363

Flaccomio, E., Stelzer, B., Sciortino, S., Micela, G., Pillitteri, I., & Testi, L. 2009, A&A, 505, 695

Fleming, T. & Stone, J. M. 2003, ApJ, 585, 908

Fleming, T. P., Stone, J. M., & Hawley, J. F. 2000, ApJ, 530, 464

Fogel, J. K. J., Bethell, T. J., Bergin, E. A., Calvet, N., & Semenov, D. 2011, ApJ, 726, 29

Furlan, E., Hartmann, L., Calvet, N., D'Alessio, P., Franco-Hernández, R., Forrest, W. J., Watson, D. M., Uchida, K. I., Sargent, B., Green, J. D., Keller, L. D., & Herter, T. L. 2006, ApJS, 165, 568

Furlan, E., McClure, M., Calvet, N., Hartmann, L., D'Alessio, P., Forrest, W. J., Watson, D. M., Uchida, K. I., Sargent, B., Green, J. D., & Herter, T. L. 2008, ApJS, 176, 184

Gammie, C. F. 1996, ApJ, 457, 355

Glassgold, A. E., Feigelson, E. D., & Montmerle, T. 2000, Protostars and Planets IV, 429

Glassgold, A. E., Najita, J., & Igea, J. 1997, ApJ, 480, 344

Graedel, T. E., Langer, W. D., & Frerking, M. A. 1982, ApJS, 48, 321

Habing, H. J. 1968, Bull. Astron. Inst. Netherlands, 19, 421

Hartmann, L. 2008, Physica Scripta Volume T, 130, 014012

Hartmann, L., Calvet, N., Gullbring, E., & D'Alessio, P. 1998, ApJ, 495, 385

Hasegawa, T. I. & Herbst, E. 1993, MNRAS, 261, 83

Hawley, J. F. & Stone, J. M. 1998, ApJ, 501, 758

Hayashi, C. 1981, Progress of Theoretical Physics Supplement, 70, 35

Herczeg, G. J., Linsky, J. L., Valenti, J. A., Johns-Krull, C. M., & Wood, B. E. 2002, ApJ, 572, 310

Herczeg, G. J., Wood, B. E., Linsky, J. L., Valenti, J. A., & Johns-Krull, C. M. 2004, ApJ, 607, 369

Hollenbach, D., Kaufman, M. J., Bergin, E. A., & Melnick, G. J. 2009, ApJ, 690, 1497

Hollenbach, D. J., Yorke, H. W., & Johnstone, D. 2000, Protostars and Planets IV, 401

Hummer, D. G. 1962, MNRAS, 125, 21

Igea, J. & Glassgold, A. E. 1999, ApJ, 518, 848

Ilgner, M., Henning, T., Markwick, A. J., & Millar, T. J. 2004, A&A, 415, 643

Ilgner, M. & Nelson, R. P. 2006, A&A, 445, 205

Jonkheid, B., Dullemond, C. P., Hogerheijde, M. R., & van Dishoeck, E. F. 2007, A&A, 463, 203

Jonkheid, B. J. 2006, PhD thesis, Leiden Observatory, Leiden University, P.O. Box 9513, 2300 RA Leiden, The Netherlands

Kamp, I. & Dullemond, C. P. 2004, ApJ, 615, 991

Kastner, J. H., Zuckerman, B., Hily-Blant, P., & Forveille, T. 2008, A&A, 492, 469

Kastner, J. H., Zuckerman, B., Weintraub, D. A., & Forveille, T. 1997, Science, 277, 67

Kenyon, S. J. & Hartmann, L. 1987, ApJ, 323, 714

—. 1995, ApJS, 101, 117

Kitamura, Y., Momose, M., Yokogawa, S., Kawabe, R., Tamura, M., & Ida, S. 2002, ApJ, 581, 357

Koerner, D. W. & Sargent, A. I. 1995, AJ, 109, 2138

Kokubo, E. & Ida, S. 2000, Icarus, 143, 15

Lee, H., Herbst, E., Pineau des Forets, G., Roueff, E., & Le Bourlot, J. 1996, A&A, 311, 690

Leger, A., Jura, M., & Omont, A. 1985, A&A, 144, 147

Lewis, J. S. 1974, Science, 186, 440

Maret, S. & Bergin, E. A. 2007, ApJ, 664, 956

Masuda, K., Takahashi, J., & Mukai, T. 1998, A&A, 330, 773

Matsumura, S. & Pudritz, R. E. 2003, ApJ, 598, 645

Matsumura, S., Pudritz, R. E., & Thommes, E. W. 2009, ApJ, 691, 1764

McCall, B. J., Huneycutt, A. J., Saykally, R. J., Djuric, N., Dunn, G. H., Semaniak, J., Novotny, O., Al-Khalili, A., Ehlerding, A., Hellberg, F., Kalhori, S., Neau, A., Thomas, R., Paal, A., Österdahl, F., & Larsson, M. 2005, Journal of Physics Conference Series, 4, 92

McCall, B. J., Huneycutt, A. J., Saykally, R. J., Djuric, N., Dunn, G. H., Semaniak, J., Novotny, O., Al-Khalili, A., Ehlerding, A., Hellberg, F., Kalhori, S., Neau, A., Thomas, R. D., Paal, A., Österdahl, F., & Larsson, M. 2004, Phys. Rev. A, 70, 052716

Miyauchi, N., Hidaka, H., Chigai, T., Nagaoka, A., Watanabe, N., & Kouchi, A. 2008, Chemical Physics Letters, 456, 27

Najita, J. R., Strom, S. E., & Muzerolle, J. 2007, MNRAS, 378, 369

Nomura, H., Aikawa, Y., Nakagawa, Y., & Millar, T. J. 2009, A&A, 495, 183

Nomura, H., Aikawa, Y., Tsujimoto, M., Nakagawa, Y., & Millar, T. J. 2007, ApJ, 661, 334

Nomura, H. & Millar, T. J. 2005, A&A, 438, 923

Öberg, K. I., Fuchs, G. W., Awad, Z., Fraser, H. J., Schlemmer, S., van Dishoeck, E. F., & Linnartz, H. 2007, ApJ, 662, L23

Öberg, K. I., Garrod, R. T., van Dishoeck, E. F., & Linnartz, H. 2009a, A&A, 504, 891

Öberg, K. I., Linnartz, H., Visser, R., & van Dishoeck, E. F. 2009b, ApJ, 693, 1209

Öberg, K. I., Qi, C., Fogel, J. K. J., Bergin, E. A., Andrews, S. M., Espaillat, C., van Kempen, T. A., Wilner, D. J., & Pascucci, I. 2010, ApJ, 720, 480

Pascucci, I., Apai, D., Luhman, K., Henning, T., Bouwman, J., Meyer, M. R., Lahuis, F., & Natta, A. 2009, ApJ, 696, 143

Perez-Becker, D. & Chiang, E. 2011, ApJ, 727, 2

Pinte, C., Woitke, P., Ménard, F., Duchêne, G., Kamp, I., Meeus, G., Mathews, G., Howard, C. D., Grady, C. A., Thi, W., Tilling, I., Augereau, J., Dent, W. R. F., Alacid, J. M., Andrews, S., Ardila, D. R., Aresu, G., Barrado, D., Brittain, S., Ciardi, D. R., Danchi, W., Eiroa, C., Fedele, D., de Gregorio-Monsalvo, I., Heras, A., Huelamo, N., Krivov, A., Lebreton, J., Liseau, R., Martin-Zaïdi, C., Mendigutía, I., Montesinos, B., Mora, A., Morales-Calderon, M., Nomura, H., Pantin, E., Pascucci, I., Phillips, N., Podio, L., Poelman, D. R., Ramsay, S., Riaz, B., Rice, K., Riviere-Marichalar, P., Roberge, A., Sandell, G., Solano, E., Vandenbussche, B., Walker, H., Williams, J. P., White, G. J., & Wright, G. 2010, A&A, 518, L126+

Pontoppidan, K. M., Salyk, C., Blake, G. A., Meijerink, R., Carr, J. S., & Najita, J. 2010, ApJ, 720, 887

Prinn, R. G. 1993, in Protostars and Planets III, ed. E. H. Levy & J. I. Lunine, 1005–1028

Qi, C. 2001, PhD thesis, California Institute of Technology

Qi, C., Kessler, J. E., Koerner, D. W., Sargent, A. I., & Blake, G. A. 2003, ApJ, 597, 986

Qi, C., Wilner, D. J., Aikawa, Y., Blake, G. A., & Hogerheijde, M. R. 2008, ApJ, 681, 1396

Sano, T., Miyama, S. M., Umebayashi, T., & Nakano, T. 2000, ApJ, 543, 486

Schreyer, K., Guilloteau, S., Semenov, D., Bacmann, A., Chapillon, E., Dutrey, A., Gueth, F., Henning, T., Hersant, F., Launhardt, R., Pety, J., & Piétu, V. 2008, A&A, 491, 821

Semenov, D., Hersant, F., Wakelam, V., Dutrey, A., Chapillon, E., Guilloteau, S., Henning, T., Launhardt, R., Pietu, V., & Schreyer, K. 2010, A&A

Semenov, D., Wiebe, D., & Henning, T. 2004, A&A, 417, 93

—. 2006, ApJ, 647, L57

Shakura, N. I. & Sunyaev, R. A. 1973, A&A, 24, 337

Sicilia-Aguilar, A., Hartmann, L. W., Briceño, C., Muzerolle, J., & Calvet, N. 2004, AJ, 128, 805

Simon, M., Dutrey, A., & Guilloteau, S. 2000, ApJ, 545, 1034

Smith, I. W. M., Herbst, E., & Chang, Q. 2004, MNRAS, 350, 323

Spaans, M. & Neufeld, D. A. 1997, ApJ, 484, 785

Thi, W., van Zadelhoff, G., & van Dishoeck, E. F. 2004, A&A, 425, 955

Thommes, E. W., Duncan, M. J., & Levison, H. F. 2003, Icarus, 161, 431

Tielens, A. G. G. M. 2005, The Physics and Chemistry of the Interstellar Medium, ed. Tielens, A. G. G. M.

Turner, N. J., Carballido, A., & Sano, T. 2010, ApJ, 708, 188

Umebayashi, T. 1983, Progress of Theoretical Physics, 69, 480

Umebayashi, T. & Nakano, T. 1981, PASJ, 33, 617

van Dishoeck, E. F. & Black, J. H. 1988, ApJ, 334, 771

van Dishoeck, E. F., Jonkheid, B., & van Hemert, M. C. 2006, Faraday Discussions - Chemical Society, 133, 231

van Dishoeck, E. F., Thi, W., & van Zadelhoff, G. 2003, A&A, 400, L1

van Zadelhoff, G., Aikawa, Y., Hogerheijde, M. R., & van Dishoeck, E. F. 2003, A&A, 397, 789

Vasyunin, A. I., Semenov, D., Henning, T., Wakelam, V., Herbst, E., & Sobolev, A. M. 2008, ApJ, 672, 629

Vasyunin, A. I., Wiebe, D. S., Birnstiel, T., Zhukovska, S., Henning, T., & Dullemond, C. P. 2011, ApJ, 727, 76

Visser, R., van Dishoeck, E. F., & Black, J. H. 2009, A&A, 503, 323

Wakelam, V., Herbst, E., & Selsis, F. 2006, A&A, 451, 551

Wetherill, G. W. & Stewart, G. R. 1993, Icarus, 106, 190

Willacy, K. 2007, ApJ, 660, 441

Willacy, K., Klahr, H. H., Millar, T. J., & Henning, T. 1998, A&A, 338, 995

Willacy, K., Langer, W., Allen, M., & Bryden, G. 2006, ApJ, 644, 1202

Willacy, K. & Langer, W. D. 2000, ApJ, 544, 903

Willacy, K. & Woods, P. M. 2009, ApJ, 703, 479

Woitke, P., Kamp, I., & Thi, W. 2009, A&A, 501, 383

Woodall, J., Agúndez, M., Markwick-Kemper, A. J., & Millar, T. J. 2007, A&A, 466, 1197